

**DEEP DRAWING AND REDRAWING OF
304 STAINLESS STEEL SHEET**

**EXPERIMENTAL AND NUMERICAL STUDIES OF
DEEP DRAWING AND REDRAWING OF
304 STAINLESS STEEL SHEET**

By

SHIXIONG HAN, B.Eng.

A Thesis

Submitted to the School of Graduate Studies

in Partial Fulfillment of the Requirements

for the Degree

Master of Applied Science

McMaster University

© Copyright by Shixiong Han, November 2006

MASTER OF APPLIED SCIENCE (2006)
(Mechanical Engineering)

McMaster University
Hamilton, Ontario

TITLE: Experimental and Numerical Studies of Deep
Drawing and Redrawing of 304 Stainless Steel Sheet

AUTHOR: Shixiong Han, B.Eng. (McMaster University)

SUPERVISOR: Dr. Mukesh Jain

NUMBER OF PAGES: xi, 184

Abstract

The drawability of sheet material in deep drawing followed by redrawing has not been studied theoretically in detail. The clamping force during deep drawing has not been properly simulated by FE method in the past due to the neglect of the operating machine stiffness. In addition, deep drawing process with centre hole blank has not been investigated in detail experimentally and numerically in the previous work. All of these aspects are studied in this work. A new FE model for deep drawing and redrawing has been developed, which accounts for the operating machine stiffness. In this model, the draw die is connected to a semi-rigid component of the test frame by some spring elements so that the stiffness of the operating machine can be controlled by the stiffness of these springs. Also, a mathematical model to determine the limiting drawing ratio (LDR) of deep drawing and redrawing processes has been derived based on the extension of an existing analytical model and Hill's anisotropic criterion. The results of the mathematical model have been validated by corresponding experimental and FE simulation work in terms of punch load and clamping force versus punch displacement and thickness distributions along the product profile. Furthermore, deep drawing with centre hole blank has been studied in terms of flanging ratio and the results of FE simulation are in good agreement with experimental work.

Acknowledgements

First of all, I'd appreciate my supervisor, Dr. Mukesh Jain for all his patient aids to my work. His strong academic background and experience really helped me to complete this thesis work.

I would also like to appreciate Dr. Mike Bruhis to assist me to conduct all the experiments.

The last but not the least, I am grateful for my dearest parents, Mrs. Jing Chen and Mr. Youtian Han. Their warm supports directly led me to the success of this job.

Table of Contents

Contents	Page
Descriptive Note	ii
Abstract	iii
Acknowledgements	iv
Table of Contents	v
List of Symbols	ix
Chapter 1 Introduction	1
1.1 Sheet Metal Forming, Cup Drawing and Redrawing.....	1
1.2 Research Objectives and Scope of Work.....	6
1.3 Research Methodology Overview.....	7
Chapter 2 Literature Review	9
2.1 Introduction.....	9
2.2 Analytical Modeling of Deep Drawing Process.....	10
2.2.1 General background.....	10
2.2.2 Schedin's expression for punch load as a function of punch displacement [8].....	11
2.2.3 Leu [1].....	12
2.2.4 Wan et al. [10-12].....	14
2.2.5 Remarks.....	16
2.3 Experimental Studies.....	17
2.3.1 Overview.....	17
2.3.2 Huang et al. [16-18].....	23
2.3.3 Jain et al. [21].....	24
2.3.4 Conclusion from experimental work.....	27
2.4 Finite Element Based Simulations of Deep Drawing Process.....	27

2.4.1 Introduction and history of finite element applications of deep drawing process.....	27
2.4.2 Element selection: axisymmetric versus 3D – shell models.....	30
2.4.3 Finite element approaches: static implicit versus dynamic explicit methods.....	32
2.4.4 Effect of numerical parameters on FE results.....	34
2.4.5 Summary of finite element simulation based studies.....	36
2.5 Review of Redrawing Process.....	36
2.5.1 Overview.....	36
2.5.2 MacPhee [37].....	37
2.5.3 Iseki et al. [38-41].....	41
2.5.4 Parsa et al. [42].....	42
2.5.5 Sonis et al. [43].....	43
2.5.6 Conclusion from redrawing studies.....	44
2.6 Brief Review of Deep drawing with Centre Hole Blank Process.....	44
2.6.1 Introduction.....	44
2.6.2 V. Marinkovic [44].....	45
2.6.3 Conclusion on deep drawing with centre hole blank process.....	48
2.7 Chapter Summary.....	48
Chapter 3 Proposed Analytical Model of Axisymmetric Redrawing Process..	49
3.1 General Characteristics.....	49
3.2 Model Development.....	52
3.2.1 Limiting drawing ratio of redrawing process, LDR_1	52
3.2.2 Limiting drawing ratio of deep drawing process, LDR_0	57
3.2.3 The overall limiting drawing ratio, LDR	58
Chapter 4 Experimental and FE Analysis Methodology.....	61
4.1 Introduction.....	61
4.2 Experimental Program.....	62
4.2.1 Sheet material.....	62

4.2.2 Equipment and apparatus.....	64
4.2.3 Problems, limitations and attempted solutions.....	68
4.3 Simulation Program.....	71
4.3.1 Software.....	71
4.3.2 Finite element modeling.....	72
4.3.3 Parameter control in pre-processing stage.....	77
4.3.4 Post-processing of FE simulation work.....	81
Chapter 5 Results and Discussion.....	85
5.1 Introduction.....	85
5.2 Experimental results.....	86
5.2.1 Deep drawing process.....	86
5.2.2 Redrawing process.....	93
5.2.3 A comparison of deep drawing and redrawing.....	97
5.2.4 Deep drawing process with centre hole blank.....	100
5.3 FE Simulation Results and Validation.....	106
5.3.1 A comparison of FE simulation and experimental results.....	106
5.3.2 Process signatures and strain paths in deep drawing versus forming limit diagram.....	112
5.3.3 Influence of tooling geometry on drawability of sheet material.....	116
5.3.4 Determination of LDR from FE simulations.....	120
5.4 Theoretical Results and Validation.....	123
5.4.1 Mathematical model validation.....	123
5.4.2 Influence of material and tool geometric parameters on drawability using the theoretical model.....	124
Chapter 6 Conclusions and Future Work.....	131
6.1 Conclusions.....	131
6.2 Future Work.....	133
6.2.1 Deep drawing process.....	133
6.2.2 Redrawing process.....	133

6.2.3 Deep drawing process with centre hole blank.....	134
References	135
Appendices	140
Appendix A: Detailed Derivation of Daw-Kwei Leu’s Work [1].....	141
Appendix B: Detailed Derivation of Wang’s Conical Cup Model [10-12]...	152
Appendix C: Effect of Numerical Parameters on FE results.....	157
Appendix D: Detailed Derivation of Iseki’s Work [38-41].....	158
Appendix E: Detailed Calculation to Solve Equation (3.8, 3.9).....	162
Appendix F: Detailed Derivation of LDR_0 with Critical Effective Strain	
Value of $\bar{\epsilon} = \frac{1 + \bar{R}}{\sqrt{1 + 2\bar{R}}} n - \ln\left(\frac{r_1}{r_{11}}\right)$	164
Appendix G: Comparison of Experimental and Simulation Results.....	168
Appendix H: Logical Flow Chart of Simulation Set Up to Determine	
Limiting Drawing Ratio of Deep Drawing and Redrawing	
Operations and Critical Flanging Ratios for Deep Drawing	
with Centre Hole Blanks.....	177
Appendix I: Simulation Results to Determine Limiting Drawing Ratio of	
Deep Drawing and Redrawing Processes.....	180

List of Symbols:

$\bar{\sigma}, \bar{\epsilon}$ = Effective stress and strain

K = Material strength factor

n = Material strain hardening exponent

\bar{R} = Average normal anisotropy

$R_{0^\circ}, R_{45^\circ}, R_{90^\circ}$ = Normal anisotropy values at 0° , 45° and 90°

$\sigma_r, \sigma_\theta, \sigma_z$ = Stresses in r , θ and z directions

$d\epsilon_r, d\epsilon_\theta, d\epsilon_z$ = Strain increments in r , θ and z directions

t_0 = Initial blank sheet thickness

t = Sheet thickness after the cup is drawn

t_r = Thickness reduction

r_1 = Punch radius of deep drawing process

r_p = Punch profile radius of deep drawing process

r_{die} = Die radius of deep drawing process

r_d = Die corner radius of deep drawing process

c = Clearance between punch and die in deep drawing process = $\frac{1}{2}(r_{die} - r_1)$

r_{11} = Punch radius of the first redrawing process

r_{d1} = Die corner radius of the first redrawing process

R_0 = Initial blank sheet radius

ρ_0 = Initial center hole radius of the blank

r_0 = Radius of annular ring drawn from R_0

r_{01} = Radius of annular ring drawn from r_{21}

r_N = Radius of the critical section, which is the corner section

R_1, R_2 = Intermediate radii of annular rings in flange region, which draw into die to r_1 and r_2

R_{11}, R_{21} = Intermediate radii of annular rings in flange region of deep drawn cup, which draw into die to r_{11} and r_{21}

H = Deep drawn cup depth or punch displacement

H_1 = Redrawn cup depth or punch displacement

R = Blank radius at current deep drawn cup depth h

L = Finished deep drawn cup height

L_1 = Finished redrawn cup height

Z = Distance redrawn cup has traveled into the die

P = Drawing force in deep drawing process

P_1 = Drawing force in redrawing process

Q = Blank holding force

F_B = Bending load

F_{total} = Total punch load in redrawing process

P_c = Critical drawing force

μ = Single-valued Coulomb friction coefficient

σ_c = Critical stress

σ_{r0} = Radial friction stress at position r_0 for deep drawing process

σ_{r01} = Radial friction stress at position r_{01} for redrawing process

σ_y = Material yield stress

σ_{UTS} = Material ultimate tensile stress

σ_{rN} = Stress at critical section, which is the corner section

β = Stress ratio = $\frac{\sigma_\theta}{\sigma_r}$

ϵ_0 = Natural strain due to deep drawing

ε_1 = Natural strain due to redrawing

ε_T = Total strain = $\delta_0 + \delta_1$

ε_{\max} = Maximum natural strain in the redrawn cup = $\ln \sqrt{4LTD + 1}$

α = Semi-conical angle

ϕ = Contact angle of the blank with punch profile = $\frac{\pi}{2} - \alpha$

A_0 = Initial section area of tensile test sample

A_j = Necking section area of tensile test sample

LDR = Overall limiting drawing ratio

LDR_0 = Limiting drawing ratio of deep drawing process

LDR_1 = Limiting drawing ratio of the first redrawing process

k_p = Flanging ratio

LTD = Length to diameter ratio of the redrawn cup

$\%RA$ = Percent reduction in area in redraw

Chapter 1 Introduction

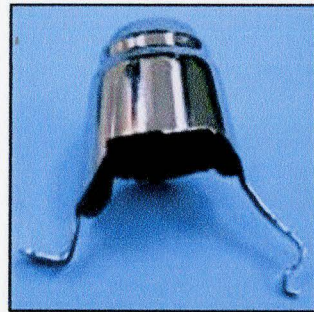
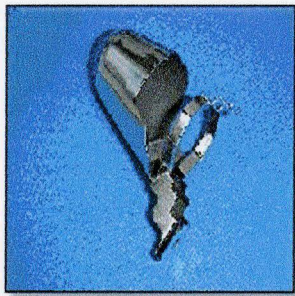
1.1 Sheet Metal Forming, Cup Drawing and Redrawing

Sheet metal forming technology plays a very important role in manufacturing industries, especially in automotive, electronic and appliance areas. Figure 1.1(a) shows some sheet metal parts produced on a sheet forming press. Deep drawing is a sheet metal forming process that is widely used in industry to fabricate many automotive parts, as shown in Figure 1.1(b). This process not only involves stretching of sheet metal blank but also drawing, using a flat-bottom punch, which has tapered or rounded corner to produce a hollow vessel from the blank sheet. The edges of the metal blank are usually restrained by a blank holder and the sheet is drawn into a die cavity to achieve the end shape that is desired. There are many shapes that can be made through deep drawing process, such as cups, pans, cylinders, domes or hemispheres, as well as irregular shaped products. Redrawing process is considered for changing the lateral dimensions of the product, which is created from deep drawing and redrawing results in an increase in the

product depth and a decrease in its section area. The combination of these two processes is usually applied to the machine line in the formation of many types of sheet metal parts, such as light bulb shield of a car (Figure 1.1(b)). This combination is also referred to as progressive drawing process. An example of this process to produce an automotive bulb shield component is shown in Figure 1.1(c).



(a)



(b)



(c)

Figure 1.1 Sheet metal forming products from (a) stamping, (b) deep drawing and (c) progressive drawing

If the product has a round or axisymmetric shape, the operation can also be called cup drawing, a special case of deep drawing process. In this thesis, the research is focused on this particular type of drawing process and, therefore, the term ‘deep drawing’ mentioned hereafter is equivalent to ‘cup drawing’. Furthermore, if the blank is prepared with an initial centre hole, the term ‘deep drawing with centre hole blank’ can be used. Some investigation on this particular deep drawing process is also involved in this thesis because it can be extremely suitable if a cylindrical automotive part has a centre hole profile at bottom and low precision is required, because it is much easier and more economical to fabricate the blanks before the process than trimming the holes from the drawn products afterwards.

Generally, cup drawing production process starts with part design and tooling design. The part is usually designed at first to fulfill a particular function in service and the tooling design is based on the corresponding part design and the forming process sequence or stages. The tooling for the first deep drawing stage usually consists of a punch, a die to form the product shape, and a blank holder to provide the clamping force, as shown in Figure 1.2(a). The punch moves up through the opening in the blank holder to contact and draw the blank into the die cavity to form a cup. Several parameters, such as the punch diameter, the clearance between the punch and die, the punch and die corner radii etc., have to be taken into consideration, as they will directly affect the shape, formability and quality of the final product. If they are not designed properly, two failure modes, necking causing cracking or wrinkling, will occur during the process. Sometimes the product requires a relatively large depth compared to the cup diameter. In this case,

the final profile cannot be achieved in one drawing stage, and one or more redrawing processes may be necessary. In most cases, the tooling for redrawing only includes a punch and a die, as shown in Figure 1.2(b). However, problems such as cracking and wrinkling can occur when they are not properly designed. As well, the process design, such as the number of redrawing stages, is an important factor to be considered in the redrawing process.

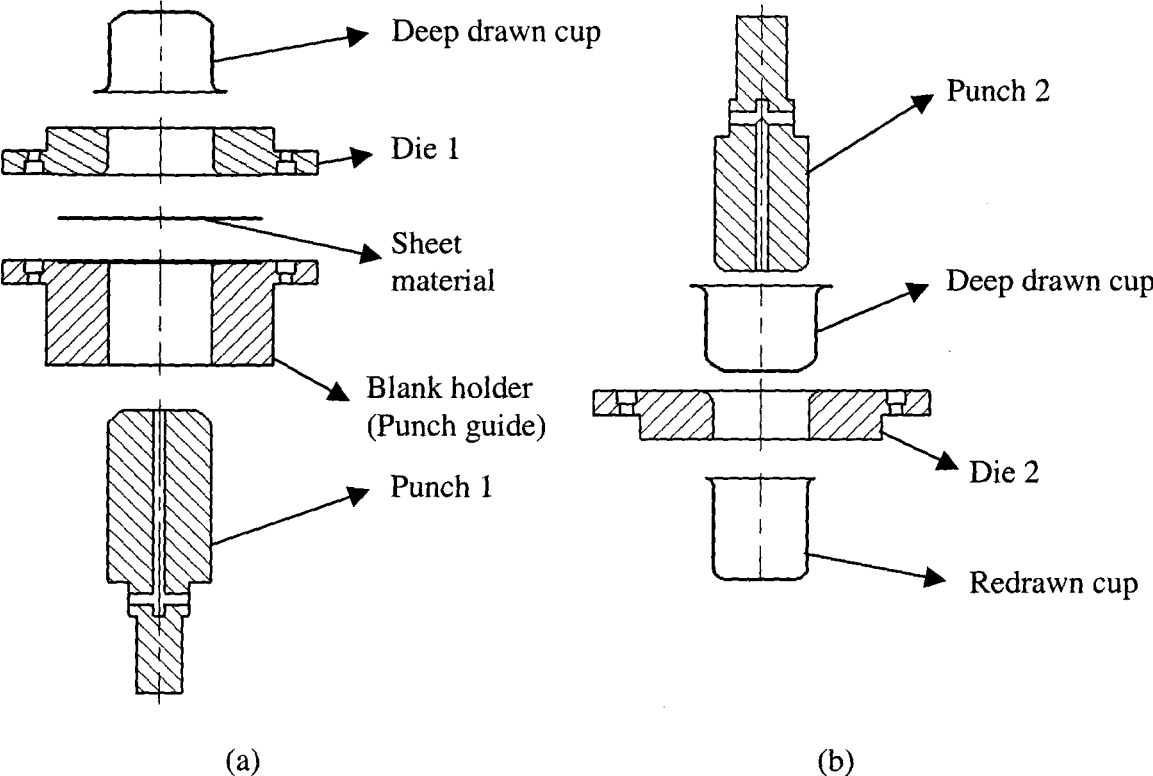


Figure 1.2 Tooling demonstrations of (a) deep drawing and (b) redrawing

In order to obtain high quality products in industries, a number of researches related to this technology, based on the parameters mentioned above, have been carried out in the

past few decades. The purpose is often to find the formability of a sheet material, which is normally represented by the term 'limiting drawing ratio' or LDR. The LDR, being the ratio of the maximum possible initial blank diameter that can be drawn into a cup to the punch diameter, provides a measure of drawability of sheet metal. Similarly, the ratio of the first punch diameter to the second punch diameter for redrawing is used as a measure of redrawability.

So far, the LDRs of deep drawing for some commercial sheet metals have been well investigated, including experimental data, finite element simulation and detailed theoretical model, so that the process has been well understood in most situations. On the other hand, a few researches have been investigated on deep drawing with centre hole blank process in the literature, either experimentally or numerically. It is necessary to develop more experimental and FE simulation work to provide a better understanding of this process. Furthermore, for redrawing operation, most researches have been carried out only experimentally. However, experimental assessment of redrawability is very time consuming as it employs many procedural steps and requires a large number of experiments. In addition, in order to predict forming outcome under different conditions, various tooling geometries and extensive sheet material supply are required that can be costly. A few finite element (FE) simulations of redrawing process have also been reported in the literature, but not many useful results have been published.

Therefore, it is necessary to develop a suitable mathematical model for redrawing process to predict the LDR that can provide a rapid assessment of redrawability as a function of material properties, tooling geometries and process parameters. Also, a

representative FE model should also be developed to predict the material flow behavior during this operation. The advantage of a mathematical or FE model is to drastically reduce the time and effort spent on the experiments, and lead the experimental work in the right direction. Furthermore, for research purpose, it is very helpful to understand the material plastic flow in this operation, so that this technology can be controlled and optimized for robust manufacturing.

1.2 Research Objectives and Scope of Work

Based on the problems defined above, the research objectives of this thesis can be stated as follows:

- (1) Develop a suitable mathematical model of mechanics of redrawing process to predict the formability of a given material under realistic process conditions and validate this model by experimental work and compare with finite element simulations so that the effects of material properties and tooling geometric parameters on LDR can be studied theoretically.
- (2) Investigate deep drawing process with centre hole experimentally and numerically.
- (3) Develop a better understanding of material behaviors during drawing processes.

To achieve these objectives, the research scope has been restricted to the following selection:

- (1) The sheet material utilized is stainless steel 304 with a thickness of 0.5 mm.
- (2) Only one redrawing stage after deep drawing has been analyzed.

- (3) For the redrawing stage investigated in this work, no blank holder will be included in the analysis.
- (4) Coulomb friction model is applied to all the tool-sheet contacting surfaces.

1.3 Research Methodology Overview

The research procedure can be expanded into four sections, as shown below:

- (1) Development of an analytical model

A theoretical development that can predict the LDRs of sheet metals during redrawing process is carried out based on the theory of plasticity. This work is an extension of an existing mathematical model of deep drawing by Leu [1]. The new mathematical model includes most of the important parameters such as material properties, tooling profiles and friction condition, so that the effect of each factor can be carefully studied.

- (2) Experimental work

Experimental work is conducted using a 25-kip, two-actuator, servo-hydraulic mechanical test system (MTS). The cup drawing and redrawing tooling was designed and fabricated in house for the above test frame. The purpose of experiments was to provide a reference for both theoretical and FE simulation work. In the experiments, the drawing force for both drawing and redrawing stages and clamping force for deep drawing only, was recorded as a function of punch displacement by MTS machine's PC based control and data acquisition system. After the cup was drawn, the strain

distributions of the cups were measured by a surface grid-based optical strain measurement system (Argus system by GOM, Germany).

(3) Finite element modeling

Deep drawing, redrawing and deep drawing with centre hole blank operations were simulated by commercial finite element software (LS-DYNA3D) close to the conditions of the experiment. The model was validated by comparing the simulation results with the experiments. This includes a comparison of the punch and clamping loads and strain distributions along the profile of the drawn and redrawn cups. Once good agreement between finite element model and experiment was achieved, the model was run repeatedly to predict drawing and redrawing behaviors under different conditions.

(4) Validation of analytical model

Finally, different parameter values were input to the analytical model to predict the LDRs for redrawing process under different conditions. These predictions could be compared with the results of finite element model, which was validated by experimental work.

Chapter 2 Literature Review

2.1 Introduction

Sheet metal forming technologies began to be popular in the middle of 20th century, due to the fast development of automotive industry. Research on deep drawing process started at the beginning of 1960's and became well-organized 10 years later. Because of the advanced automotive industry at that time, this technology developed very quickly in US, UK, Europe and Japan. It became widely utilized by many car companies, such as GM, Ford, Mercedes, Audi, Honda, and etc., to produce some typical automotive parts. In the past four decades, research on this topic was focused on the drawability of different materials, represented by the term 'limiting drawing ratio', as mentioned in Chapter 1. The research on cup drawing, redrawing and other related processes have continued in three different ways: analytical, experimental and finite element analysis of the process to study aspects of intrinsic material properties, material flow in the die cavity, friction, and tool and sheet surface modification.

2.2 Analytical Modeling of Deep Drawing Process

2.2.1 General background

The objective of the analytical work is to find the exact relationships between LDR and other material and process parameters. Swift and Chung [2] first started to analyze the deep drawing process in 1952. In 1969, Takeuchi et al. [3] published a paper, which described the effects of punch diameter and sheet thickness on the limiting drawing ratio. In the same year, Woodthorpe [4] studied the effect of anisotropy and strain hardening coefficient upon the deep drawability of sheet steel. Subsequent researches utilized a combined experimental and theoretical approach to relate the tooling profiles and material properties. In 1970, Chakrabarty et al. [5] proposed a new theoretical approach to predict the LDR for a severely work-hardened material. Kaftanoglu [6] indicated that the cup depth at fracture to blank diameter curves for oversize blanks can be expressed by a particular type of exponential expression in 1974. In 1993, Bayoumi [7] described the friction and bending effects on limiting drawing ratio and took into consideration two instability conditions: the instability under plane strain conditions, which usually occurs in conventional deep drawing process and the instability under uniaxial tension, which generally happens during unconventional deep drawing operation. All the previous theoretical researches have shown that there are three major parameters affecting the LDR of drawing process and they are tooling geometry, such as punch diameter and die profile radius, material properties, including anisotropy and strain-hardening exponent, and the friction between the blank and tooling (punch, blank holder and die).

2.2.2 Schedin's expression for punch load as a function of punch displacement [8]

As mentioned before, the LDR is commonly obtained from the critical drawing load in the process, so the prediction of drawing force is necessary and useful. This topic has been already included in much of the previous work, but the most detailed study was carried out by E. Schedin [8]. In 1991, Schedin derived an expression for punch load as a function of punch displacement (or cup height), which combined all the deformation characteristics in a deep drawing process. They are plastic deformation due to flange shrinking, plastic deformation due to bending and unbending at the die edge, friction at the flange rim and friction at the die edge. The following expression for drawing load as a function of cup height H was obtained:

$$P = 2\pi r_1 t_0 \left\{ e^{\frac{\mu\pi}{2}} \left[K \left(\frac{2b}{b+1} \right)^{\frac{1+n}{2}} \int_{r=r_1}^{r=R} \left(\ln \sqrt{1 + \frac{2r_1 H}{r^2}} \right)^n \frac{dr}{r} + \frac{Q\mu}{\pi R t_0} \right] + \frac{t_0 K}{2r_d} \left(\frac{2b}{b+1} \right)^{\frac{n}{2}} \left(\ln \sqrt{1 + \frac{2H}{r_1}} \right)^n \right\} \quad (2.1)$$

where: $b = \frac{1 + \bar{R}}{\bar{R}}$

Assumptions made in this work were that no thickness change occurred in cup flange area during the operation, and the cup was perfectly cylindrical. The advantage of this model was that it tracked the punch force for the whole process. The other models provided only the limit load, as discussed later in this chapter.

2.2.3 Leu [1]

In 1998, D.K. Leu established a detailed mathematical model to predict LDR, which included the effects of material properties, tool geometries and friction. A schematic of the cup drawing process from Leu's work is shown in Figure 2.1. It shows the deep drawing operation under consideration that a circular sheet blank of original radius R_0 and thickness t_0 is drawn by the flat-bottomed punch through a die opening of radius r_1 with a constant clearance blank holder.

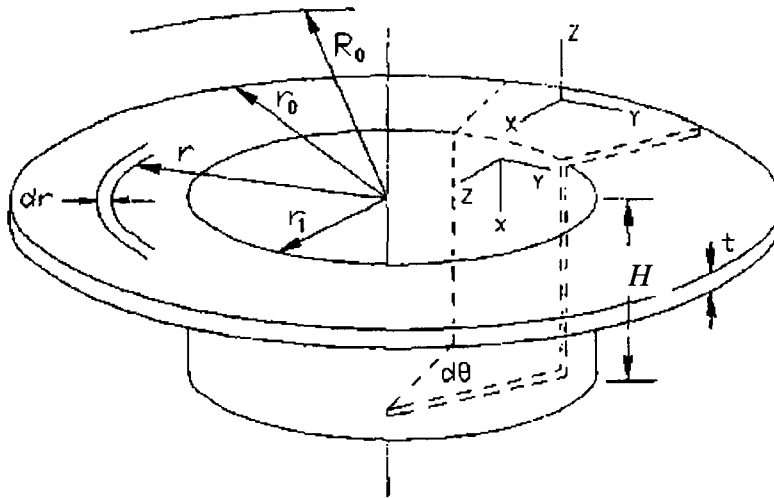


Figure 2.1 Schematic representation of a drawn cup showing the coordinate system and the dimensional notation [1]

In this model, the material is assumed to follow the Hollomon's strain hardening expression, which gives:

$$\bar{\sigma} = K \bar{\epsilon}^n \quad (2.2)$$

where:

$\bar{\sigma}, \bar{\varepsilon}$ = Effective stress and strain

K = Material strength factor

and n = Material strain hardening exponent

The average normal anisotropy \bar{R} of the material was evaluated using:

$$\bar{R} = \frac{R_{0^\circ} + 2R_{45^\circ} + R_{90^\circ}}{4} \quad (2.3)$$

Hill's quadratic anisotropic yield criterion and corresponding flow rule [9] were utilized with the following equation from the incremental theory of anisotropic plasticity, as shown below:

$$\bar{\sigma} = \sqrt{\frac{1}{1+R} \left[(\sigma_\theta - \sigma_z)^2 + (\sigma_r - \sigma_z)^2 + \bar{R}(\sigma_r - \sigma_\theta)^2 \right]^{1/2}} \quad (2.4)$$

$$d\bar{\varepsilon} = \frac{\sqrt{1+R}}{1+2R} \left[(d\varepsilon_\theta - \bar{R}d\varepsilon_z)^2 + (d\varepsilon_r - \bar{R}d\varepsilon_z)^2 + \bar{R}(d\varepsilon_r - d\varepsilon_\theta)^2 \right]^{1/2} \quad (2.5)$$

$$\begin{aligned} \frac{d\varepsilon_r}{\bar{R}(\sigma_r - \sigma_\theta) + (\sigma_r - \sigma_z)} &= \frac{d\varepsilon_\theta}{\bar{R}(\sigma_\theta - \sigma_r) + (\sigma_\theta - \sigma_z)} \\ &= \frac{d\varepsilon_z}{(\sigma_z - \sigma_\theta) + (\sigma_z - \sigma_r)} = \frac{d\bar{\varepsilon}}{(1+R)\bar{\sigma}} \end{aligned} \quad (2.6)$$

The maximum drawing load P_c can be calculated by the following formula:

$$P_c = 2\pi r_1 t_0 \left(\frac{1+\bar{R}}{\sqrt{1+2\bar{R}}} \right)^{1+n} (n^n e^{-n} K) \quad (2.7)$$

Critical effective strain corresponding to P_c is given by $\bar{\varepsilon} = \frac{1+\bar{R}}{\sqrt{1+2\bar{R}}} n$.

This analytical model provides an expression for the maximum drawing load based on the critical effective strain. Schedin's expression, on the other hand, represents the

relationship between the punch load and punch displacement at every time step. It was reasonable to use Leu's method to find LDR, because LDR itself is a critical value. Analytical equations and procedures for determination of the final mathematical expression for LDR as a function of material properties, tooling geometrical parameters and friction coefficient at flange region, are described in detail in Appendix A.

This model has two major limitations. As shown in Figure 2.1, the cup was assumed to be perfectly vertical instead of a conical profile. In addition, there was no blank holder included in the model, so that the friction between the sheet material and die surface was considered lower than the real situation.

2.2.4 Wan et al. [10-12]

Wan et al. developed an analytical model for conical cups. In this model, the effect of die clearance and clamping force were both considered, as shown below in Figure 2.2. Also, the model utilized Hollomon's expression to describe the material properties and Hill's anisotropic criterion to establish the stress-strain relationships. The stress state at the critical section, the corner of the cup where necking phenomena usually happens, were considered in this model, as shown in Figure 2.3.

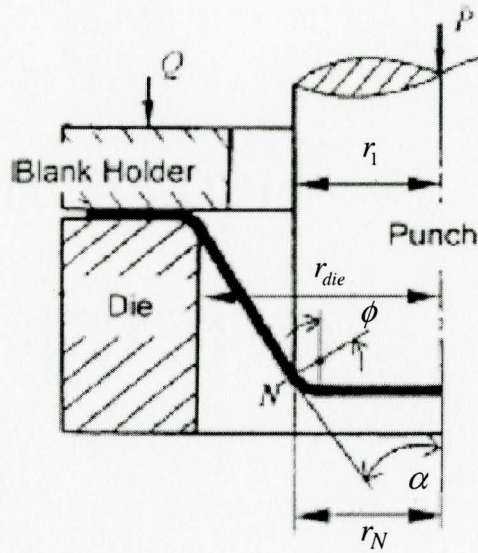


Figure 2.2 Illustration of a conical cup drawing [12]

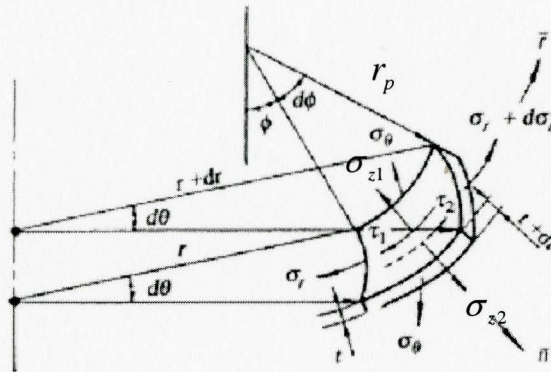


Figure 2.3 Stress state on the critical section [11]

By setting up and solving the normal equilibrium equation at the corner section, the limit stress σ_c was obtained as:

$$\sigma_c = C \left(\frac{1 + \bar{R}}{\sqrt{1 + 2\bar{R}}} \right)^{1+n} e^n \sigma_{UTS} \quad (2.8)$$

where:

$$C = \frac{1}{1 + \bar{R}} \frac{1 + \bar{R} + \frac{t_0 e^{-n} \cos \alpha}{r_1 - r_p + \left(r_p + \frac{1}{2} t_0 e^{-n}\right) \cos \alpha}}{1 + \frac{t_0 e^{-n} \cos \alpha}{r_1 - r_p + \left(r_p + \frac{1}{2} t_0 e^{-n}\right) \cos \alpha + \frac{t_0 e^{-n}}{r_p + \frac{1}{2} t_0 e^{-n}}}}$$

The detailed derivation of LDR using this model is given in Appendix B.

This model did include many relevant parameters that can affect the result of the whole deep drawing operation. However, the solution utilizes the assumption of $\frac{r_0}{R_0} \approx 0.9$ to obtain the expression for maximum radial drawing stress, $\sigma_{rN \max}$ as explained in Appendix B. This assumption is based on some experimental experience and needs to be verified for different materials. Because the model consisted of too many parameters, the authors simplified the model to obtain a numerical solution, although it would affect the final result. Overall, the analytical model can well represent the deep drawing operation and the theoretical results are reasonable compared to the experiments.

2.2.5 Remarks

Theoretical models can represent LDR as a function of all the parameters in consideration so that the sensitivity of LDR by altering each parameter can be obtained. However, due to the difficulty of solving complex partial differential equations, some assumptions could not be avoided, which will affect the final results. It is for this reason that proper experimental verification of the models is essential. Also, there is no suitable

analytical redrawing model that exists in the literature, which are reviewed in Section 2.5, so it is necessary to carry further work on this subject.

2.3 Experimental Studies

2.3.1 Overview

Deep drawing experiments have been conducted by many researchers in the past few decades. The purpose has been mostly to determine the effects of different material and process parameters on LDR. Also, the experimental results have been used to validate the theoretical and numerical predictions. An overview of experimental aspects of deep drawability in terms of material, tooling and test equipment is given below.

(1) Materials

Steel and aluminum are perhaps the most commonly used commercial sheet metals, so most of the experimental work has been focused on these two types of materials. The two materials have quite different properties, as shown in Table 2.1. Generally, steels exhibit better deep drawability than aluminum, because they usually have larger elongations at break and possess strain ratio (R value) greater than 1. R value represents the resistance to thinning and correlates directly with LDR.

Table 2.1 Mechanical properties of steel and aluminum sheet materials

Material	E (GPa)	σ_y (MPa)	σ_{UTS} (MPa)	$Elong$ (%)	n	R value
Aluminum						
AA 3003	68.9	41.4	110	35	0.23	0.723
AA 5182	69.6	130	275	21	0.23	0.710
AA 5754	67.4	104.5	224	24	0.31	0.693
Al 6061	68.9	48.3	117	25	0.26	0.672
AA 6111	69.5	165	291	23	0.24	0.655
Steel						
SS 304	193	215	505	70	0.36	1.168
SS 310	200	310	620	45	0.35	1.132
SS 316	193	290	580	50	0.34	1.155
ASTM A29	200	315	420	39	0.31	1.043
ASTM A322	200	434	703	25.5	0.32	1.012

From the table above, it is noted that Stainless Steel 304 has a very large elongation value at break as well as a large n value but the rest of the properties are very similar to the other steels. Furthermore, this material also has a relatively larger anisotropy value, compared to the other steels. This is why SS304 is widely used for many deep drawing applications in industry.

(2) Tooling profiles

Two tool geometric parameters: punch-die clearance and die corner radius have been reported to be critical for LDR. In general, LDR decreases with an increase in

clearance and a decrease in die corner radius. The punch profile radius also has minor effect on LDR in the deep drawing process from the information in the literature.

(3) Equipments

For research purposes, the deep drawing operation is usually conducted by hydraulic or mechanical presses or modified standard tensile test machines such as the one shown in Figure 2.4. The deep drawing process can be carried out by configuring the tooling in such a way that the punch can be moved either upwards or downwards to form a cup (Figure 2.5).



Figure 2.4 Deep drawing equipment: modified tensile testing machine

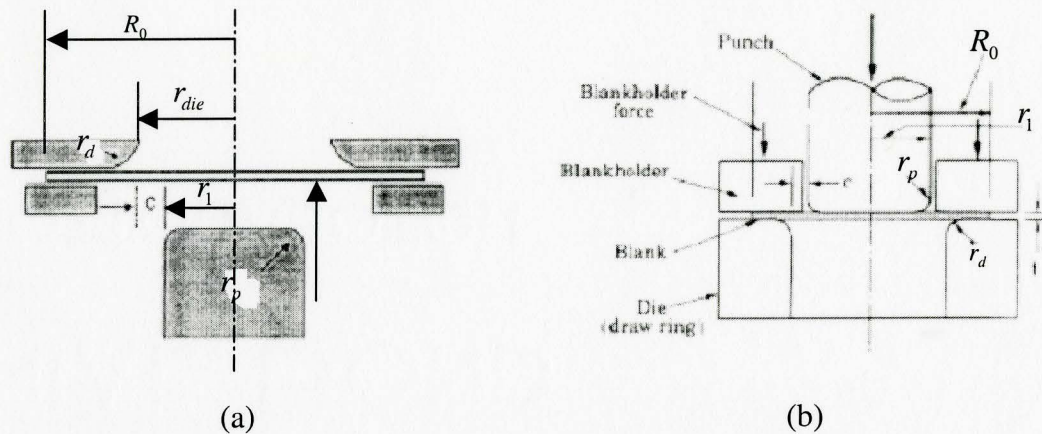


Figure 2.5 Demonstration of deep drawing process using a modified standard tensile test machine with:
 (a) punch moving upward [21], (b) punch moving downward [24]

Swift and Chung [2] first conducted deep drawing experiment in 1952. Since then, a number of researchers have made experimental investigations on this process with various materials and under different conditions. A brief review of deep drawing experimental work is shown in Table 2.2.

Table 2.2 A brief review of experimental work of deep drawing in history

Author	Year	Material	Process variables and tooling geometry (All units in mm)	Remarks
Swift et al. [2]	1952	Aluminum	Not specified	First experimental investigation of deep drawing process in the literature
Whiteley [13]	1960	Soft Aluminum	Not specified	Detailed experimental demonstration of deep drawing process

Takeuchi et al. [3]	1969	Pure Aluminum	$r_1 = 30, 54, 120, 180$ $t_0 = 0.6, 0.8, 1.0, 1.2$	The LDR \downarrow linearly with r_1/t_0 \uparrow
Kaftanoglu [6]	1974	Ferrous and Non-Ferrous Material	Not specified	Cup depth at fracture was obtained by using oversize blank to obtain LDR value
Kawai et al. [14]	1988	Pure Aluminum	Not specified	Confirmed that LDR \uparrow nonlinearly with \bar{R} \uparrow
Saran et al. [15]	1990	Quality Steel Brass Stainless Steel Aluminum	Not specified	Predicted P , ε , and flange reduction were compared with the corresponding experiment work
Bayoumi et al. [7]	1993	Anisotropic work-hardening material	$\mu = 0.0, 0.05, 0.1, 0.2$	Studied the friction and bending effects on LDR in deep drawing process
Huang et al. [16-18]	1994	BA-DDQ Steel	$r_1 = 30$ $r_p = 8$ $t_0 = 1.2$ $r_{die} = 31.25, 31.38, 31.46$ $r_d = 4.8, 10, 12, 14$ $\mu = 0.02, 0.05, 0.15, 0.2$	Studied the influence of c , r_d and μ on LDR experimentally and compared with FE simulation results
Moshksar et al. [19]	1997	Pure Aluminum	$r_1 = 20$ $r_{die} = 22$ $t_0 = 1.5$ $r_p = 4, 6, 8, 10, 12$ $r_d = 4, 6, 8, 10, 12$	Studied the effect of r_d and r_p on LDR to optimize tool geometries
Zaky et al. [20]	1998	BA-DDQ Steel Pure Aluminum	$r_1 = 20$ $r_p = 4.0$ $r_{die} = 21.4$ $r_d = 10.0$ $t_0 = 1.0$	Found the optimum blank shape of cylindrical cups of anisotropic sheet metals

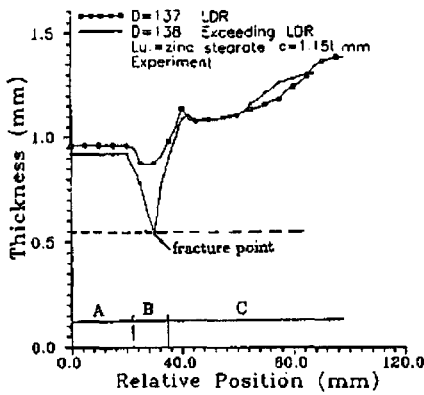
Leu [1]	1999	CA-DDQ Steel BA-DDQ Steel BA-CQ2 Steel	$r_1 = 30.65, 30.75, 30.78, 30.86$ $r_d = 5.4, 8.5, 8.6, 10.6, 12.6, 14.6$ $\mu = 0.1, 0.2$	Compared the analytical LDR values with experimental outcomes under various drawing conditions
Jain et al. [21]	1998	AA5754-0 AA6111-T4	$r_1 = 74.995$ $r_p = 12$ $r_{die} = 76.915$ $r_d = 3, 6, 9, 12$	Achieved P VS H curve, flange draw-in as measured by LVDT as a function of H , and the effect of r_d on LDR
Kishor et al. [22]	2002	EDD Steel	$r_1 = 19.5$ $r_p = 4$ $r_{die} = 20.7$ $r_d = 6$ $t_0 = 1$	Obtained LDR value experimentally as well as optimized the initial blank shape to minimize earing in deep drawing
Natarajan et al. [23]	2002	AA1100-0	$r_1 = 50$ $t_0 = 0.8$	Obtained LDR value experimentally and measured surface ε in different directions
Colgan et al. [24]	2003	Mild Steel EN10130 FeP01	$r_1 = 19.7$ $r_p = 2$ $r_{die} = 20.85$ $r_d = 2$ $t_0 = 1$	Compared experimental LDR values with FEA predicted magnitudes

Some particularly noteworthy studies in recent years are discussed below.

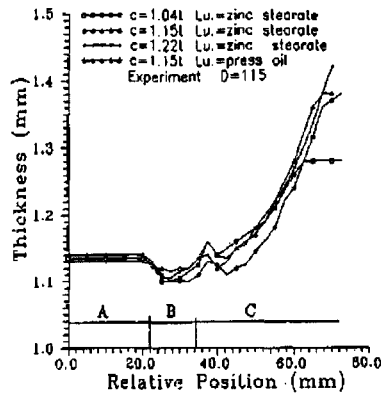
2.3.2 Huang et al. [16-18]

This research was focused on the effect of tool clearance, friction coefficient and die corner radius on LDR during deep drawing of a low carbon steel, as shown in Table 2.2. The thickness distributions at LDR and exceeding LDR were plotted along the cup profile, as shown in Figure 2.6(a). By changing the tooling clearance, lubrication and die corner radius, thickness distributions at different conditions could be plotted to find the influence of the above factors on LDR, as shown in Figure 2.6(b, c). The LDRs for different conditions were determined by repeating the same procedure. Predictably, the thinnest area is at location B of the cup, the punch nose area, where the material is most likely to be under a plane strain state and becomes the site of neck initiation. On the other hand, the thickest part is the top of the cup because the material comes from the outmost flange area, where the material is likely to be under a circumferential compression state where some flange thickening occurs.

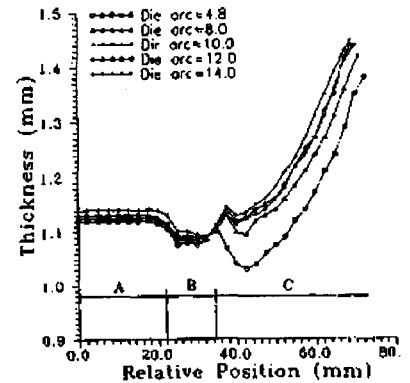
Three conclusions could be drawn from this set of experiments: (1) the sheet metal has the best drawability when the tool clearance is $1.15t_0$ (t_0 = initial blank thickness), (2) a lower value of friction coefficient in the flange region can provide a better limiting drawing ratio, and (3) increasing the die corner radius can increase the LDR.



(a)



(b)



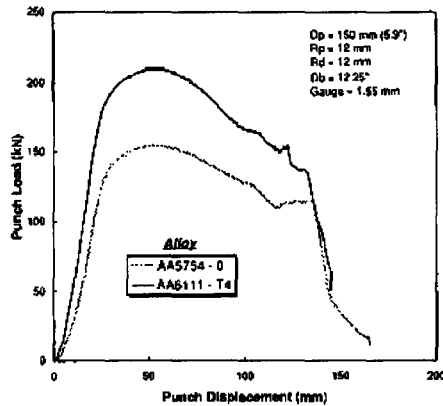
(c)

Figure 2.6 Experimental thickness distribution comparisons along the cup: (a) at LDR and exceeding LDR [16], (b) with different tool clearances and lubrications [17] and (c) with different die arc radii [18]

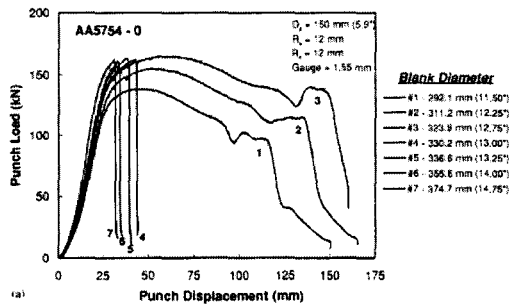
2.3.3 Jain et al. [21]

Deep drawing characteristics of automotive aluminum alloys were studied by Jain et al [21]. LDRs of two commercially produced automotive aluminum sheet material, AA5754 and AA6111, were obtained under different drawing conditions.

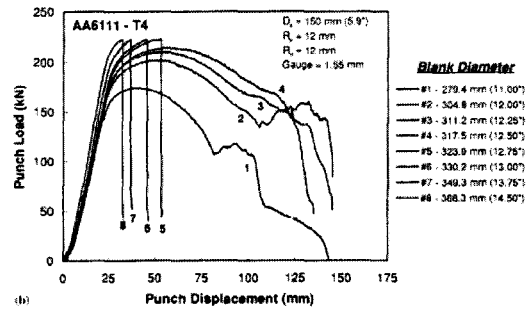
Figure 2.7(a) shows a typical punch load versus punch displacement curve in deep drawing operation for both materials. It is reasonable in the figure that the load curve of AA6111 has a higher peak than that of AA5754, because it has larger yield and tensile strength. Figure 2.7(b, c) shows the detailed punch load versus displacement curves with various initial blank sizes for both materials.



(a)



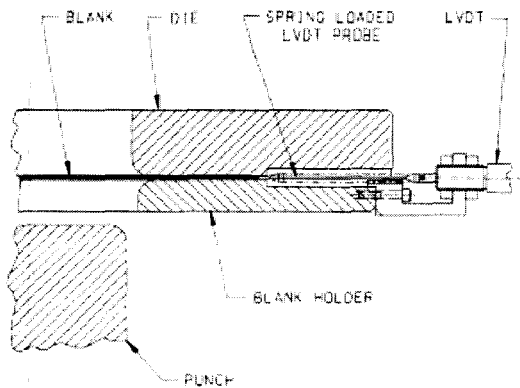
(b)



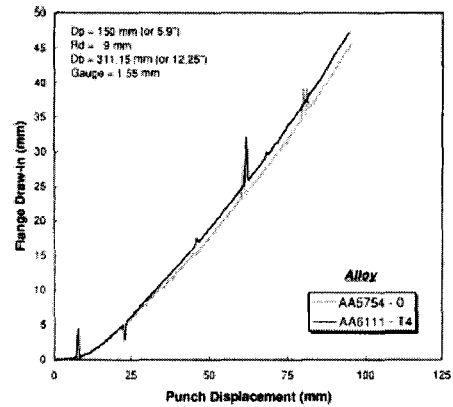
(c)

Figure 2.7 Punch forces VS punch displacement curves: (a) comparison of AA5754 and AA6111, (b) AA5754 with different blank diameters, and (C) AA6111 with different blank diameters [21]

Furthermore, an important part of this experimental work was that it made measurements of flange draw-in during the test by using a especially designed LVDT. The flange displacement was measured continuously as a function of punch displacement in the process. The detailed setup for this LVDT equipment is shown in Figure 2.8(a) and the relationship between flange draw-in and punch displacement is shown in Figure 2.8(b).



(a)



(b)

Figure 2.8 Illustration of (a) LVDT setup and (b) flange draw-in distances versus punch displacements [21]

The conclusions made were that the LDR is proportional to the die corner radius and the strain-hardening exponent of the material. Three important contributions of this experimental work were in terms of development of punch load and punch displacement curves, influence of die profile radius and strain-hardening exponent of material on LDR, and exploration of the relationship between flange draw-in distance and punch displacement. Although the investigation of thickness distribution was also made, the strains were measured only at 4 points along the cup, while 20 points were used to plot the thickness in work of Huang et al. [16-18].

2.3.4 Conclusion from experimental work

The influence of various parameters on LDR is summarized in Table 2.3.

Table 2.3 Relationship between LDR and effective parameters

Parameter	Status	LDR
Optimum Tooling clearance	1.15t	Max LDR
Die corner radius	Increasing	Increasing
Punch profile radius	Increasing or decreasing	Minor effect
Friction coefficient	Increasing	Decreasing
Strain-hardening exponent	Increasing	Increasing
Anisotropy	Increasing	Increasing

Although experiments provide reliable LDR values, the laboratory test conditions cover only a limited range of variables. Analytical models, if properly validated, can lead to a more comprehensive understanding of the interplay between the different material, tooling and process parameters.

FE models of deep drawing process are briefly reviewed in the following section.

2.4 Finite Element Based Simulations of Deep Drawing Process

2.4.1 Introduction and history of finite element applications of deep drawing process

Finite Element Analysis (FEA) was first developed in 1943 by R. Courant [25], who utilized the Ritz method of numerical analysis and minimization of variational calculus to

obtain approximate solutions to vibration systems. It started to be applied in metal forming research area in 1970s and fast developed in the next two decades. FEA is also widely used to simulate deep drawing process to analyze the drawing behavior of sheet metals. The results are gradually improving, compared with experiments, due to the improvement in the FEA software. Furthermore, the FEA of sheet metal forming has become an important research subject (refer to several Numisheet conferences in the last 10 to 15 years). Table 2.4 provides a summary of FE based studies of deep drawing in the past.

Table 2.4 A brief review of FE work of deep drawing in history

Author	Year	Model Characteristics		Contributions
		Element Type	Remarks	
Gotoh et al. [26]	1978	Axisymmetric	Obtained a general formulation for FEA of very large rigid-plastic deformation	Proposed a fourth-degree yield function that results in better prediction in the shape of the deformed flange
Onate et al. [27]	1983	Axisymmetric 3D - Shell	Extended the visco-plastic flow theory for continuum problems to deal with thin sheet	Numerical results for the stretch forming were presented as well as simple 3D sheet forming problem
Keck et al. [28]	1990	Axisymmetric	Elastic-plastic finite element calculations	Developed an advanced model of the contact conditions to improve the accuracy of FE results

Saran et al. [15]	1990	3D - Shell	Employed an elastic-plastic material description with Hill's anisotropic model	Predicted values of P , ϵ , and flange reduction were compared with the corresponding experiments
Wang et al. [29]	1991	Axisymmetric	A rigid-viscoplastic section analysis finite element program, for plane strain stretching with general tooling shape, was developed	FEM ϵ on both outer and inner specimen surfaces and draw-in displacements at various H , were compared with corresponding experiments
Sukhomlinov et al. [30]	1992	Axisymmetric	The rigid-viscoplastic finite element approach and an incremental procedure including a Lagrangian formulation were used	The non-linear effects due to the changes in sheet geometry and contact conditions during each incremental step were observed
Huang et al. [16-18]	1994	Axisymmetric	Applied incremental Lagrangian formulation of elasto-plastic FE code to handle the contact condition	Predicted LDR under various drawing conditions and investigated the influence of c , μ , and r_d in the process
Harpell et al. [31]	1998	3D - Shell	Utilized an explicit dynamic finite element code, LS-DYNA	The LDR was predicted based on principal ϵ and attainment of the peak P
Jain et al. [21]	1998	Axisymmetric	Utilized elasto-plastic material, Von Mises yield criterion, and the isotropic hardening option	Analyzed the sensitivity of various material and test parameters towards the maximum P and σ , ϵ in various regions of the cup

Menezes et al. [32]	2000	3D - Solid	An elasto-plastic model was applied with an implicit algorithm of Newton-Raphson type	The method yielded a mixed system where the unknowns of the problem are static and kinematics variables
Kim et al. [33]	2001	3D - Shell	Incremental deformation theory and elastic-plastic material modeling were utilized	The factors affecting the initiation and growth of wrinkles were conveniently considered by FEM
Liu et al. [34]	2002	3D - Shell	Elastic-plastic FE formulation based on a Kirchhoff triangle element model was used	Flange earrings of strong anisotropic sheet metals in deep drawing process were numerically analyzed

2.4.2 Element selection: axisymmetric versus 3D – shell models

From Table 2.4, it is noted that there are two common element types used in literature, namely the axisymmetric and 3D – shell models. Figure 2.9 shows the images of the corresponding FE model of these two element types.

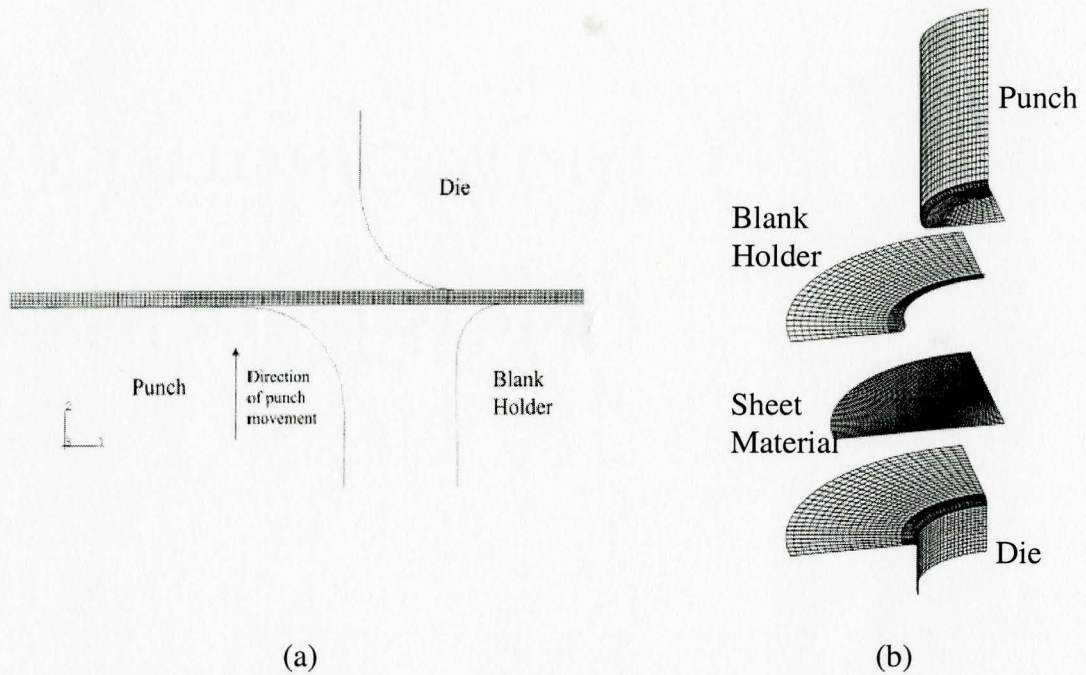


Figure 2.9 FE model of cup drawing process: (a) axisymmetric [21] and (b) 3D – shell model [31]

The advantages of axisymmetric model are that it takes less time to run this model due to a smaller number of elements, and additionally, the bending deformation at the punch nose can be analyzed accurately. The weakness is that the material is assumed to be isotropic in the model so that the anisotropy effect in different directions, which will result in earing phenomena after the cup is drawn or wrinkles in the flange during the process, cannot be properly simulated. On the other hand, the quarter shell element model in 3-D case does not have this problem, but it usually has a higher computational cost than axisymmetric model. Solid model was used in a very few cases, but it is not commonly applied in sheet metal forming research because the shell element model can well represent the process compared with the time consuming solid element model.

2.4.3 Finite element approaches: static implicit versus dynamic explicit methods

In this section, a brief review of the two common solution methods in FE analysis for metal forming problems are reported.

Assume a function $f(y, t)$ is continuous and differentiable in the domain Ω . Cauchy problem yields the following differential equation:

$$\frac{dy}{dt} = f(y, t) \text{ with } y(t_0) = y_0 \quad (2.9)$$

The solution of Equation (2.9) in the implicit scheme can be written as:

$$y_n = y_{n-1} + hf(y_n, t_n) \quad (2.10)$$

Explicit scheme, on the other hand, gives:

$$y_{n+1} = y_n + hf(y_n, t_n) \quad (2.11)$$

where h is the time step size and $n - 1, n, n + 1$ are the node numbers.

Implicit method attempts to satisfy the differential equation at time t_n after the solution at time t_{n-1} is determined [35]. Therefore, implicit method requires the solution of an algebraic system of equations at each time step. This is why implicit method is generally hard to implement for nonlinear problems. It is unconditionally stable for all stable model problems and conditionally stable for unstable model problems. On the other hand, explicit method uses the differential equation at time t_n to predict a solution at time t_{n+1} . It is conditionally stable for stable model problems and unconditionally unstable for unstable model problems.

Implicit method, which was the very first method implemented in FE method for simulation of metal forming process, is characterized by the formation of a stiffness matrix to represent the interaction of each node point, as shown below [35]:

$$[K(u)]\{u\} = \{F\} \quad (2.12)$$

where $K(u)$ is the stiffness matrix, u is the nodal displacement and F is the nodal force. In the solution process, the overall stiffness matrix is assembled by the stiffness of each element. This equation is nonlinear in the displacement and the static equilibrium has to be satisfied in the unknown final configuration, so it requires a full static solution of the stiffness matrix with convergence control [35]. The increment size is limited by contact conditions, so the computational time increases quadratically with increasing element number. In addition, the CPU cost is also very high, due to the calculation of matrix inversion and accurate integration scheme.

Explicit method can be expressed using a diagonal mass matrix system, as shown below [35]:

$$[M]u'' = \{F'\} - \{I'\} \quad (2.13)$$

where $[M]$ is the lumped mass matrix and $\{F'\}$ and $\{I'\}$ are external and internal forces matrices.

In explicit method, there is no need to check the force equilibrium, so convergence control is not required [35]. The computational cost of the explicit solution procedure is directly proportional to the size of the finite element model, which is less than the implicit method. As well, the CPU memory requirement is also lower than the implicit

method for large problems. This is why explicit method is more popular in simulating sheet metal forming operations, including the deep drawing process.

2.4.4 Effect of numerical parameters on FE results

In deep drawing simulations, there are some parameters or settings in pre-processing, which will directly affect the numerical results, and this is called sensitivity of finite element analysis. Duchene et al. [36] has recently carried out a sensitivity analysis of FE model of a deep drawing operation.

The deep drawing process simulation was presented for high strength steel, SPXI 250 with a strength factor K of 579.5 MPa and a strain-hardening exponent n of 0.17. The tooling geometries are shown in Figure 2.10.

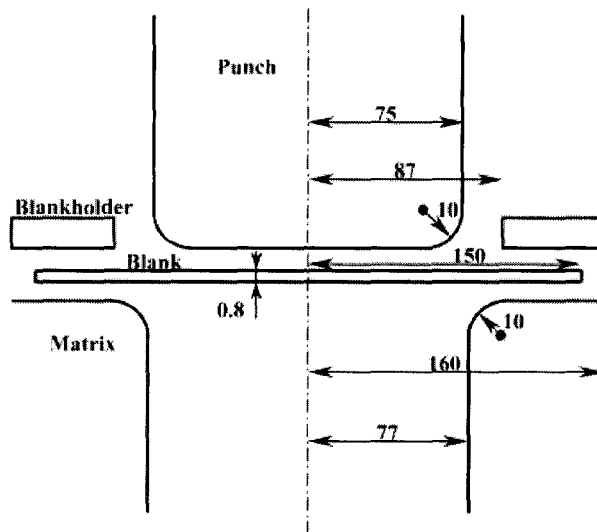


Figure 2.10 Geometry of the tools and blank (mm) [36]

In order to analyze the bending and unbending effect on the deep drawing process, the simulations were performed with one to three element layers through thickness of the sheet. Two lubricants, oil and nylon film were used in the analysis. A penalty factor representing the contact condition between the blank sheet and the die, whose effect on the final results was also taken into account. Another important factor was the type of finite element used, JET3D or BLZ3D. Both elements are 8-node solid elements with one integration point. The main differences between the JET3D and the BLZ3D elements are the hypothesis used for the strain field and the treatment of element locking. A comparison of FE results with experimental results for the above parameters was made through punch forces as a function of punch displacement and earing profile radii as a function of angles with respect to the rolling direction, as shown in Appendix C.

The conclusions drawn from this study are shown in Tables 2.5 and 2.6.

Table 2.5 Summary of the sensitivity study for the punch force [36]

Numerical parameter	Effect on the value of the maximum	Effect on initial slope	Effect on oscillations
Number of element layers	10% between 1 and 3 layers	No	No
Friction coefficient	Large effect	No	No
Penalty coefficient	Small effect	No	Yes
Finite element type	-	Yes	-

Table 2.6 Summary of the sensitivity study for earing profile prediction [36]

Numerical parameter	Effect of mean amplitude	Effect on shape
Number of element layers	0.87 mm between 1 and 3 layers	Yes
Friction coefficient	Large effect	Yes
Penalty coefficient	Small effect	Yes

The results from the above study indicate a clear need to select the numerical parameters, such as number of element layers, friction coefficient and penalty factor, with utmost care to ensure that these parameters do not adversely affect the quality of FE analysis.

2.4.5 Summary of finite element simulation based studies

Finite element analysis has already become a popular tool in metal forming analysis. If properly carried out, the amount of experiments can be reduced drastically, leading to increased efficiency in part and process design and consequent cost reduction. However, the numerical results are not always quantitatively accurate. They are often useful in the prediction of the trends with respect to various parameters.

2.5 Review of Redrawing Process

2.5.1 Overview

As mentioned in the Section 2.2, there is no suitable analytical redrawing model in the literature. However, some theoretical models have been developed with the

assistance of experiments and simulations. In this section, modeling and experimental redrawing studies are briefly reviewed.

2.5.2 MacPhee [37]

John MacPhee first proposed an engineering analysis of the redrawing process in 1976. Some relationships from this model and experiment are described here (refer to Figure 2.11 for nomenclature).

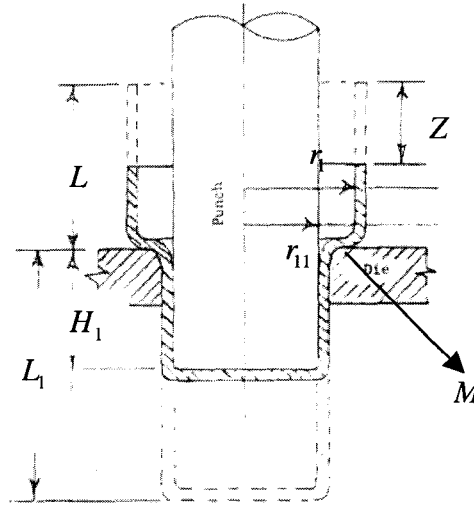


Figure 2.11 Relationships in redrawing process [37]

Using the relationship of geometry, the total strain at current radius r for punch displacement H_1 was calculated by the following equation:

$$\varepsilon_r(r, H_1) = \ln \sqrt{\frac{2r_{11}H_1}{r^2} + 1} \quad (2.14)$$

The radial or drawing stress at the juncture of flange and redrawn cup wall, point M in Figure 2.11, for punch displacement H_1 , $\sigma_1(H_1)$, was derived as:

$$\sigma_1(H_1) = - \int_{r_{\max}}^{r_1} \frac{\sigma_y(r, H_1)}{r} dr \quad (2.15)$$

where

$\sigma_y(r, H_1)$ = Yield stress at r for punch displacement H_1 , which is related to $\epsilon_T(r, H_1)$

$r_{\max} = r_1$ or $\sqrt{r_{11}^2 + 2r_{11}(L_1 - H_1)}$, whichever is less

By making the assumption of a constant yield stress in the flange for any punch travel, based on the experimental data, Equation (2.15) was approximated as:

$$\sigma_1(H_1) = \sigma_y(r_{11}, H_1) \ln\left(\frac{r_1}{r_{11}}\right) \quad (2.16)$$

where $\sigma_y(r_{11}, H_1)$ is the yield stress at the juncture of flange and redrawn cup wall, which is Point M in Figure 2.11.

The success of the redrawing process depends upon the total force required, which is made up of three components; the force necessary to deform the flange, the force due to hold-down pressure, and the force required to bend and unbend the work piece during redrawing. These forces were analyzed by MacPhee as follows.

(1) Drawing load P_1

The largest component of the total redrawing force, the force required to deform the flange, P_1 was expressed as:

$$P = K(\epsilon_{\max})^n \ln\left(\frac{1}{1 - \%RA}\right) \quad (2.17)$$

(2) Hold-Down Pressure Q

This component Q was estimated from experimental data and was approximated as:

$$Q = 0.33P_1 \quad (2.18)$$

(3) Bending Load F_B

The bending load, F_B was assumed by the author with the following value:

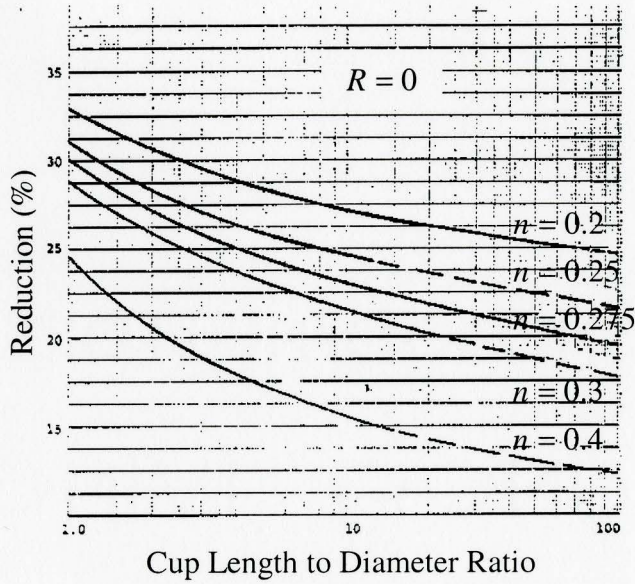
$$F_B = 0.1\sigma_{y\max} \quad (2.19)$$

where $\sigma_{y\max}$ is the maximum yield stress in the redrawn cup wall at top of the redrawn cup and it was represented as $\sigma_{y\max} = K(\epsilon_{\max})^n$.

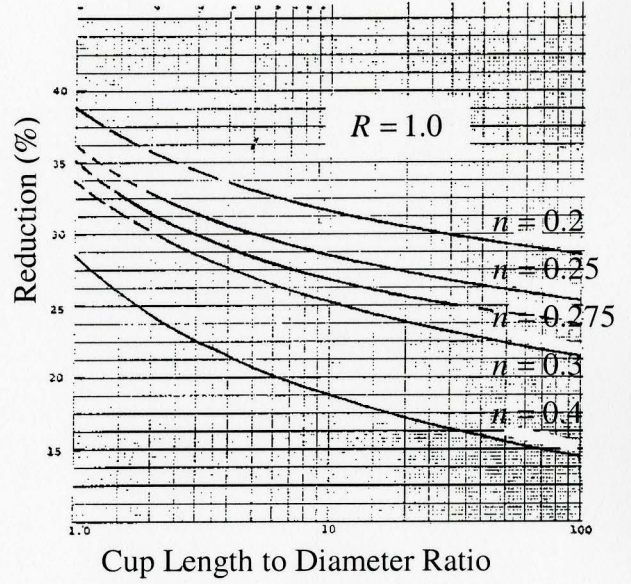
The total punch load F_{total} was expressed simply by taking the sum of the above components, as shown below:

$$F_{total} = P_1 + Q + F_B = K(\ln \sqrt{4LTD} + 1)^n \left[1.33 \ln \left(\frac{1}{1 - \%RA} \right) \right] \quad (2.20)$$

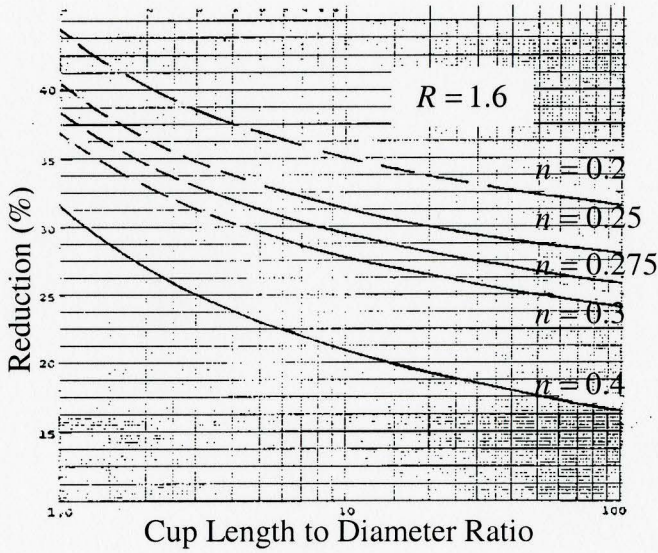
It was assumed that the limit in redrawing is reached when the punch load required to affect the redraw equals the maximum load that can be carried by the redrawn cup wall. Using the method presented above, the required punch force as a function of percent reduction, cup length to diameter ratio, and the rate of work hardening, was determined. Some relationships between maximum permissible reduction in redraw and redrawn cup length to diameter ratio with different anisotropy values are shown in Figure 2.12.



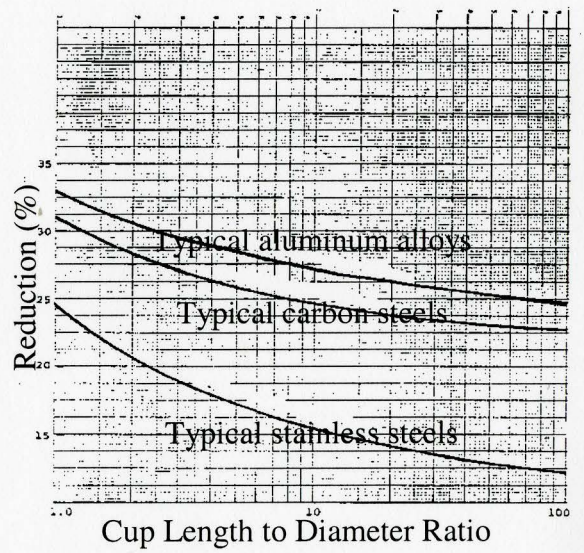
(a)



(b)



(c)



(d)

Figure 2.12 Maximum permissible reduction in redraw versus redrawn cup length to diameter ratio with (a) $\bar{R} = 0$, (b) $\bar{R} = 1$, (c) $\bar{R} = 1.6$ and (d) some typical metal type [37]

This work was the first model to analytically predict redrawing limit in the literature. However, some equations proposed were based on experimental data. The approach suffers from many rather arbitrary assumptions to simplify the analytical model. There was inadequate validation of the model results.

2.5.3 Iseki et al. [38-41]

In 1990, Iseki and coworkers proposed a detailed analytical model for determination of the redrawing ratio in the redrawing of cylindrical cups. Optimization theory was employed in the study and the limiting drawing ratio at different redraw stages was determined based on three different criteria: (1) the onset of plastic instability in the cup wall, (2) reduction in the maximum drawing force, from the standpoint of the life span of the tools and press, and (3) reduction in the drawing energy from a viewpoint of the power of the press. The method employed in all three criteria was simply the minimization or maximization of a chosen objective function. It was found that the predicted redrawing ratios were strongly dependent upon the objective function, which were (1) maximizing the minimum safety factor, (2) minimizing the maximum drawing force, and (3) minimizing the maximum drawing energy. The detailed derivation of this work is given in Appendix D and some results are shown in Figure 2.13 and 2.14 (referring to Appendix D for all the symbols in the figures).

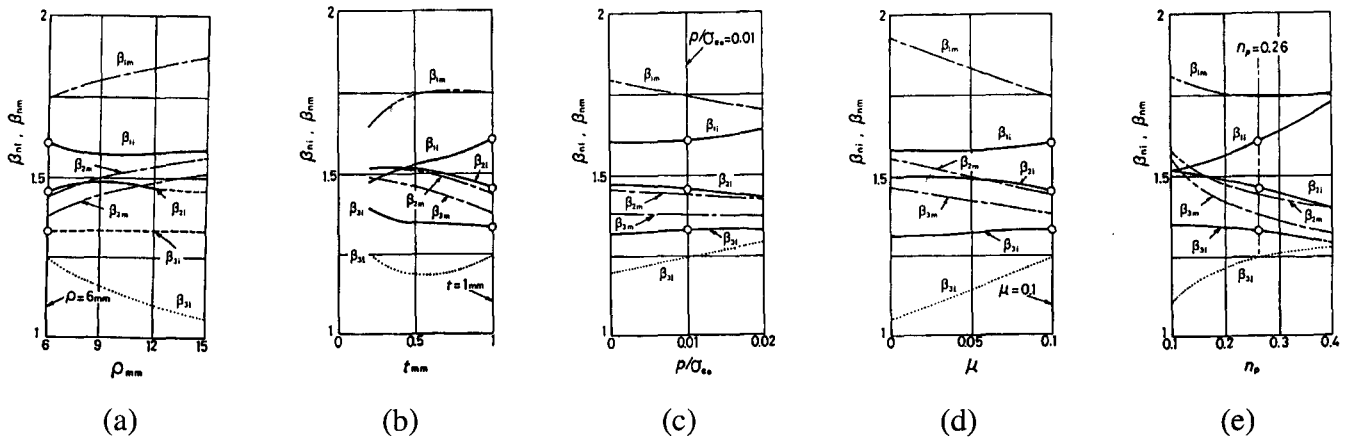


Figure 2.13 Relationship between β_{ni} of the minimum ψ_{max} method and (a) punch nose radius ρ , (b) blank thickness t , (c) mean pressure p / σ_{e0} , (d) coefficient of friction μ and (e) strain hardening exponent n_p [41]

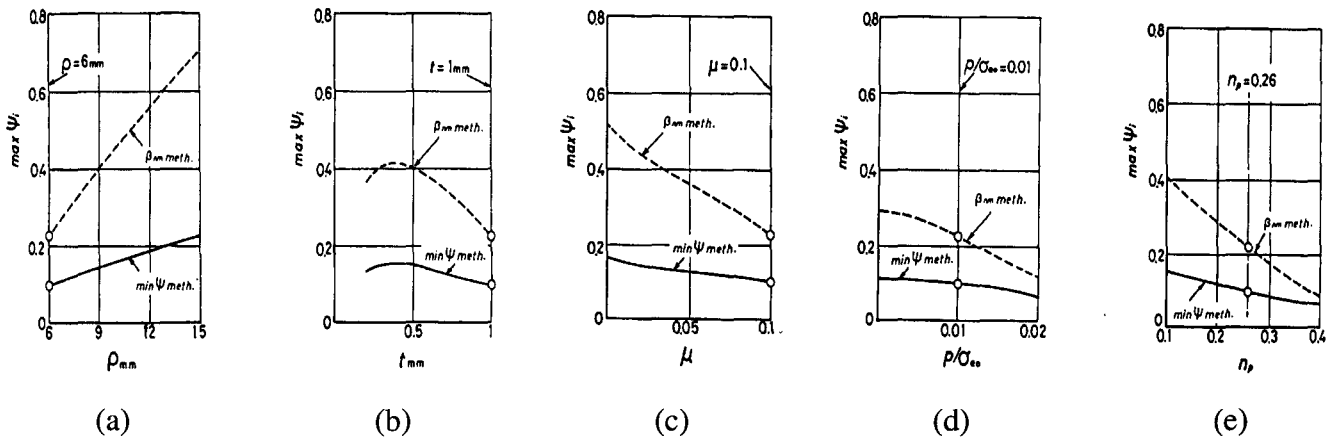


Figure 2.14 Relationship between maximum ψ_i and (a) punch nose radius ρ , (b) blank thickness t , (c) mean pressure p / σ_{e0} , (d) coefficient of friction μ and (e) strain hardening exponent n_p [41]

2.5.4 Parsa et al. [42]

Parsa et al. investigated the behavior of two-layer aluminum-stainless-steel (AL-SUS) laminated sheets during deep drawing, direct and reverse redrawing processes by FE simulations and laboratory experiments. However, the research was focused on the effect of thickness ratio of aluminum and stainless steel on the limiting drawing and

redrawing ratios, instead of the material properties, tooling geometries or friction conditions. The results showed that with a thickness ratio of 71.3% aluminum and 28.7% stainless steel, highest drawing ratio was achieved. In addition, in direct redrawing, contact of stainless steel with the punch leads to the maximum drawing ratio and in reverse redrawing, aluminum should contact the punch in order to achieve the highest drawing ratio.

2.5.5 Sonis et al. [43]

Recently, Sonis and coworkers have proposed an analytical redrawing model based on Leu's work on deep drawing. An equation of limiting redrawing ratio as function of material properties, tool geometries, and friction coefficient was derived using Hill's yield criterion. However, there are significant errors in their derived expressions, which would lead to wrong numerical results. For example, in Leu's work, the critical effective strain in deep drawing process was determined as an expression of $\bar{\epsilon} = \frac{1 + \bar{R}}{\sqrt{1 + 2R}} n$, which should not be the critical value if a redrawing operation is involved. In this work, this value was still set to be critical in a combined drawing and redrawing process. A modification of the Leu and Sonis et al. models in the form of a new redrawing model is proposed in Chapter 3.

2.5.6 Conclusion from redrawing studies

Although there are some redrawing studies reported in the literature, they are not comprehensive and accurate enough to understand this operation. For instance, only a few of redrawing force versus punch displacement curves or strain distributions of a redrawn cup were found in the literature, so it is necessary to develop more comprehensive understanding of this process through experimental and FE simulation studies.

2.6 Brief Review of Deep drawing with Centre Hole Blank Process

2.6.1 Introduction

The only difference between this process and regular deep drawing is that the initial circular blank has a centre hole, as shown in Figure 2.15. Depending on the initial hole size, the process usually results in three different consequences: (1) a full drawn cup with a centre hole at the bottom of the cup, (2) cracking at the centre hole edge, and (3) punch through the centre hole. The purpose to investigate this deep drawing process is to reduce the cost of fabrication process according to the product profile, because it is usually more economical to pierce a centre hole on the blank than trim it after the cup is drawn. Furthermore, there is limited information available based on this particular drawing process in the literature.

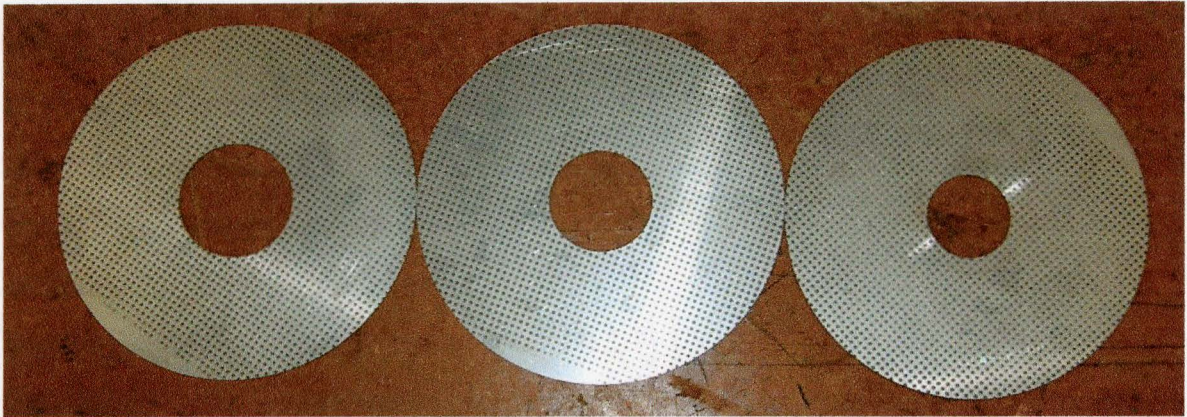


Figure 2.15 Centre hole blanks

2.6.2 V. Marinkovic [44]

Marinkovic [44] has recently carried out some analysis of hole-flange process both theoretically and experimentally. From Figure 2.16, it is to be noted that the research was focused on the third case mentioned above, which is the punch through case. If the ratio of the centre hole diameter to the initial blank diameter is too small, the elements around the centre hole area have to expand a large amount to let the punch travel through and the critical strain may be reached to cause the cracking failure. Marinkovic's research was based on this phenomenon, as shown in Figure 2.16.

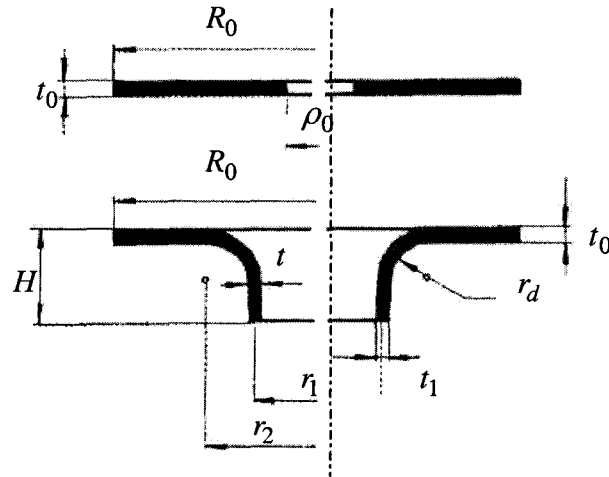


Figure 2.16 Geometric parameters of the centre hole blank and finished part [44]

In this study, the most important parameter is the flanging ratio k_p , which was expressed as the following equation:

$$k_p = \frac{r_1}{\rho_0} \quad (2.21)$$

The author followed the theoretical generalization made by A.J. Averkiev [45], which showed that the limiting deformation at forming can be brought into a functional correlation with a stress-based criterion (CP). This criterion can represent a specific deformation work at uniform plastic deformation. The CP criterion was determined by the following formula:

$$CP = \sqrt{\frac{3(1+\bar{R})}{2(2+\bar{R})}} \left[\sigma_y + \frac{(\sigma_b e^n - \sigma_y)^2}{\sigma_b e^n (n+1) - \sigma_y} \right] n \quad (2.22)$$

Based on a series of experimental work, Averkiev set up the following relations between $K_{p_{max}}$ and CP for various materials and thickness:

$$\frac{1}{k_{p\max}} = \begin{cases} 0.3796 + \frac{20.2304}{CP}, t_r = 3\% \\ 0.3477 + \frac{19.9620}{CP}, t_r = 4\% \\ 0.3090 + \frac{20.8150}{CP}, t_r = 5\% \\ 0.2948 + \frac{19.5235}{CP}, t_r = 10 - 30\% \end{cases} \quad (2.23)$$

Based on Equations (2.23), a regression equation to determine the maximum flanging ratio $k_{p\max}$ was obtained and is shown below (Equation 2.24):

$$k_{p\max} = 1.8671 + 0.0604t_r - 0.0007t_r^2 \quad (2.24)$$

where t_r is reduced thickness.

A plot of Equation (2.24) is shown in Figure 2.17 along with experimental data.

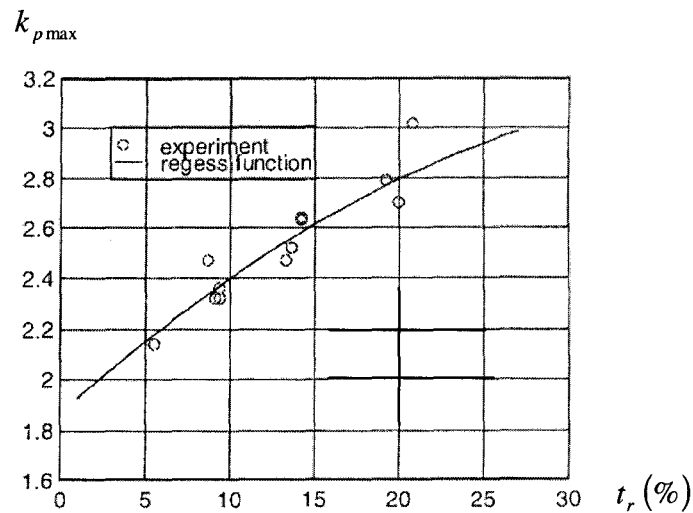


Figure 2.17 Dependence of the limiting flanging ratio on the reduced thickness [44]

The research was based on a combined theoretical-experimental method and regression was utilized to obtain the relationship between the limiting flanging ratio and

thickness reduction. The conclusion was that with larger thickness reduction, a higher limiting flanging ratio could be achieved in this deep drawing process.

2.6.3 Conclusion on deep drawing with centre hole blank process

From the brief review on this deep drawing process for a blank with a centre hole, a limited amount of resources were found in the literature. A few of theoretical and experimental work and FE simulation models were developed. However, a better understanding of this process will provide a useful contribution to automotive industry for certain applications, so it is necessary to carry out further investigation of this drawing operation in terms of experiments and FE simulations.

2.7 Chapter Summary

From a literature review of previous work, it was found that a large number of studies to investigate the deep drawing process have been carried out and a good understanding of the first draw process now exists in terms of analytical, experimental, and FE models. However, redrawing and deep drawing of blank with a central hole processes have been analyzed in a rather limited way. Both experiment and simulation work is at best partially studied and results are not consistent. There is a need for an improved analytical model and a more detailed experimental and FE simulation based studies of the redrawing and deep drawing of blank with a central hole.

Chapter 3 Proposed Analytical Model of Axisymmetric Redrawing Process

3.1 General Characteristics

In Chapter 2, Leu's theoretical model [1] to predict limiting drawing ratio for deep drawing was discussed in detail. The procedure of his derivation was to: (1) find the maximum stresses at cup wall and flange area, (2) develop the relationship between these two critical stresses in die profile region, and to (3) obtain the LDR by relating the two stress parameters. Hill's anisotropic criterion [8] was applied to determine the critical

effective strain, which was found to be $\bar{\epsilon} = \frac{1 + \bar{R}}{\sqrt{1 + 2R}} n$. Because Leu's model is further

developed for redrawing in this chapter. The reader is referred to Appendix A for detailed derivations of the mathematical expressions in his work. The general idea is that at LDR

of redrawing, the critical effective strain of the redrawn cup is $\bar{\epsilon} = \frac{1 + \bar{R}}{\sqrt{1 + 2R}} n$. Thus, the

maximum effective strain available for prior deep drawing process is only

$$\bar{\varepsilon} = \frac{1 + \bar{R}}{\sqrt{1 + 2\bar{R}}} n - \ln\left(\frac{r_1}{r_{11}}\right).$$

The second term on the right hand side of the above expression represents the effective strain produced by redrawing. The critical condition can also be expressed by $\ln(LDR_1)$, the natural logarithm of limiting drawing ratio of first redrawing process. With these concepts, the limiting drawing ratio for both the first draw and subsequent redraw stages can be obtained, using the same procedure as Leu's work and associated assumptions. All the assumptions made in this theoretical model are listed below for the sake of completeness:

- (1) The drawn cup is a perfectly hollow cylinder.
- (2) There is no thickness change in the flange region during deep drawing process.
- (3) There is no thickness change at the bottom of the cup region during both operations.
- (4) The thickness along the cup wall region is a constant value.
- (5) Figure 3.1 shows the power law fit for both deep drawing and redrawing processes and the two stage fit can be expressed as:

$$I: \sigma = K_1 \varepsilon^{n_1} \quad (0 < \varepsilon < \varepsilon_1)$$

$$II: \sigma = K_2 \varepsilon^{n_2} \quad (\varepsilon_1 < \varepsilon < \varepsilon_{II})$$

The analytical model is derived and validated with the assumption of $K_1 \approx K_2 \approx K$ and $n_1 \approx n_2 \approx n$ in Section 3.2.

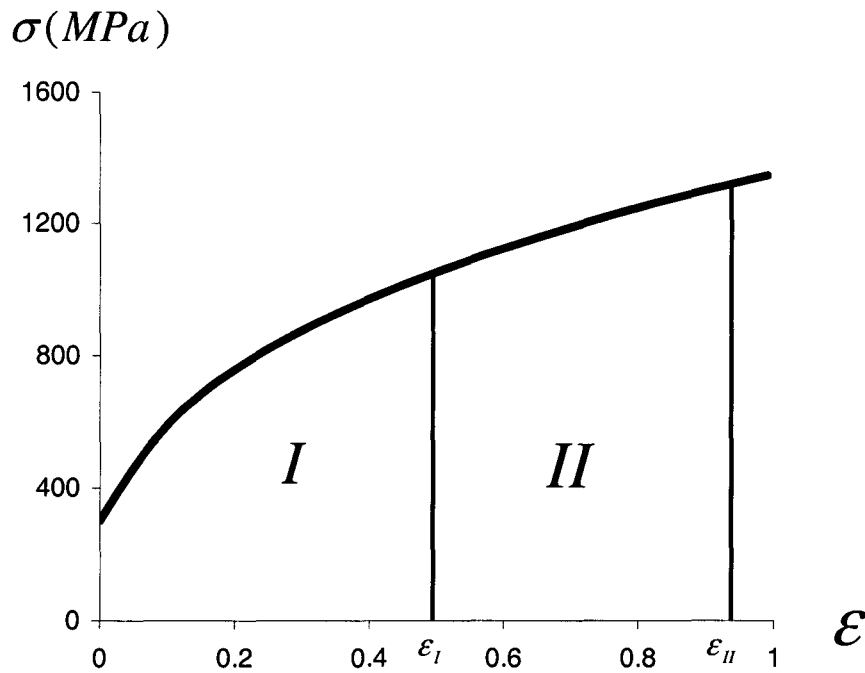


Figure 3.1 Power law fit for both deep drawing and redrawing stages

Another important issue in this theory is the blank design process behind the term ‘*LDR*’. It should follow the procedures shown below:

(1) As mentioned in Chapter 1, the product profile is usually designed first, which means that the second punch geometry is defined.

(2) From equation, $LDR_1 = \frac{r_1}{r_{11}}$, the limiting drawing ratio of redrawing, being the ratio

of the maximum value of the first punch radius to the second punch radius, the critical punch profile for deep drawing process can be determined.

(3) From equation, $LDR_0 = \frac{R_0}{r_1}$, the limiting drawing ratio of deep drawing, being the ratio of maximum value of initial blank radius to the first punch radius, the critical initial sheet blank size can be calculated.

Thus the objectives are to design the tooling for both stages based on the final product profile and to find the critical initial blank size to avoid failure during the process.

3.2 Model Development

3.2.1 Limiting drawing ratio of redrawing process, LDR_1

As mentioned in Chapter 2, the limiting drawing ratio for redrawing process is determined first. Figure 3.2 below shows this model in detail, including all of the parameters of interest at some instance of time.

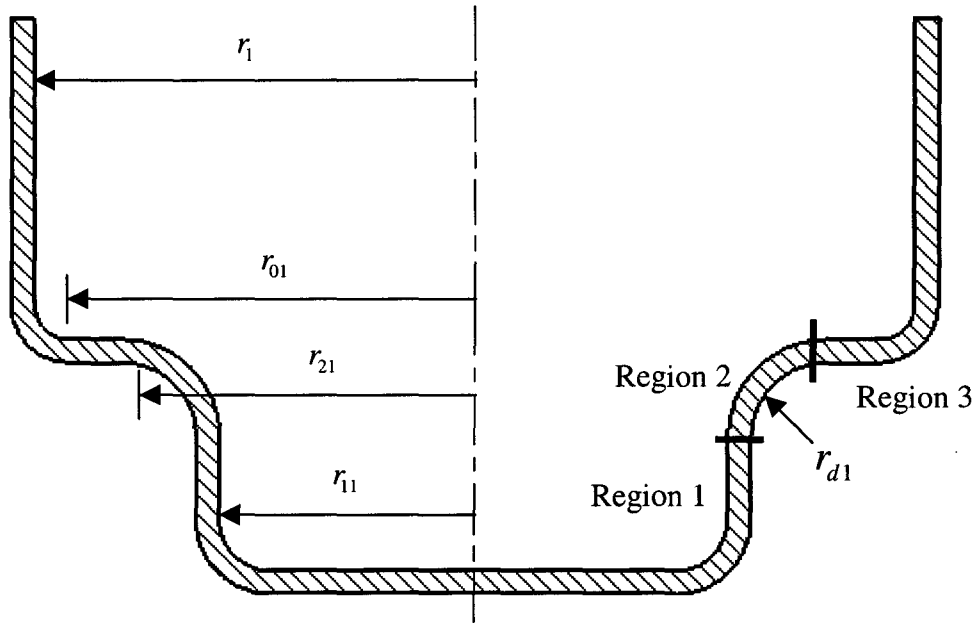


Figure 3.2 Detailed section view of half-drawn cup for redrawing process

(1) Region 1

Using the method proposed by Leu, the maximum drawing load for redrawing P_{c1}

in this region can be calculated based on the critical effective strain $\bar{\epsilon} = \frac{1 + \bar{R}}{\sqrt{1 + 2\bar{R}}} n$ as:

$$P_{c1} = 2\pi r_{11} t_0 \left(\frac{1 + \bar{R}}{\sqrt{1 + 2\bar{R}}} \right)^{1+n} (n^n e^{-n} K) \quad (3.1)$$

(2) Region 2

The critical drawing stress at the top part of Region 1, $\sigma_{r_{21}}$ can be obtained in this region using the force equilibrium and the increase in rope tension around a capstan with friction between radii r_{11} and $r_{21} = r_{11} + r_{d1}$ [46], as shown below:

$$\sigma_{r_{21}} = \left(\frac{1 + \bar{R}}{\sqrt{1 + 2\bar{R}}} \right)^{1+n} (n^n e^{-n} K) \frac{r_{11}}{r_{21}} e^{-\frac{\pi}{2}\mu} \quad (3.2)$$

(3) Region 3

During this redrawing process, the effective strain in this region can be expressed by the following equation:

$$\bar{\epsilon} = \ln\left(\frac{R_0}{r_1}\right) + \sqrt{\frac{2(1 + \bar{R})}{1 + 2\bar{R}}} \ln\left(\frac{R}{r}\right) \quad (3.3)$$

The term ' $\ln\left(\frac{R_0}{r_1}\right)$ ', above represents the effective strain caused by the first stage. In the above equation, R is the initial radius of an arbitrary annular ring in this region and r is the radius of the annular ring after the cup is drawn.

Utilizing Equation (3.3), Hollomon's power law gives:

$$\bar{\sigma} = K \left[\ln\left(\frac{R_0}{r_1}\right) + \sqrt{\frac{2(1 + \bar{R})}{1 + 2\bar{R}}} \ln\left(\frac{R}{r}\right) \right]^n \quad (3.4)$$

By rearranging Hill's anisotropic equations, which are Equation (2.4-2.6) in Chapter 2, the following expression can be obtained:

$$\sigma_r - \sigma_\theta = K \sqrt{\frac{2(1+\bar{R})}{1+2\bar{R}}} \left[\ln\left(\frac{R_0}{r_1}\right) + \sqrt{\frac{2(1+\bar{R})}{1+2\bar{R}}} \ln\left(\frac{R}{r}\right) \right]^n \quad (3.5)$$

The radial force equilibrium equation of an element in this region for constant thickness yields:

$$\frac{d\sigma_r}{dr} = -\frac{\sigma_r - \sigma_\theta}{r} \quad (3.6)$$

On substituting Equation (3.5) into Equation (3.6), the following equation for radial stress is obtained in the integral form:

$$\int_{\sigma_{r01}}^{\sigma_{r21}} d\sigma_r = -K \sqrt{\frac{2(1+\bar{R})}{1+2\bar{R}}} \int_{r_{01}}^{r_{21}} \left[\ln\left(\frac{R_0}{r_1}\right) + \sqrt{\frac{2(1+\bar{R})}{1+2\bar{R}}} \ln\left(\frac{R}{r}\right) \right]^n \frac{dr}{r} \quad (3.7)$$

Alternatively, Equation (3.7) can be written as:

$$\sigma_{r21} = \sigma_{r01} + K \sqrt{\frac{2(1+\bar{R})}{1+2\bar{R}}} \int_{r_{21}}^{r_{01}} \left[\ln\left(\frac{R_0}{r_1}\right) + \sqrt{\frac{2(1+\bar{R})}{1+2\bar{R}}} \ln\left(\frac{R}{r}\right) \right]^n \frac{dr}{r} \quad (3.8)$$

The stress σ_{r01} can be approximated as $2\mu(1.1\sigma_y)\frac{r_1}{r_{01}}$ [1]. By substituting Equation (3.2)

in Equation (3.8) and solving the integral, the limiting drawing ratio for redrawing is determined, as shown below:

$$\begin{aligned}
f(LDR_1) = & -C_1 \frac{r_{11}}{r_{11} + r_{d1}} + C_3 \frac{LDR_1 r_{11}}{\sqrt{\left(LDR_1 r_{11} \right)^2 - \left(\frac{R_{21}}{r_{21}} \right)^2 (r_{11} + r_{d1})^2 + (r_{11} + r_{d1})^2}} \\
& + C_4 \left[1 + \frac{n}{2} \sqrt{\frac{1+2\bar{R}}{2(1+\bar{R})}} \ln \left(\frac{R_0}{LDR_1 r_{11}} \right) \right] \ln \sqrt{\left(\frac{LDR_1 r_{11}}{r_{11} + r_{d1}} \right)^2 - \left(\frac{R_{21}}{r_{21}} \right)^2 + 1} \\
& - C_4 n \ln \left[\frac{LDR_1 r_{11}}{r_{11} + r_{d1}} + \sqrt{\left(\frac{LDR_1 r_{11}}{r_{11} + r_{d1}} \right)^2 - \left(\frac{R_{21}}{r_{21}} \right)^2 + 1} \right] + C_4 n \ln \left(\frac{R_{21}}{r_{21}} + 1 \right) \\
& - C_4 n \frac{1}{\frac{LDR_1 r_{11}}{\sqrt{\left(LDR_1 r_{11} \right)^2 - \left(\frac{R_{21}}{r_{21}} \right)^2 (r_{11} + r_{d1})^2 + (r_{11} + r_{d1})^2}} + 1}} + C_4 n \frac{1}{\frac{R_{21}}{r_{21}} + 1}} = 0
\end{aligned} \tag{3.9}$$

where:

$$C_1 = \left(\frac{1+\bar{R}}{\sqrt{1+2\bar{R}}} \right)^{1+n} (n^n e^{-n} K) e^{-\frac{\mu\pi}{2}}$$

$$C_3 = 2\mu(1.1\sigma_y)$$

$$C_4 = 2^n K \left(\sqrt{\frac{2(1+\bar{R})}{1+2\bar{R}}} \right)^{1+n}$$

The detailed calculation procedures to solve the integral in Equations (3.8) and (3.9) are

shown in Appendix E. In Equation (3.9) above, the term $\frac{R_{21}}{r_{21}}$ for Region 2 can be

evaluated from volume constancy during plastic deformation:

$$\pi(R_{21}^2 - R_{11}^2)t_0 = 2\pi \left(r_{21} - \frac{2r_{d1}}{\pi} \right) \frac{\pi r_{d1} t_0}{2}$$

giving:

$$\frac{R_{21}}{r_{21}} = \sqrt{\pi \left(\frac{r_{d1}}{r_{11} + r_{d1}} - \frac{2r_{d1}^2}{\pi(r_{11} + r_{d1})^2} \right) + \left(\frac{r_{11}}{r_{11} + r_{d1}} \right)^2 \left(\frac{R_{11}}{r_{11}} \right)^2} \quad (3.10)$$

Because the effective strain in Region 3 is equal to the critical effective strain at limiting drawing condition, one obtains:

$$\bar{\varepsilon} = \ln \left(\frac{R_0}{r_1} \right) + \sqrt{\frac{2(1+\bar{R})}{1+2\bar{R}}} \ln \left(\frac{R_{11}}{r_{11}} \right) = \frac{1+\bar{R}}{\sqrt{1+2\bar{R}}} n$$

or

$$\frac{R_{11}}{r_{11}} = e^{\sqrt{\frac{1+\bar{R}}{2}} n - \sqrt{\frac{1+2\bar{R}}{2(1+\bar{R})}} \ln \left(\frac{R_0}{r_1} \right)} \quad (3.11)$$

It is to be noted that only parameter r_{11} is present in all of the equations. The term r_1 is simply expressed by $r_1 = LDR_1 r_{11}$, in a manner similar to first draw as described in Chapter 2.

3.2.2 Limiting drawing ratio of deep drawing process, LDR_0

After the limit punch radius of first redrawing stage, r_1 , is determined, the evaluation of limiting drawing ratio for deep drawing amounts to the problem of finding the critical sheet blank radius of the first operation with the relationship $R_0 = LDR_0 r_1$.

All the procedures are exactly the same as Leu's work, (refer to Figure 2.1 for details)

except that the critical strain at limiting drawing condition is not $\bar{\varepsilon} = \frac{1+\bar{R}}{\sqrt{1+2\bar{R}}} n$ anymore

but lower, as discussed in Chapter 2, since some strain has to be left for the redrawing

process. Equations presented by Leu are reset here with a different limiting value for effective strain and the detailed derivations are shown in Appendix F.

3.2.3 The overall limiting drawing ratio, LDR

Once LDR_0 and LDR_1 are obtained, the overall limiting drawing ratio of the combination of deep drawing and one redrawing operation can be simply determined as:

$$LDR = LDR_0 \times LDR_1 \quad (3.12)$$

Since the equations shown above are too complicated to solve in close form, an iteration method, such as Newton-Raphson Method, is employed. A flow chart of the calculations is presented in Figure 3.3 and 3.4. The results of numerical solutions are presented in Chapter 5 and compared with simulation results.

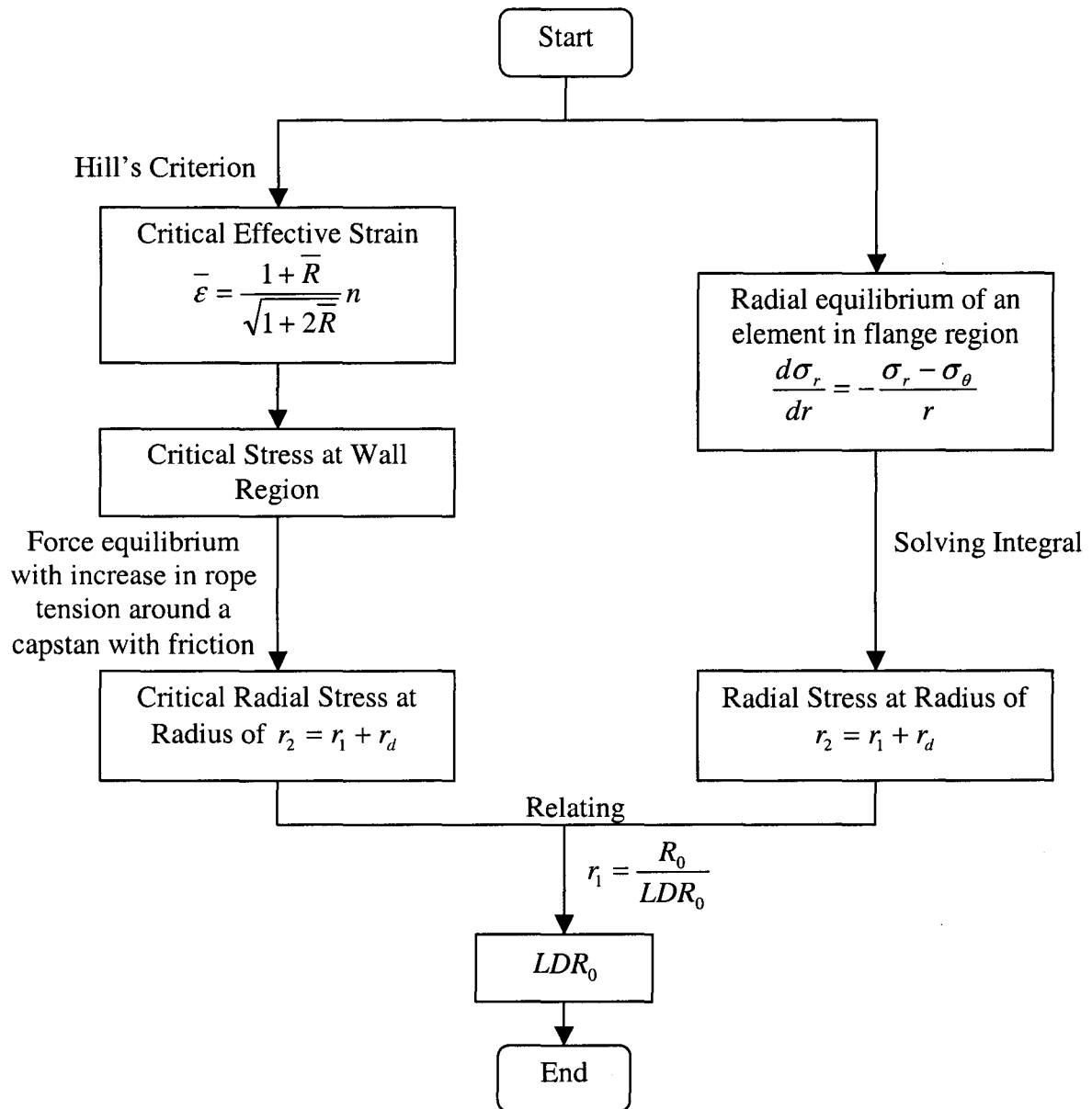


Figure 3.3 Logical flow chart for LDR determination in deep drawing

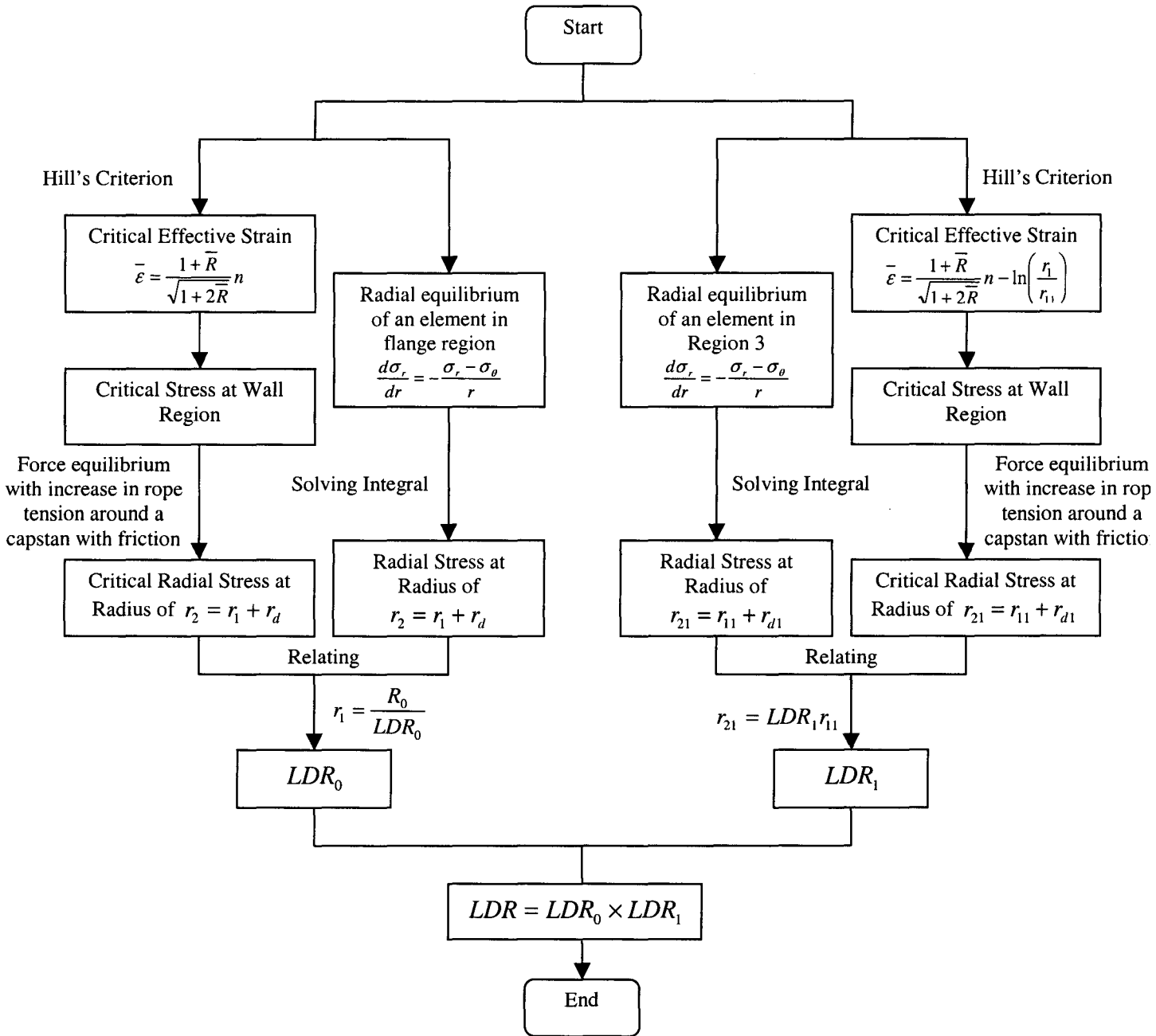


Figure 3.4 Logical flow chart for LDR determination in combined deep drawing and one redrawing operation.

Chapter 4 Experimental and FE Analysis Methodology

4.1 Introduction

To achieve the research objectives described in Chapter 1, experimental and simulation work was carried out. In this chapter, the experimental and FE analysis procedures are described in detail. Experimental aspects include the test equipment used, tooling design and test procedures. The FE modeling aspects include various modeling conditions such as part meshing, dynamic motion of the tooling and contact definition. In addition, problems encountered in both programs will be defined and the solution to those problems are also presented and discussed.

4.2 Experimental Program

4.2.1 Sheet material

The material of the blank sheet was a stainless steel 304 with a thickness of 0.5 mm. Three sets of dog-bone samples were cut along the sheet rolling (RD), 45° and transverse to rolling (TD) direction respectively from the same strip of blank sheet, as shown in Figure 4.1. The specimens were prepared as ASTM specification. Specimen dimensions are shown in Figure 4.2 and all units are in mm. Tensile tests were conducted on these specimens in a servo-hydraulic MTS test system with a speed of 1 mm/min. Tensile loads and axial displacements were continuously recorded during the test. This data was later converted into true stress versus true strain curves.

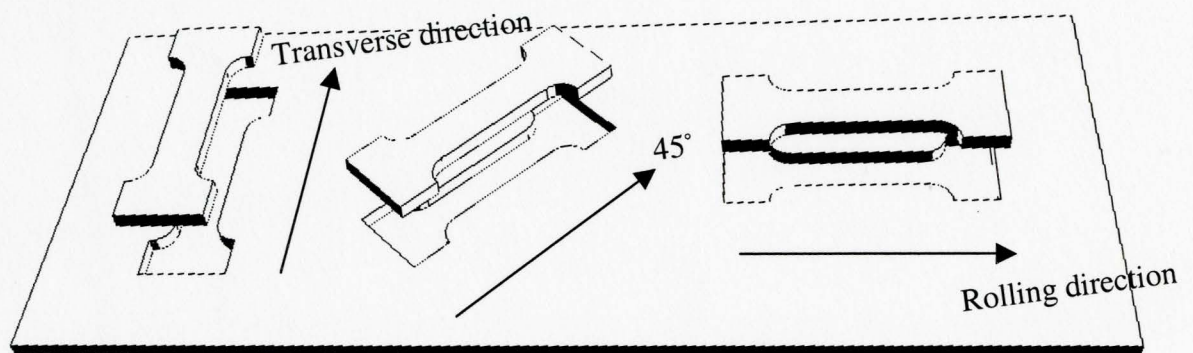


Figure 4.1 Demonstration of tensile test samples

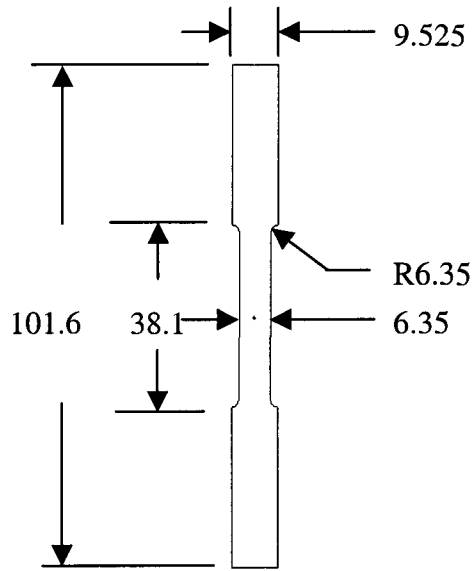


Figure 4.2 ASTM tensile test specimen dimension (mm)

A power law fit ($\bar{\sigma} = K\bar{\epsilon}^n$) to the data was carried out using non-linear least square curve fitting. Table 4.1 shows the detailed material properties of stainless steel 304 including the power law fit parameters.

Table 4.1 Material properties of stainless steel 304

	RD	45°	TD	Average
σ_y (MPa)	298.23	289.86	292.99	293.69
σ_{UTS} (MPa)	702.75	655.05	720.94	692.91
Elongation (%)	61.54	72.44	68.54	67.51
K (MPa)	1423.14	1238.67	1448.43	1370.08
n	0.373	0.358	0.367	0.366
R	0.981	1.279	1.134	1.168

As shown in Table 4.1, the material exhibits significant anisotropy as indicated by *R* values.

4.2.2 Equipment and apparatus

(1) Operating equipment

The deep drawing and redrawing tests were performed on a MTS mechanical testing machine fitted with two servo-controlled actuators, as shown in Figure 4.3. Two-actuator system allowed a close control of the clamping force during the drawing and redrawing processes. The capacity of the MTS test system was limited to 22,700 lbf force and a maximum stroke of ± 3 inch for both cylinders.

Cup drawing and redrawing test-rigs were designed, fabricated on a lathe, and assembled onto the above MTS machine with some common parts, to operate both drawing and redrawing processes. An A2 steel was utilized to fabricate the punches and dies for both processes because a high hardness was required by these components to avoid accidental scratches during the tests. The punches and dies were heat-treated in the hardness range from 55 to 58 HRC to increase their strength and scratch resistance.

Assembled tooling for deep drawing is shown in Figure 4.3. In the cup drawing process, the top half of the tooling stayed largely stationary at a certain initial height. A die insert, which performed the function of a die, was attached to the top tool housing. The bottom half of the tooling had a different insert that was utilized as a blank holder or punch guider. After the sheet material is placed on the bottom tooling, the top cylinder moves downwards until the top insert touches the material, and the blank sheet is then

clamped by both of the inserts. Subsequently, the bottom cylinder with the attached punch moves upwards to draw the blank. Some of the important tool dimensions are given in Table 4.2

Table 4.2 Tooling geometries of deep drawing

Punch Radius r_1 (mm)	Punch Profile Radius r_p (mm)	Punch Length (mm)	Die Radius r_{die} (mm)	Die Corner Radius r_d (mm)
28.35	9.525	120	28.9	6.35



(a)



(b)

Figure 4.3 Detailed assembly for deep drawing: (a) actual assembly and (b) computer generated model of the assembly

For the redrawing process, the former drawn cup was placed on the rig insert so that the centre axis of the cup could match the punch centre axis, as shown in Figure 4.4. A redrawing punch was then attached to the upper actuator and the drawing punch was removed from the lower actuator. The redrawing punch was then moved downward to

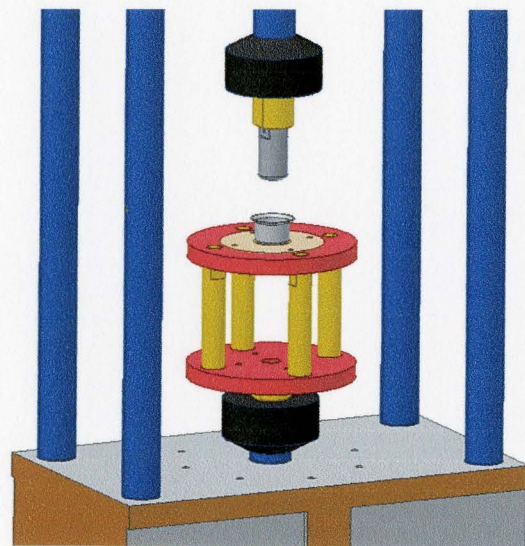
carry out the redrawing process. In retrospect, the cup drawing and redrawing tooling was easy to design and handle. Furthermore, good quality drawn and redrawn cups were obtained due to the alignment of the centre axis of punch and that of the cup drawn by the first stage. The redrawing tooling dimensions are shown in Table 4.3.

Table 4.3 Tooling geometries of redrawing

Punch Radius r_1 (mm)	Punch Profile Radius r_p (mm)	Punch Length (mm)	Die Radius r_{die} (mm)	Die Corner Radius r_d (mm)
24	6.35	80	24.65	6.35



(a)



(b)

Figure 4.4 Detailed assembly for redrawing (a) actual assembly and (b) computer generated model of assembly

(2) Strain measurement equipment

Argus Optical Strain Measurement System from GOM [47] was used to plot the strain distributions from different areas of the cup after the test. The system consists of a

CCD camera, a frame-grabber and a PC. Prior to the cup drawing process, all stainless steel blanks were electrochemically etched using Electrolyte LNC-3 solution using AC power with a magnitude of 20 A. The resulting grid pattern is shown in Figure 4.5. After the drawing operation, the system camera, as shown in Figure 4.6(a), was used to take several cup images from different angles to obtain the whole profile of the cup. Generally, the more black circular dots the system camera detected, the more accurate the strain measurement results were, so it was important to adjust the camera to the best position before imaging a region of the sample. These images were recorded and analyzed using dedicated software with the Argus System. The system computer can track the solid circular dot pattern to calculate and plot the different strain distributions in the cup. Overall, the accuracy of Argus system is exceptionally high and the absolute error is under $\pm 0.05\%$ [47].

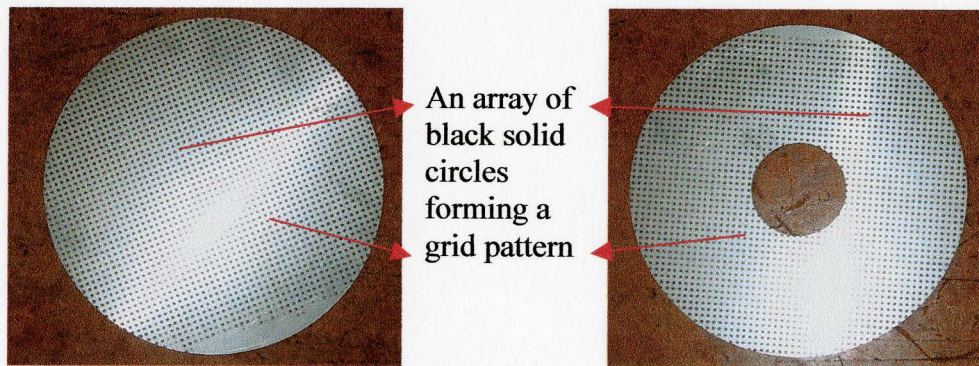


Figure 4.5 Grid pattern on the blank: (a) without and (b) with centre hole

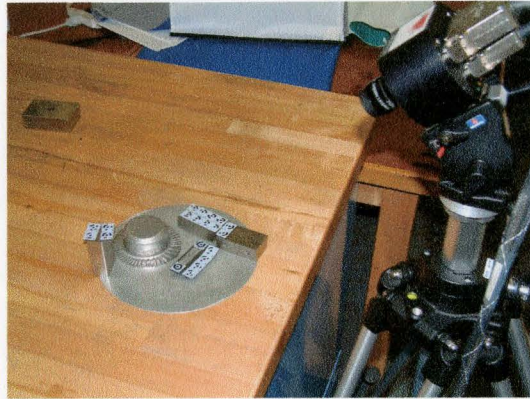


Figure 4.6 Argus system camera, formed cup with flange and calibration markers

4.2.3 Problems, limitations and attempted solutions

(1) Deep drawing process

In the earlier experimentation, wrinkling occurred in the cup flange area as well as wrinkle-free regions, as shown in Figure 4.7. This was because the sheet was clamped too tight on one side of the flange so that the material was unable flow into the die. However, on the other side, wrinkling happened, which means the clamping force was not adequate. This problem was caused the by unparallel contact surfaces of the blank and die, as shown in Figure 4.8. Because the design of this set of tooling is based on the limitation of MTS machine, the die and punch guide could not be perfectly be aligned to each other. However, after polishing the surface of the punch guide again and aligning both rigs at the beginning of each test, the cup quality could be significantly improved.

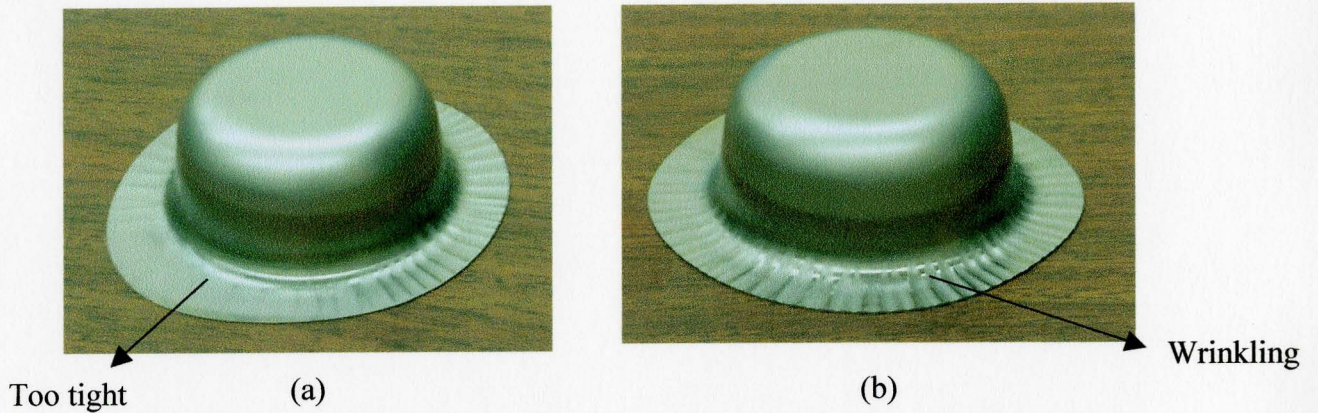


Figure 4.7 The drawn cup with problem at the flange area: (a) front view and (b) back View



Figure 4.8 The cause of unsymmetrical problem

Teflon® was utilized as a lubricant to reduce the friction force in the test. The method was to cover the Teflon® sheet onto the blank before the operation so that it would contact to the die surface instead of the blank surface, as shown in Figure 4.9. It was noticed that this application would decrease the clearance between the die and the cup wall during the test because of the thickness of the Teflon® sheet itself. However, due to the small amount around 0.01 mm for the Teflon® sheet, compared with the blank of 0.5 mm thickness, this influence could be neglected.

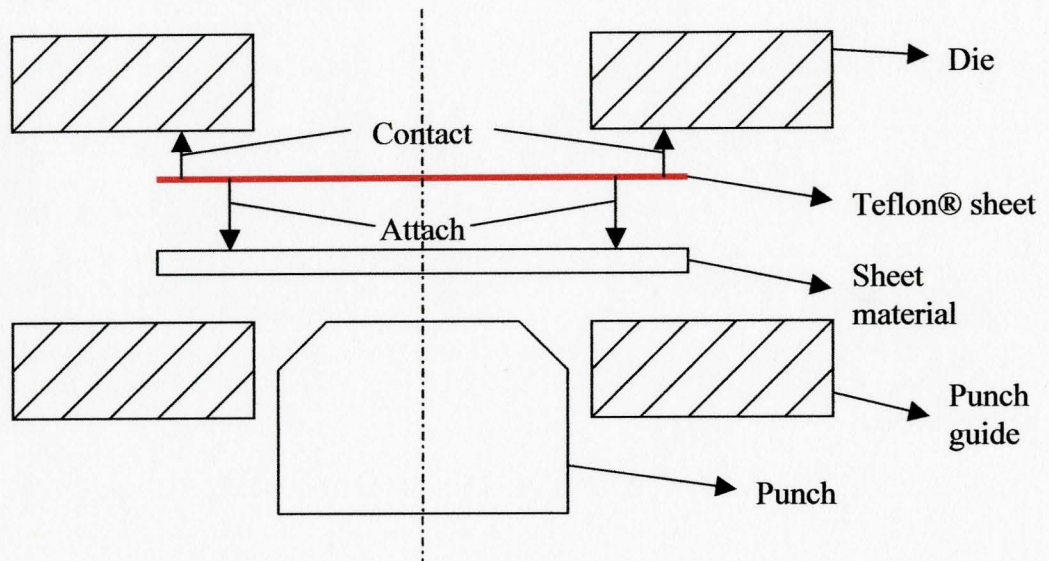


Figure 4.9 Application of Teflon® sheet as a lubricant

(2) Redrawing process

In the redrawing stage, the major problem was the post processing of the grid data after the test. For deep drawing, before the process, a very thin paper sheet was attached to the blank sheet so that the imprinted grids could be preserved during the contact and sliding when the material was drawn into the die. However, it was difficult to use the same method for redrawing, so after the process, almost all the grids were removed so that the Argus System was not able to measure the strains in the cup after the redrawing operation. A simple solution to this problem was to paint the dots on both surfaces of the blank sheets before the operations so that after the redrawing, the dots on the inside surface of the cup could be utilized for strain measurement. However, there were still some limitations to this method, because the redrawn cup had a relatively large depth so

that the system could not detect the grids easily due to the dark shadow inside the cup. Therefore, additional work was needed for a successful measurement of strains. An angle grinder was used to cut the one section of sidewall off from the cup to reduce the shadow effect, as shown in Figure 4.10. Although the process caused some heat and springback effects in Region 1 and 2 in Figure 4.10, the strains in Region 3 were representative due to the symmetric profile of the cup.

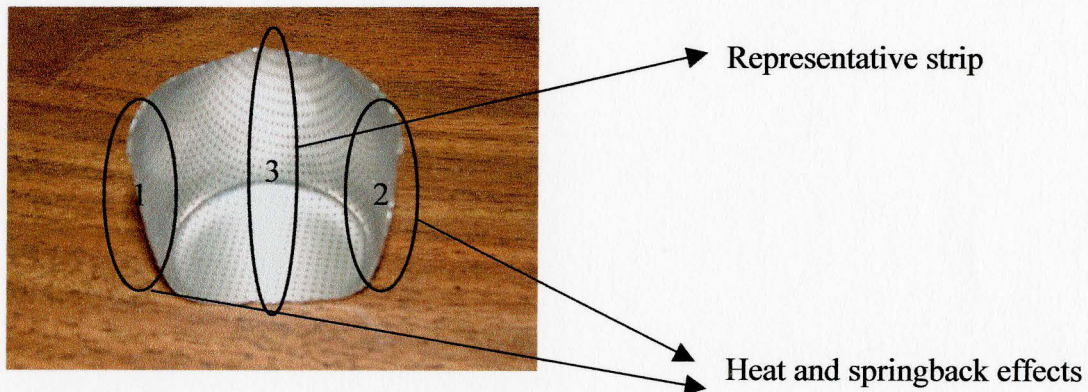


Figure 4.10 Redrawn cup after cutting

4.3 Simulation Program

4.3.1 Software

The finite element simulations were carried out by LS-DYNA3D - Version 970, a commonly used commercial general purpose nonlinear dynamic explicit FE code and particularly suitable for sheet metal forming operations. The dynamic explicit aspects of the FE analysis were discussed earlier in Chapter 2. Although the original DYNA3D was

developed by US national laboratory, the software has been significantly developed by Livermore Software Technology Corporation in the past two decades.

4.3.2 Finite element modeling

(1) Blank

The selection of FE mesh parameters, such as type and number of elements and element distribution, is important because it can directly affect the simulation result. Since the material and loading conditions are XY plane and YZ plane symmetric, as shown in Figure 4.11, a quarter model was enough to represent the blank and its deformation process. This way, anisotropy effect could also be investigated. Furthermore, the thickness of the blank is very small compared to its diameter, so shell elements were utilized. The traditional method to mesh this sheet surface is to mesh a line first and revolve the line elements around the normal direction, which is the Y-axis, by 90 degrees. However, this method results several triangular elements at the centre of the corner, as shown in Figure 4.12. Most of the finite element software prefers quadrangular elements to triangular elements, because a triangular element leads to a constant strain in the element area, which affects the accuracy of the calculation result. Thus, it was better to mesh the surface in a different way. In Figure 4.11, a quadrangular surface was made at the centre area of the blank, and by meshing this surface separately, the mesh distortion problem was avoided. The Angle BCD was set to be 150° instead of 90° , because it provided a smooth geometry transfer from this surface to the rest of the

blank. However, the traditional method mentioned above worked well to mesh the blank with a centre hole, as shown in Figure 4.13.

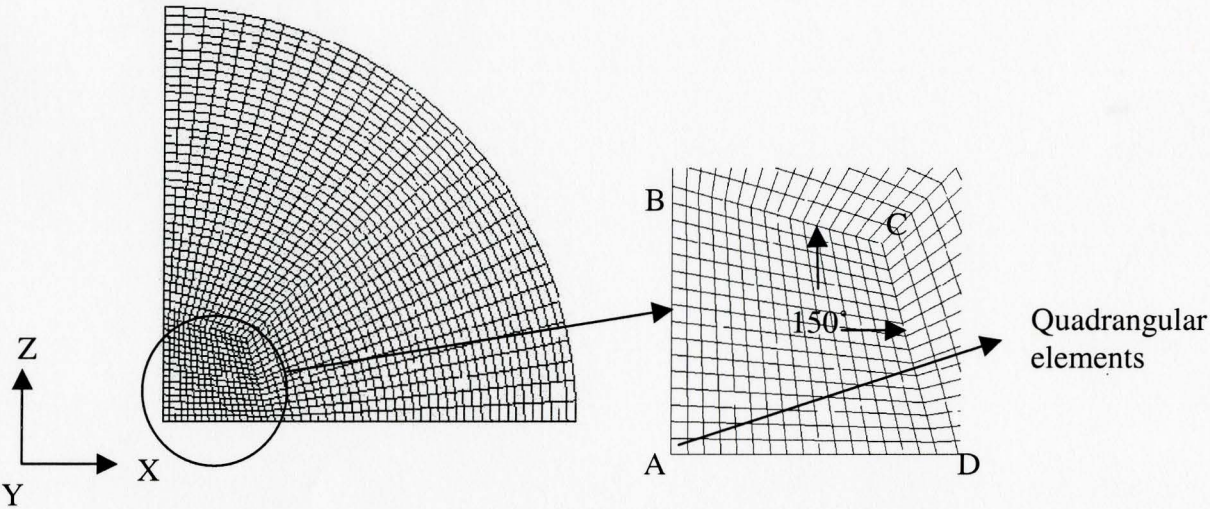


Figure 4.11 Quadrangular shell element mesh for sheet material

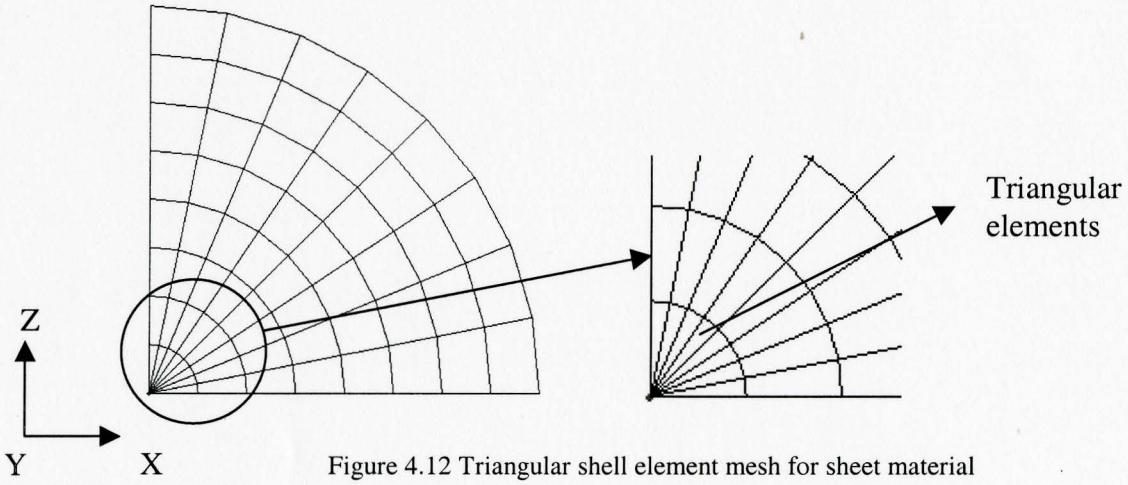


Figure 4.12 Triangular shell element mesh for sheet material

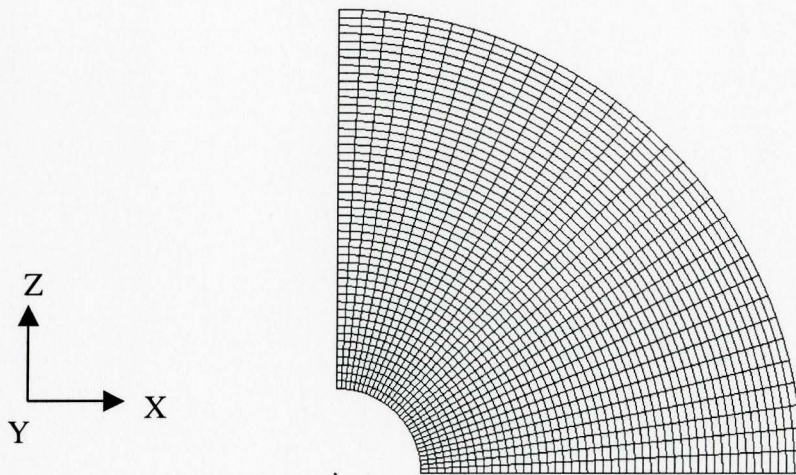


Figure 4.13 Shell element mesh for the blank with a centre hole

(2) Tooling

The tools for deep drawing process were modeled as five parts: punch, die, a punch guide or called blank holder, a rigid body, and 6 springs, as discussed below. The initial mesh for tooling is shown in Figure 4.14(a). Once again, due to the symmetry of the problem, only a quarter of the tooling was modeled to reduce the computational effort. The punch, die and punch guide were meshed as rigid body with shell elements. In FE analysis of metal forming process, the stresses and strains of rigid bodies are not the major interests of the research, and therefore they are not included in the calculation, resulting in a large saving in process time and CPU.

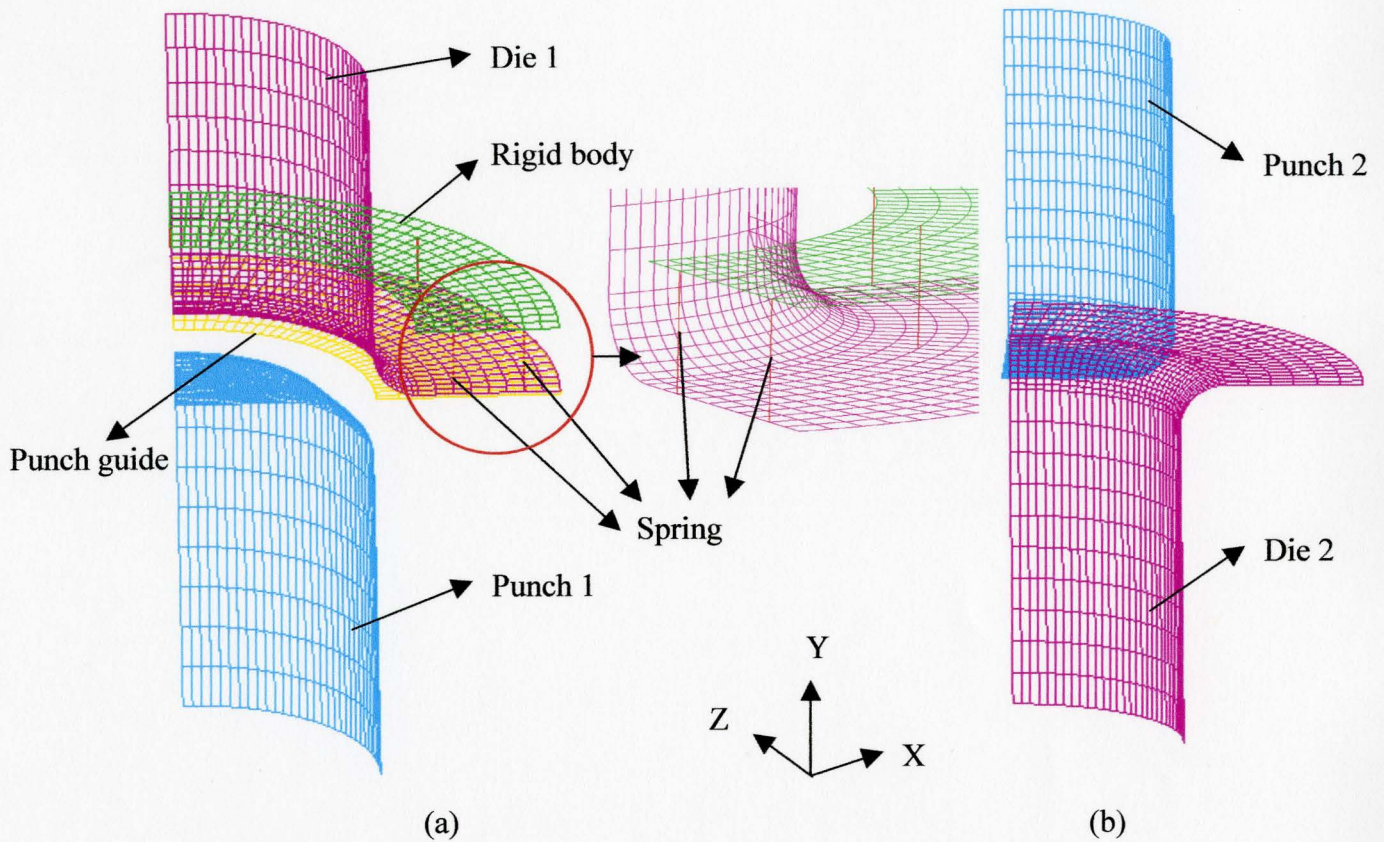


Figure 4.14 Finite element modeling of tooling for (a) deep drawing, and (b) redrawing

Another rigid body is included in the model and connected to the die by several springs. The reason of modeling this way is based on the behavior of MTS Machine in the experiments. In the experimental process, the clamping force is achieved by applying a downward displacement to the top hydraulic cylinder, so the magnitude of this force is controlled by the position of the top cylinder precisely. However, during the operation this position keeps changing because the contact between the drawn-in material and the die surface occurs and an additional load is needed to push the cylinder upwards so that the clamping force is increased. This is an important issue because the value of the clamping load will directly affect the punch force and lead to the effect on the strain

distributions of the final cup. In order to simulate this process properly, this clamping model based on a spring element was developed. Before exploring the model in detail, two traditional methods in literature to apply this force are briefly described.

- (a) The easiest way is to enable the die to just contacting to the top surface of the blank sheet and then apply a certain magnitude of force or pressure to this die to achieve the clamping function. This is not close to the real situation because the force is constant during the whole operation time, as shown in Figure 4.14, Curve 1.
- (b) The second method is to apply a displacement to the die until the target value of clamping load is obtained. However, in this case the die is set to be perfectly rigid, so it will absorb all the energies in the process and this will cause a huge increment of the clamping load, shown as Curve 2 in Figure 4.14. This is also not the correct situation.

In this model, two rigid bodies, one of which has the function of die, move downwards to a certain amount based on the real experimental data to achieve some particular clamping force at the beginning of the process and stay stationary. With an increase in the clamping force due to material drawn into the die, the die will be pushed upwards a small amount of displacement, which will be determined by the stiffness of the springs. In this case, the simulation work is very close to the reality and the set up of spring stiffness can be referred as the stiffness of this MTS test system (Figure 4.15, Curve 3). It is found that the clamping force gradually increases during the whole process, which can properly represent the experimental situation. The comparison of clamping force between this model and experiment is described in detail in Chapter 5.

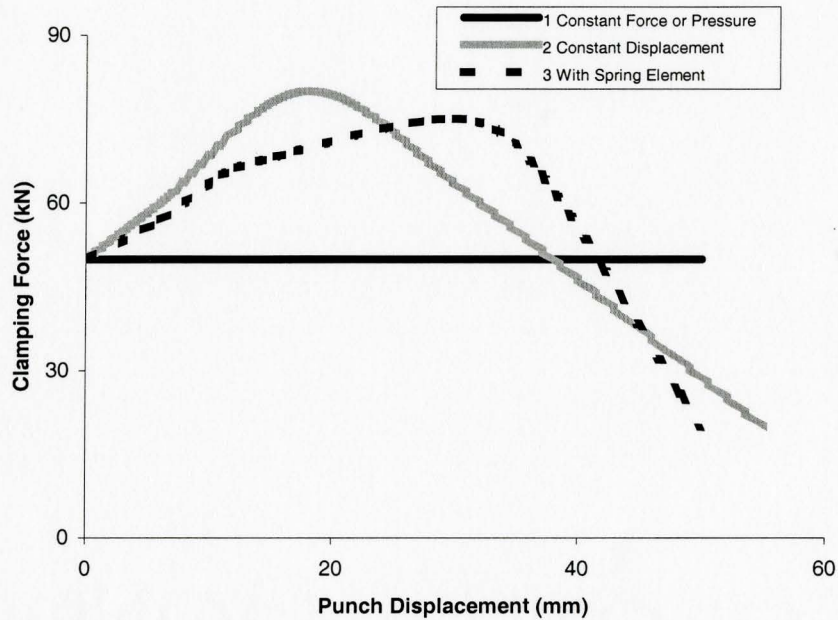


Figure 4.15 Demonstration of clamping forces with different simulating methods

In redrawing stage, the tooling consisted of only two components, which are the second punch and die, as shown in Figure 4.14(b). The drawn cup from the first simulation with all the stresses and strains information was utilized as the 'initial' state of the redrawing simulation.

4.3.3 Parameter control in pre-processing stage

The parameters input into the model follow the suggestions of Maker et al. [48], as described below:

(1) Materials

A material model named as 3_PARAMETER_BARLAT, which was developed for modeling sheets with anisotropic material under plane stress conditions, was selected to define the blank. 'Load Curve' HARDENING RULE option was chosen and twenty points were gathered and plotted from true stress-strain curve of the tensile test, to define the material hardening information. The anisotropies of three directions in terms of R - values were also input into the material model. For all the tooling, a rigid material model MAT_RIGID with the material properties of regular steel, including a density of $7.83 \times 10^3 \text{ kg/m}^3$ and a yield stress of 290 MPa , were utilized. However, it is to be noted that for the mathematical model, Hill's model with normal anisotropy value, material strength factor and strain hardening exponent was utilized. A comparison between these two material models in terms of drawn cup profiles, punch and clamping loads and thickness distribution was made and the results were in good general agreement. Therefore, it was decided to utilize this 3_PARAMETER_BARLAT material model in the simulation program.

(2) Shell element

'Fully integrated shell element' type in the shell element formulation definition using ELFORM parameter on the SECTION_SHELL keyword was selected, because it produces better accuracy and less convergence problems although this element type is more expensive in CPU cost. The number of thickness integration points NIP was set to 5 in this keyword as well, which was adequate for formability analysis. The CPU cost of the forming analysis increases linearly with the number of thickness integration points.

Another parameter set up in this keyword was the part thickness, t1-t4, which was defined as the real sheet thickness, 0.5 mm. The CONTROL_SHELL keyword was utilized to select two important parameters to define shell element. ITRIST flag was chosen to minimize the triangle elements, because as mentioned in the previous chapter, triangle element was not the suitable type in LS-DYNA. In order to allow the shell element thickness change during the whole process, the ISTUPD flag was also activated. Since a stiffness form of hourglass control is recommended for metal forming, the IHQ parameter was set to be either type 4 or 5, which is Flanagan-Belytschko type, in CONTROL_HOURLASS keyword.

(3) Contact

CONTACT_FORMING_SURFACE_TO_SURFACE contact type, especially developed for sheet metal forming process, was used to define all the three contact surface pairs, which were the sheet to the punch, sheet to the die and sheet to the punch guide. In these sets of contact pairs, the blank was always defined as slave surface and all the tools were set to be the master surfaces. For forming process, twenty percent of critical viscous damping, the VDC parameter, was used to eliminate high frequency dynamics as recommended [46]. Furthermore, the shooting node logic was disabled by using the SNLOG flag on this keyword. Penalty based contact interfaces were utilized and the penalty scale factor for all interfaces was set to be 0.010, by using SLSFAC on the CONTROL_CONTACT keyword. Another important parameter to be activated on this keyword was the thickness offset for the sheet using SHLTHK flag.

(4) Tooling motion

In explicit forming simulations, the running time can be greatly decreased using mass scaling or artificially high tool velocity. Both of these methods will introduce artificial dynamic effects, which must be minimized to some reasonable levels in an engineering sense. An independent parameter describing artificial dynamic effect is the number of explicit time steps taken every millimeter of the tool motion. In this simulation work, the second method was selected and the maximum tool velocity was set to be 2 mm/millisecond (ms). The time step size was set up by the DT2MS flag with a value of 0.00006 ms and this resulted in 500,000 steps for each 30 ms simulation. The velocity increased linearly in the first couple of seconds up to 2 mm/ms and stayed stable and then decreased to zero at the same deceleration in the last 2 ms of the whole process, as shown in Figure 4.16. The area of the profile geometry in the Figure 4.16 can represent the total magnitude of the punch displacement.

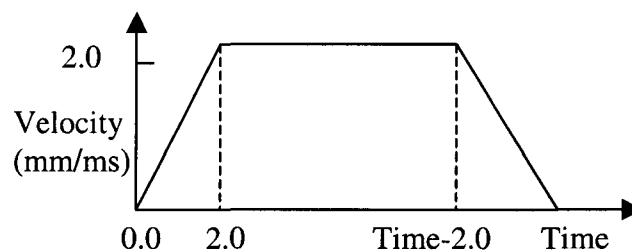


Figure 4.16 Punch velocity profile

(5) Output

In metal forming applications, a particular interest is the finite strain data, which was obtained by the keyword DATABASE_EXTENT_BINARY. As well, the reaction forces across interfaces due to prescribed motion, which are equivalent to punch and clamping forces, were achieved by activating the RCFORC and BNDOUT parameters on the DATABASE keyword. The output frequency of these two sets of data was adjusted by dt flag as 0.5 mm in these parameters.

(6) Multi-stage forming

Because this research involves redrawing operation, a multi-stage forming simulation was required. LS-DYNA can output a keyword-formatted file, named 'dynain', containing the deformed mesh and stress state at the end of the forming simulation. This file was requested by using the INTERFACE_SPRINGBACK_DYNA3D keyword. Then the input deck of redrawing simulation was created with all the information of the drawn cup from the previous simulation. For LS-DYNA to simulate multi-stage drawing processes, this feature is usually utilized to apply an explicit method for deep drawing with an implicit output analysis so that the calculation for redrawing can be developed.

4.3.4 Post-processing of FE simulation work

After each simulation, in post-processing stage, the deep drawn or redrawn cup height was determined by measuring the distance in Y direction between Node 1 and Node 2, Y_{12} in Figure 4.17. For deep drawing of blank with central hole, the cup height

was obtained by measuring the distance in Y direction between Node 1 or Node 2 and Node 3, Y_{12} or Y_{23} , as shown in Figure 4.18. The centre hole diameter $D_{centre\ hole}$ was determined by measuring the X or Z direction distance between Node 1 and Node 2, X_{12} or Z_{12} and multiplying a factor of 2. Furthermore, the remaining flange diameter was calculated by the equation below:

$$D_{remaining\ flange} = 2Z_{13} + D_{centre\ hole} \quad (4.1)$$

where Z_{13} is the distance between Node 1 and Node 3 in Z direction.

As mentioned in the previous chapter, the punch and clamping loads information was stored in 'RCFORC' file every certain period of time, which was set as 0.5 ms, by LS-DYNA and the curve was then transferred to load versus displacement curve to be compared with the experimental curve. It is to be noted that since a quarter model is applied in simulation work, the force magnitude obtained from simulation was only a quarter of the real case and, therefore, before plotting the curve, all the data values had to be multiplied by a factor of four.

After each simulation, the thickness contour along the whole cup was exported by LS-DYNA, referring to Figure 4.17 and 4.18, and with this function, the thickness distribution curve from simulation was obtained.

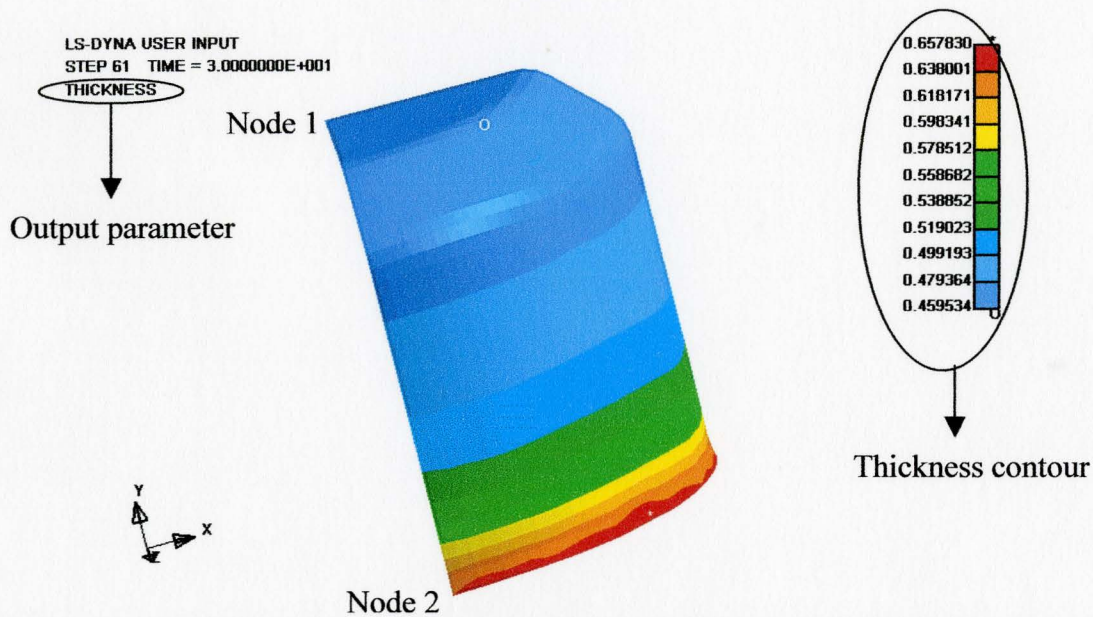


Figure 4.17 Demonstration of post-processing stage of FE simulation work for deep drawing or redrawing process

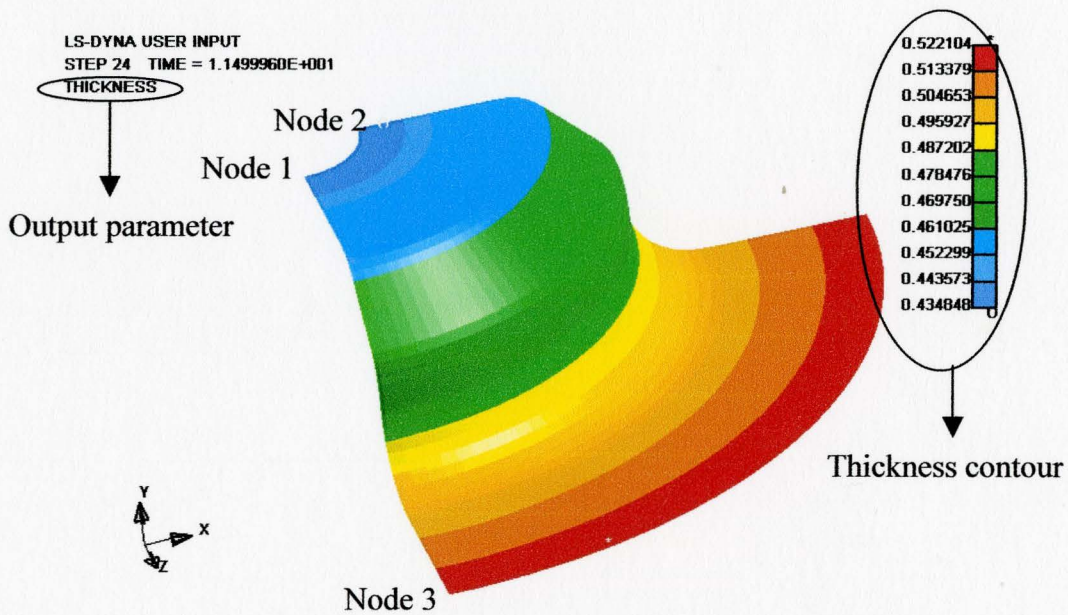


Figure 4.18 Demonstration of post-processing stage of FE simulation for deep drawing with centre hole blank process

From tensile test of the material, it was found that the critical effective strain for stainless steel 304 before failure is around 0.65 and this value was set to be the failure criterion of the simulation model. If the effective strain of any element became larger than 0.65 during the simulation process, the model was determined to fail, as shown in Figure 4.19.

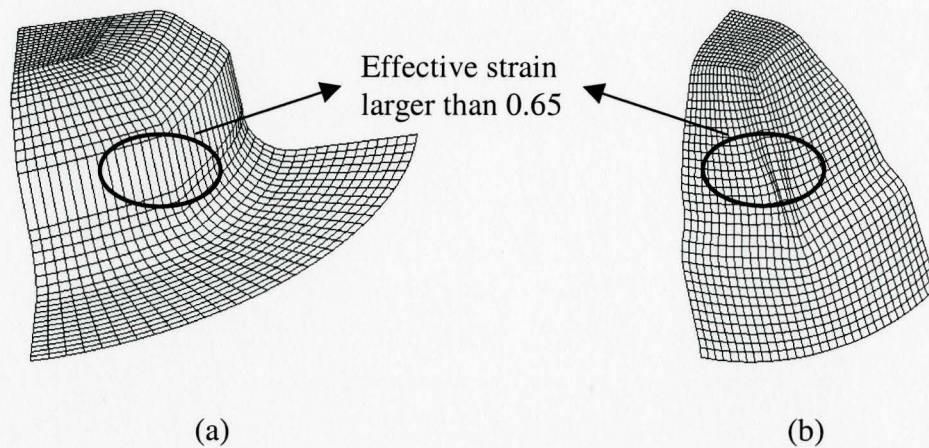


Figure 4.19 Failure criterion of FE simulation model: (a) cracking and (b) wall wrinkling

In the next chapter, results from analytical, experimental and FE simulation studies are presented and discussed.

Chapter 5 Results and Discussion

5.1 Introduction

In this chapter, the theoretical, experimental and simulation results of drawing, subsequent redrawing and deep drawing with centre hole blank processes are presented. The relationships between deep drawing and redrawing operations are compared. The process strain signatures and strain paths are studied to obtain a better understanding of material flow behavior in drawing process. In addition, an error analysis is presented by comparing the results from theoretical, experimental and simulation work. Some explanations of the cause of these errors will also be provided. Finally, the factors affecting the drawability of sheet material, such as tooling profiles, material properties and friction conditions, are discussed.

5.2 Experimental Results

5.2.1 Deep drawing process

Four sets of blanks with different diameters, 95 mm, 100 mm, 105 mm and 110 mm, were investigated in deep drawing experimental work. Figure 5.1 shows the drawn cups from these four blanks.

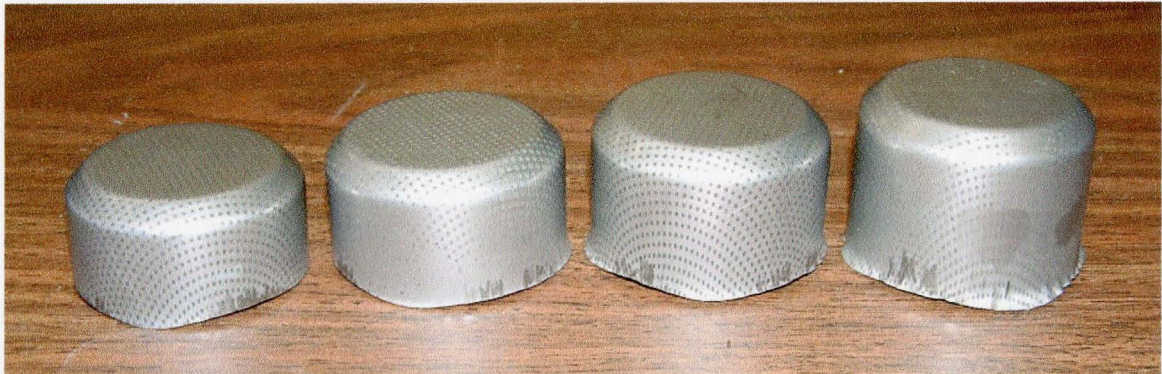


Figure 5.1 Deep Drawn cups from four blank sheets with different diameters: from left to right, 95 mm, 100 mm, 105 mm, 110 mm respectively

As expected, the cup drawn from the larger initial blank diameter had larger cup height. As discussed in the previous chapter, the cups were also drawn using Teflon sheet as a lubricating medium. All the cups drawn from the same initial blank size but with different friction conditions had the same heights (Table 5.1).

Table 5.1 Deep drawn cup depths from different sizes of blank sheets

Initial blank size (mm)	95	100	105	110
Deep drawn cup heights (mm)	29.59	33.84	38.43	43.41

Figure 5.2 shows a typical punch load and clamping force versus punch displacement curve. The punch load gradually increases to a maximum value, around 60% of the maximum cup depth. The punch force decreases at larger punch displacements due to a decreasing flange area, and consequently a reduced force requirement to draw the flange into the die cavity. The profile of the curve actually matches what has been described by Jain et al. [21] for aluminum. At the very last several millimeters of the punch displacements, the load raises a certain small amount. The cause of this phenomenon is that at this moment the cup has been fully drawn into the die and as explained in the former chapter, usually the top part of the cup wall is the thickest area, which can exceed the punch-die clearance, thus resulting in ironing of the top portion of the wall. The clamping force increases at a small rate until the end of the operation. The increasing of the clamping force is because of the contact between the drawn-in material and the die and this small increasing rate is due to the low stiffness of this MTS Machine.

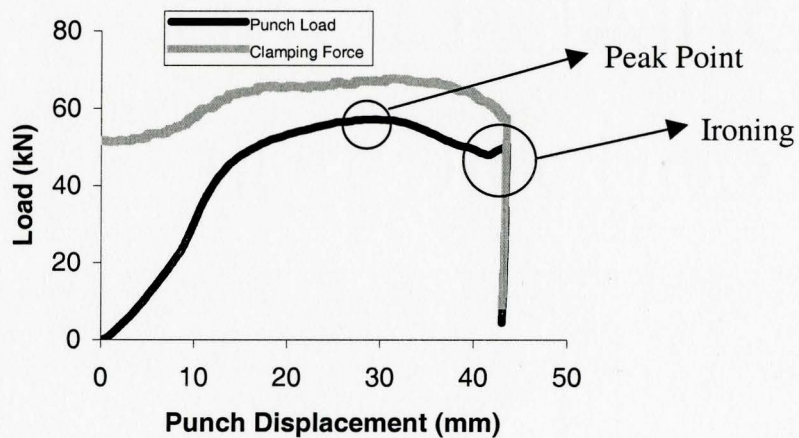


Figure 5.2 Punch load and clamping force versus punch displacement curve.

Another important but obvious issue is that the punch load curve from the largest initial blank diameter has the highest peak load and this means the critical drawing force of deep drawing process is proportional to the initial blank size, if no failure occurs (Figure 5.3(a) and (b)). Furthermore, as shown in Figure 5.3(c), the maximum drawing force with Teflon, which has lower friction coefficient, has a smaller magnitude than the dry friction condition. It means with decreasing of friction coefficient in the deep drawing operation, the maximum punch force also decreases so that the formability of the material is improved.

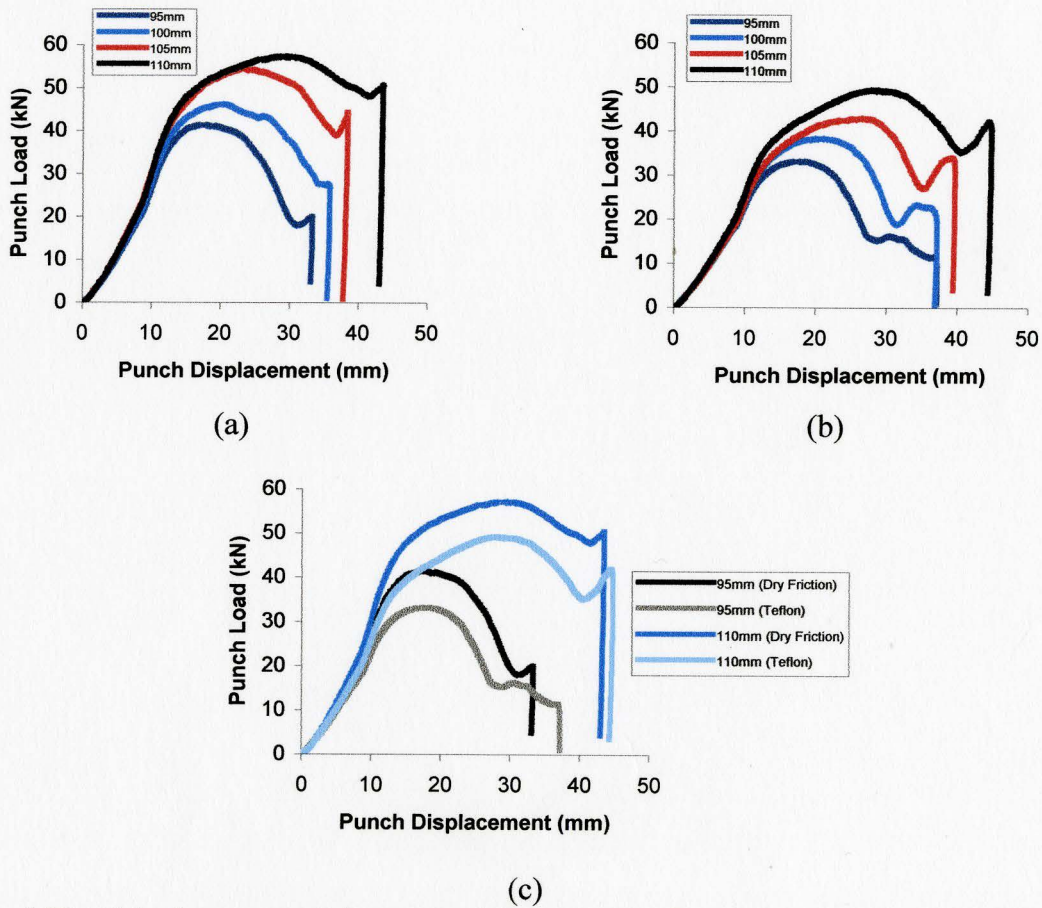


Figure 5.3 Punch load versus punch displacement: (a) dry Friction, (b) Teflon condition and (c) Comparison of these two friction conditions

A uniform strain distribution after sheet metal forming is a useful product performance and hence quality attribute. As mentioned in the previous chapter, Argus system can provide this strain distribution mapping function on the drawn cups. Figure 5.4 shows an example of the strain contours on the deep drawn cup with three output parameters: major, minor and Mises strains. At the bottom part of the cup the strain should be largely uniform. However, there are some noisy areas in the strain contour map as the drawn cup was often stuck to the die that necessitated tapping with hammer to eject the cup. However, these errors did not cause too much uncertainty in analysis, because the bottom part was not the focus of the research.

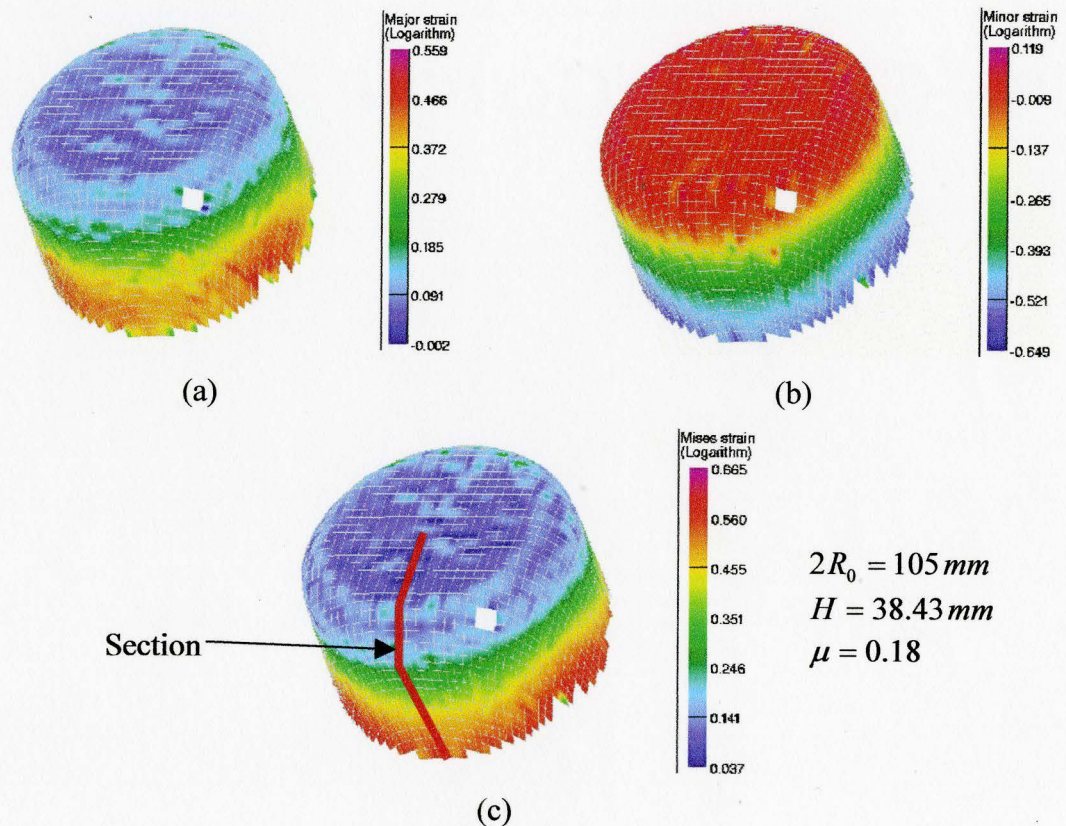


Figure 5.4 Strain distributions of a deep drawn cup with (a) major, (b) minor and (c) Mises strains output parameter

The final purpose of strain analysis is often to find the thickness distribution along the whole product. From the strain distributions in Figure 5.4, one conclusion is that the anisotropy effect of this material is not very obvious. Although stainless steel 304 is an anisotropic material from the tensile test, this effect is not severe compared with aluminum sheet materials. Therefore, as shown in Figure 5.4(c), a set of major and minor strains data of only one section along the cup profile starting from the bottom centre to the top of the cup wall, is plotted (Figure 5.5(a)). Then, the thickness along the cup is obtained from this information along with assumption of the constancy of volume, as stated below:

$$\varepsilon_1 + \varepsilon_2 + \varepsilon_3 = 0 \quad (5.1)$$

where ε_1 , ε_2 are the major and minor strains and ε_3 is the true strain in thickness direction. The thickness was calculated as follows:

$$\varepsilon_3 = \ln \frac{t}{t_0} \Rightarrow t = t_0 e^{\varepsilon_3} \quad (5.2)$$

where t_0 is the original sheet thickness of 0.5 mm.

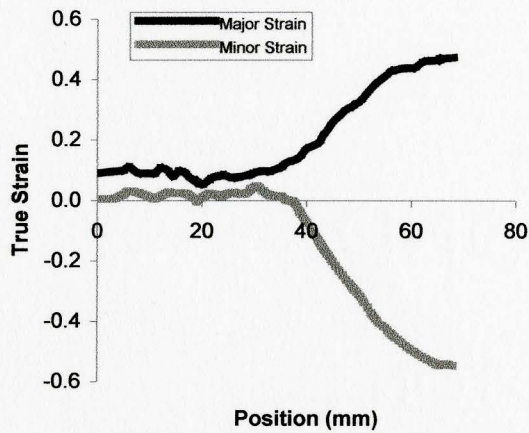
Figure 5.5(b) shows an example of the thickness distribution versus position plot.

Following observations can be made:

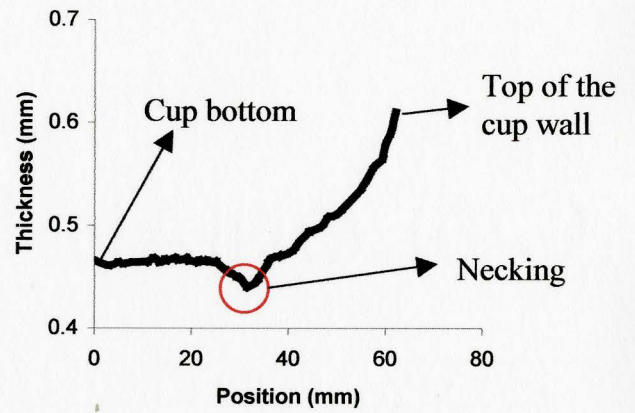
- (1) The thickness of the bottom area of the cup does not change too much, from originally 0.5 mm to 0.47 mm.
- (2) The thinnest part of the cup is the corner area, where the necking or cracking failures usually occur. This is because in this region, the material is under uniaxial tension condition.

- (3) In the wall area, the thickness gradually increases from the bottom to the top. The reason is because at top part of the cup wall, the material is actually under uniaxial compression condition.

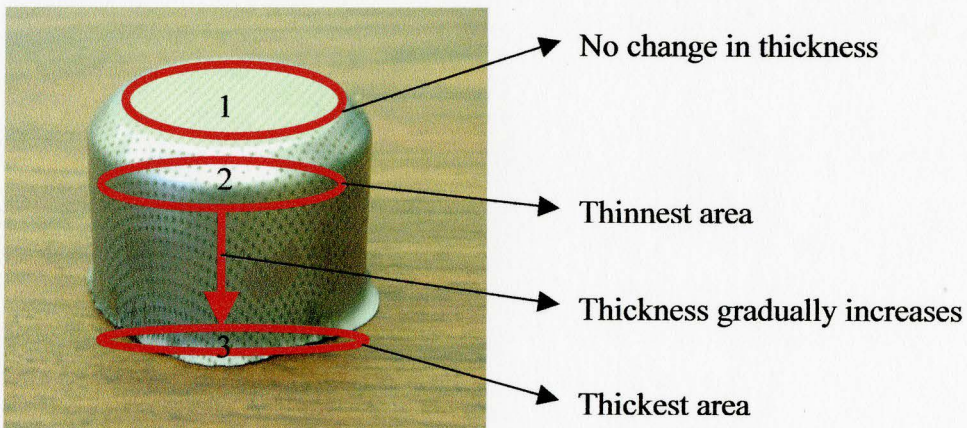
The results of thickness distribution are in agreement with the data reported in the literature.



(a)



(b)



(c)

Figure 5.5 (a) Major and minor Strain distributions, (b) an example of thickness distribution, and (c) demonstration of thickness distribution along a drawn cup

Using the same method, the thickness distributions of all the cups drawn from different initial blank diameters, were plotted, as shown in Figure 5.6 and some conclusions can be drawn: The thinnest areas in the all the drawn cups are always located at the punch profile radius position (Region 2 in Figure 5.5(c)). In Figure 5.6(a), which is the dry friction case, it is obvious that the thickness in Region 2 of the drawn cup decreases with an increase in the initial blank diameter. This is because of an increase in the drawing force so that necking phenomenon occurs earlier with an increase in blank size. However, in Figure 5.6(b), with Teflon friction condition, the thickness in the same area of all the cups drawn from different blank sheet diameters is very close to each other. This means that the necking either does not occur or occurs to a limited extent. In other words, lower friction can improve this failure mode to achieve a good drawn cup.

Figure 5.6(c) shows a re-plot of the data to compare the thickness distributions of the cups drawn from the same blank sheet size but with different friction conditions. The result agrees with the concepts discussed above: the cup drawn with lower friction has a larger thickness in Region 2, which is the cup corner area.

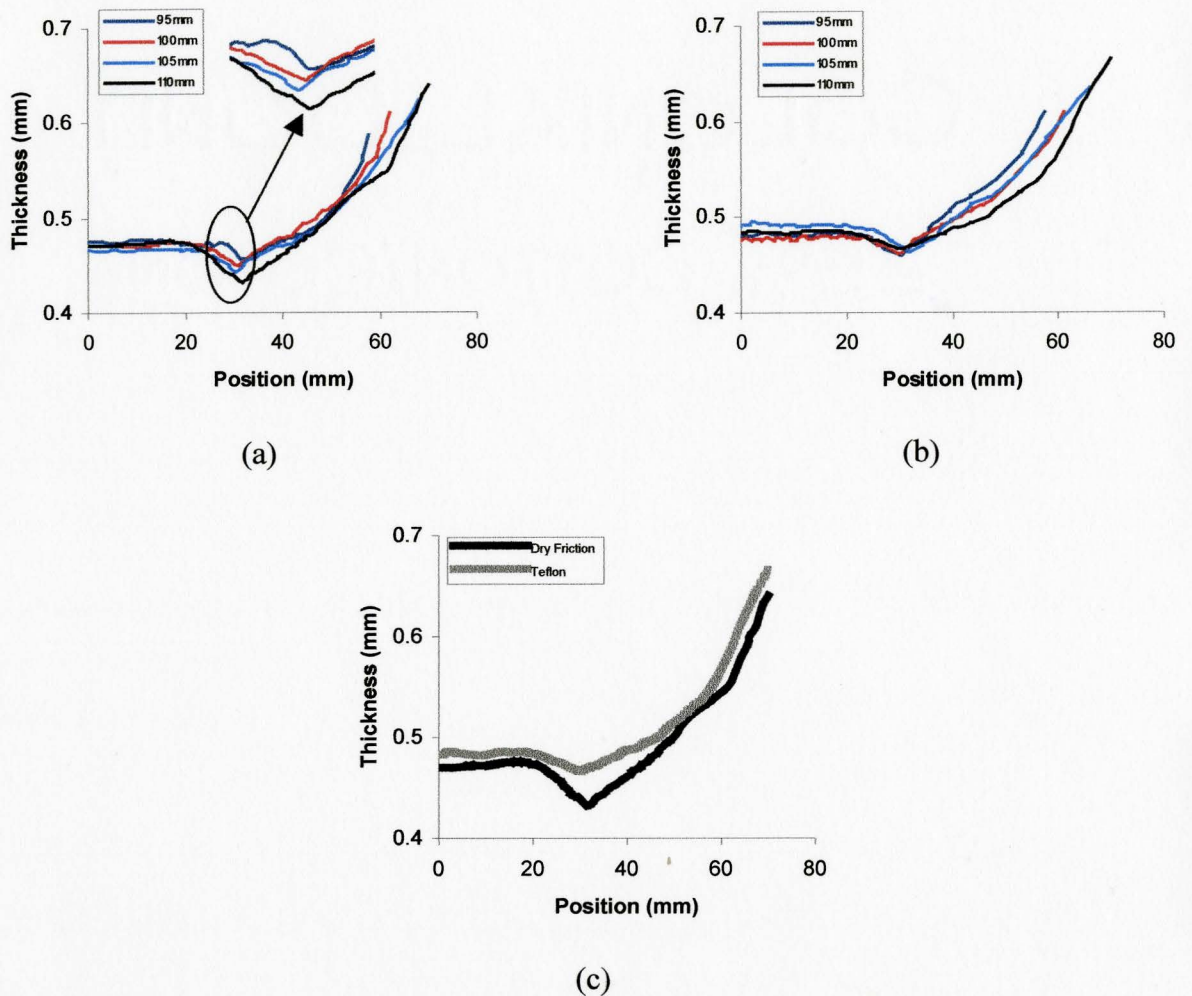


Figure 5.6 Thickness Distributions of the cups drawn from different initial blank sheet sizes with (a) dry friction, (b) Teflon condition and (c) comparison of the friction effects

5.2.2 Redrawing process

In the redrawing stage, only dry friction was applied (no lubrication between drawn cup and tools) due to the drawn cup profile, so only one set of redrawing experiments was conducted. The cups deep drawn from 95 mm, 100 mm, 105 mm and 110 mm diameters were redrawn to four new cups with smaller diameters but larger cup heights as shown in Figure 5.7 and Table 5.2.

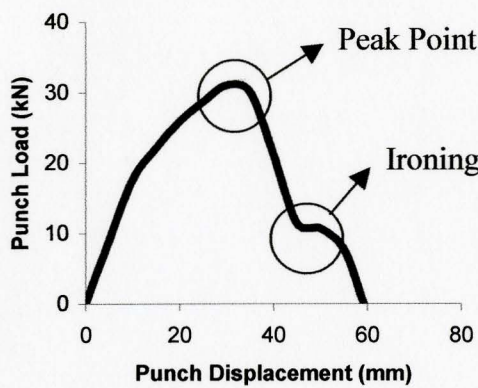


Figure 5.7 Redrawn cups from four deep drawn cups with different initial diameters: from left to right, 95 mm, 100 mm, 105 mm, 110 mm respectively

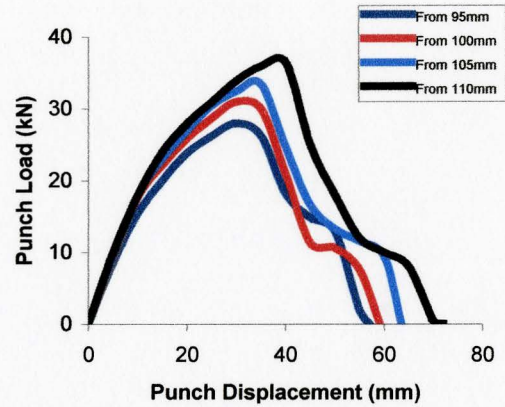
Table 5.2 Redrawn cup depths from different sizes of blank sheets

Initial blank size (mm)	95	100	105	110
Redrawn cup heights (mm)	35.13	40.11	45.42	51.46

Figure 5.8(a) shows an example of redrawing load versus punch displacement curve. The overall profile is very similar to the one of deep drawing. The punch force reaches its critical value at around 50-60% of the maximum cup height. The same ironing phenomenon reported for the first draw occurs in the last few millimeters of the punch displacement. Figure 5.8(b) shows a plot of four punch force versus punch displacement curves of the redrawn cup from different initial blank size. Similar to the case of the first draw, the redrawing force is proportional to the original blank diameter. In other words, redrawing load is proportional to the former drawn cup height, because the larger initial blank size leads to a deeper cup.



(a)



(b)

Figure 5.8 (a) Example of redrawing force versus punch displacement curve and (b) comparison of punch loads with different former drawn cup depths

Major, minor and Mises strain distributions along the redrawn cup, as measured using the Argus system, are shown in Figure 5.9. Also, thickness distributions of the redrawn cups are shown in Figure 5.10(a, b). The following observations can be made from the two sets of the figures:

- (1) Localized thinning or necking in the punch profile region is still present, but the problem is not very severe.
- (2) The profiles of these thickness curves in Figure 5.10(b) are very similar at the bottom of the drawn cup (Region 1 and Region 2 areas in Figure 5.5(c)), but start to disperse as one moves up to the cup wall (Region 3). Redrawn cup with larger initial height has a greater thickness value.

Redrawing experiments suggests that all redrawn cups have similar profile except the cup height. A deeper redrawn cup can be treated as an extension of the shorter one.

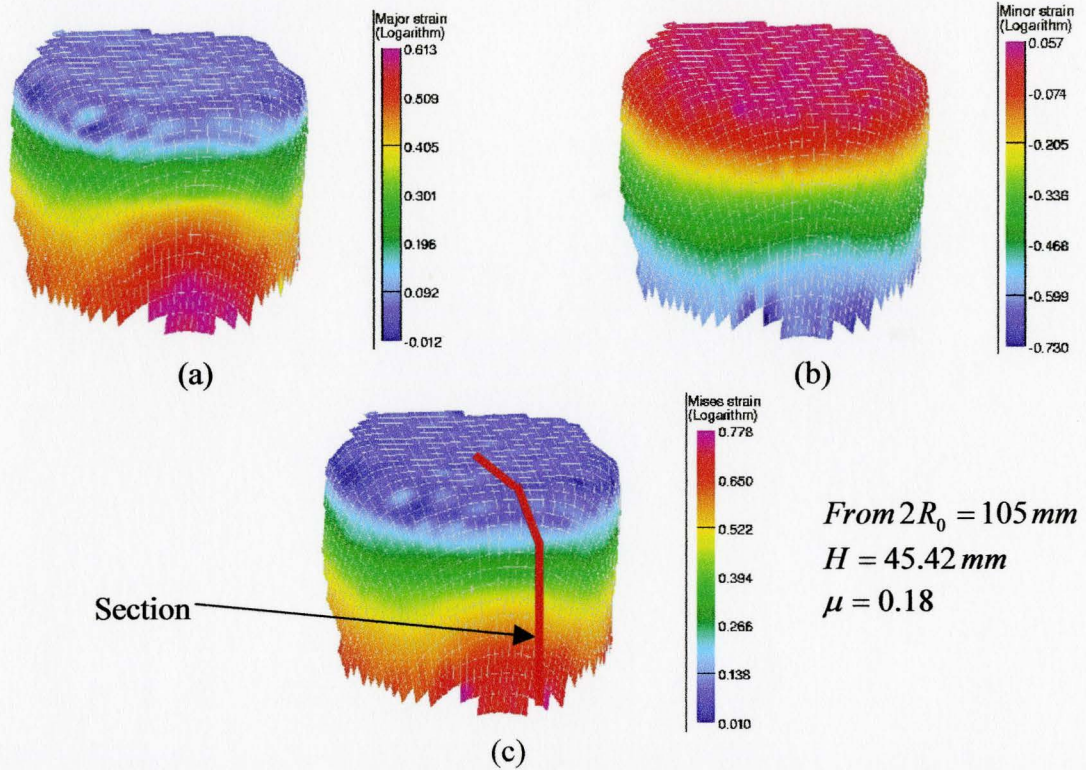


Figure 5.9 Strain distributions of a redrawn cup with (a) major, (b) minor and (c) Mises strains output parameter

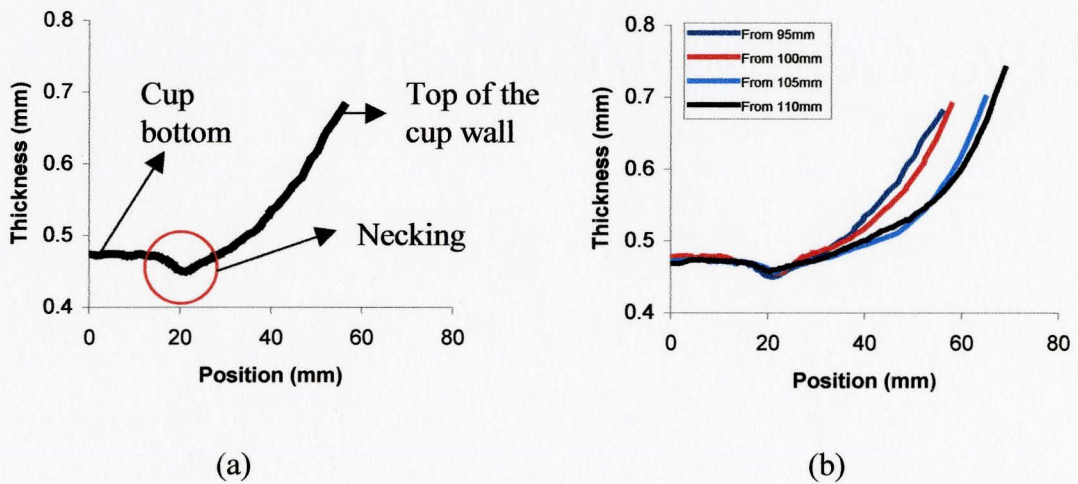


Figure 5.10 (a) Example of thickness distribution of a redrawn cup and (b) thickness distribution of redrawn cups from different initial cup heights

5.2.3 A comparison of deep drawing and redrawing

(1) Cup height

As mentioned before, the redrawing process can increase the cup or product height by decreasing the cup diameter. In this thesis, for all deep drawing experiments, a punch with 56.7mm diameter was used and for the redrawing operation, a punch applied with a diameter of 48mm was utilized. Thus, the diameter reduction of each pair of deep drawing and redrawing experiment has the same magnitude of 15.35%, which is shown in the equation below:

$$\text{Diameter reduction} = \frac{56.7 \text{ mm} - 48 \text{ mm}}{56.7 \text{ mm}} \times 100\% = 15.34\% \quad (5.3)$$

Table 5.3 shows the cup height difference of deep drawn and redrawn cups from various initial blank sheet sizes and the increments of all the cases are around 18.5%. A simple calculation is shown in Equation (5.4):

$$(1 - 15.34\%) \times (1 + 18.5\%) \approx 1 \quad (5.4)$$

This means the experimental results agree with the constancy of volume. With this basic theoretical support, the cup depths of each redrawing operation can be predicted if the information on punch diameter is available.

Table 5.3 Height difference of deep drawn and redrawn cups

	Cup height (mm)			
Initial blank sizes (mm)	95	100	105	110
Deep drawn cups	29.59	33.84	38.43	43.41
Redrawn cups	35.13	40.11	45.52	51.46
Increment (%)	18.72	18.53	18.45	18.54

(2) Punch load

Figure 5.11 shows an example of the difference in punch load between deep drawing and redrawing operations. As shown, the critical force for deep drawing stage is significantly higher than that of redrawing process. This is because of the larger drawing ratio for deep drawing process, as indicated below:

$$\text{Drawing ratio of deep drawing} = \frac{100\text{ mm}}{56.7\text{ mm}} = 1.76 \quad (5.5)$$

$$\text{Drawing ratio of redrawing} = \frac{56.7\text{ mm}}{48\text{ mm}} = 1.18 \quad (5.6)$$

Table 5.4 lists the critical drawing forces of each experiments and it was found that the punch load difference between each pair of deep drawing and redrawing operation is always about 32-35%. On the other hand, the drawing ratio difference in these sets of experiments is indicated below:

$$\text{Difference of drawing ratio} = \frac{1.76 - 1.18}{1.76} \times 100\% = 32.95\% \quad (5.7)$$

This result is very close to the drawing load difference. In addition, the difference gradually increases with increasing initial blank size, because the drawing ratio increases. Therefore, the results suggest that the maximum drawing load in the process is proportional to the drawing ratio. The advantage of this relationship is that the punch load of redrawing process can be approximated if the drawing load of first stage and the drawing ratio values for both processes are available.

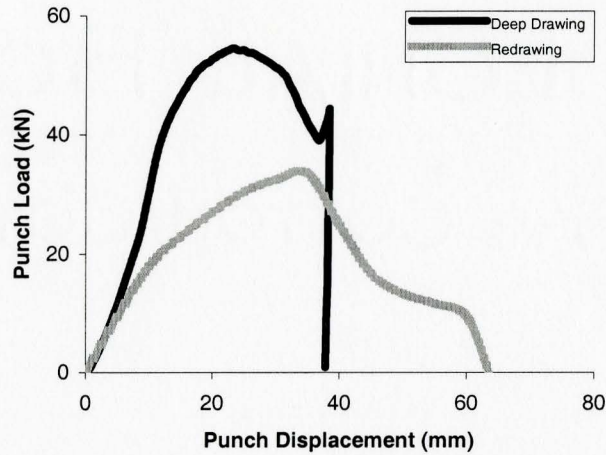


Figure 5.11 Punch load comparison of deep drawing and redrawing

Table 5.4 Critical drawing load comparison of deep drawing and redrawing

Initial blank sizes (mm)	Maximum drawing load (kN)			
	95	100	105	110
Deep drawn cups	41.14	46.16	53.29	57.21
Redrawn cups	27.86	31.04	35.31	37.58
Difference (%)	32.28	32.76	33.74	34.31

(3) Thickness distribution

Figure 5.12 shows a sample plot of difference in thickness distribution between deep drawing and redrawing processes. Also, Table 5.5 lists the smallest thickness of the drawn cups. As discussed in the previous chapter, in the deep drawing experiment with dry friction condition, the necking problem has already started if the drawing ratio is increased and this is why the thickness value in Region 3 in Figure 5.5(c) drops drastically with larger drawing ratio. However, in redrawing process, because the drawing ratio of each experiment always stays the same with a value of 1.18, the

thickness of each drawn sample is very close to each other with a value in the range of 0.450 mm - 0.455 mm. In summary, the thickness value at cup corner part, which is the thinnest area, decreases with increasing the drawing ratio.

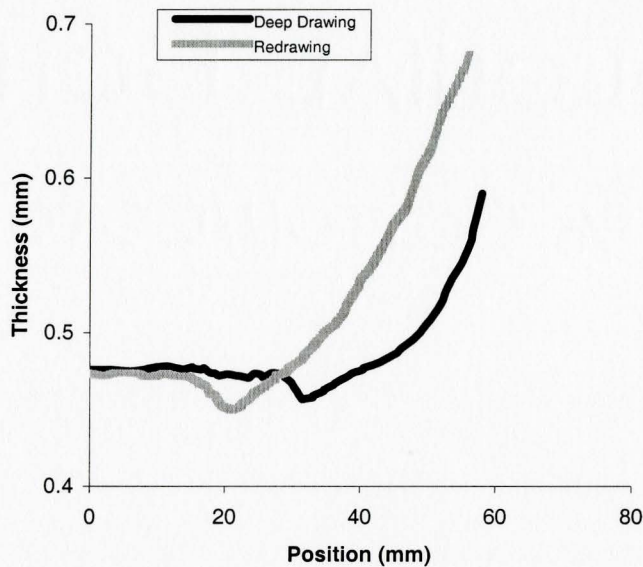


Figure 5.12 Thickness distribution comparison of deep drawing and redrawing

Table 5.5 Smallest thickness value comparison of different drawn cups

	Smallest thickness value (mm)			
Initial blank sizes (mm)	95	100	105	110
Deep drawn cups	0.457	0.452	0.444	0.432
Redrawn cups	0.452	0.455	0.456	0.453

5.2.4 Deep drawing process with centre hole blank

Eight sets of blanks with 110 mm diameter and different centre hole sizes were investigated in this drawing experimental work under dry friction condition. The centre hole diameter increased from 0 mm to 35 mm with a 5 mm step. Figure 5.13 shows the

cups drawn from these sets of blanks. From the figure, it is to be noted that three different cases were observed after the cup was drawn: (1) the cup was successfully drawn into the die cavity from the blanks with the initial centre hole diameters of 0 mm and 5 mm; (2) the cup cracked at the centre hole edge while it was drawn from the blanks with initial centre hole diameters from 10 mm to 20 mm and (3) if the initial centre hole diameter was larger or equal to 25 mm, the punch just went through the hole resulting an “L” shape ring and no crack occurred.

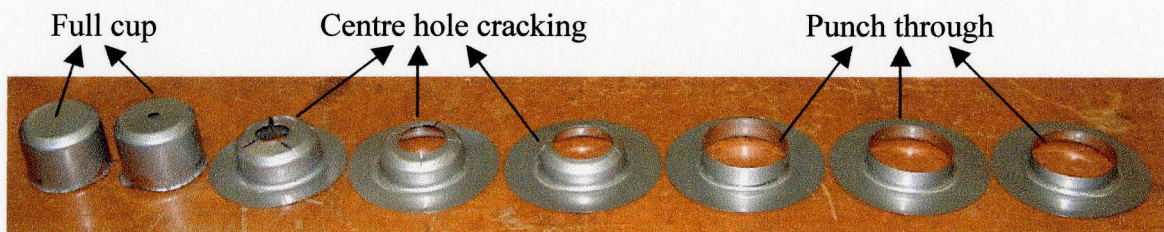


Figure 5.13 Deep drawn cups from centre hole blank with different initial centre hole diameter: from left to right, 0 mm to 35 mm

The product profiles from this process were investigated in terms of the cup height, expanded centre hole diameter and the remaining flange size (Table 5.6). It is to be noted that if the punch traveled through the centre hole, the hole diameter is equivalent to the punch diameter.

Table 5.6 Cup height, remaining flange size and centre hole diameter from different centre hole blanks

Initial centre hole size (mm)	0	5	10	15	20	25	30	35
Cup height (mm)	43.31	43.51	25.95	21.54	19.21	18.41	15.87	13.27
Flange diameter (mm)	Full cup	Full cup	93.66	103.01	106.98	108.75	109.37	109.76
Centre hole diameter (mm)	0	6.87	21.74 (Crack)	29.93 (Crack)	38.94 (Crack)	Punch through	Punch through	Punch through

In Figure 5.14, the drawing load and clamping force versus punch displacements of three different cases mentioned before were plotted. As shown in Figure 5.14(a), the drawing and clamping load curves from a full drawn cup were very similar to those of regular deep drawing (Section 5.2.1). For the centre hole cracking case, the two load curves gradually increased and dropped sharply at the time of cracking, as shown in Figure 5.14(b). In Figure 5.14(c), the punch load and clamping force reached the peak point when the punch totally traveled through the centre hole and decreased smoothly until the end of the process.

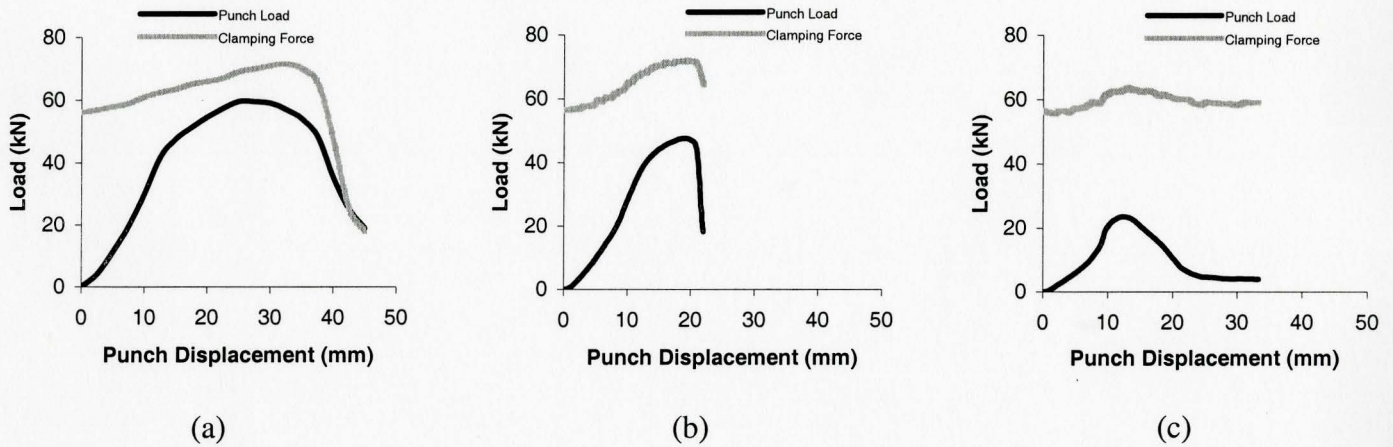


Figure 5.14 Punch load and clamping force versus punch displacements plots from deep drawing with centre hole blanks process in different cases: (a) full drawn cup, (b) cup cracking at centre hole and (c) punch through the centre hole

It is to be noted that the initial centre hole size has influence on punch load in the process for all three cases. As shown in Figure 5.15(a), for a full drawn cup, the maximum punch force had a slightly larger value from 5 mm diameter centre hole blank than that of the one without a hole. For centre hole cracking case in Figure 5.15(b), the smaller the initial centre hole diameter was, the more the punch traveled until the cup cracked and the larger was the magnitude of the critical punch load. If the punch went through the centre hole, as shown in Figure 5.15(c), the critical punch load had a larger value and the punch traveled for a larger amount in the process with a smaller initial centre hole diameter blank. The information can be obtained from these phenomena is that the punch is easier to travel through the hole and the drawn product has a smaller cup wall size if the drawing process is operated using a blank with larger initial centre hole size.

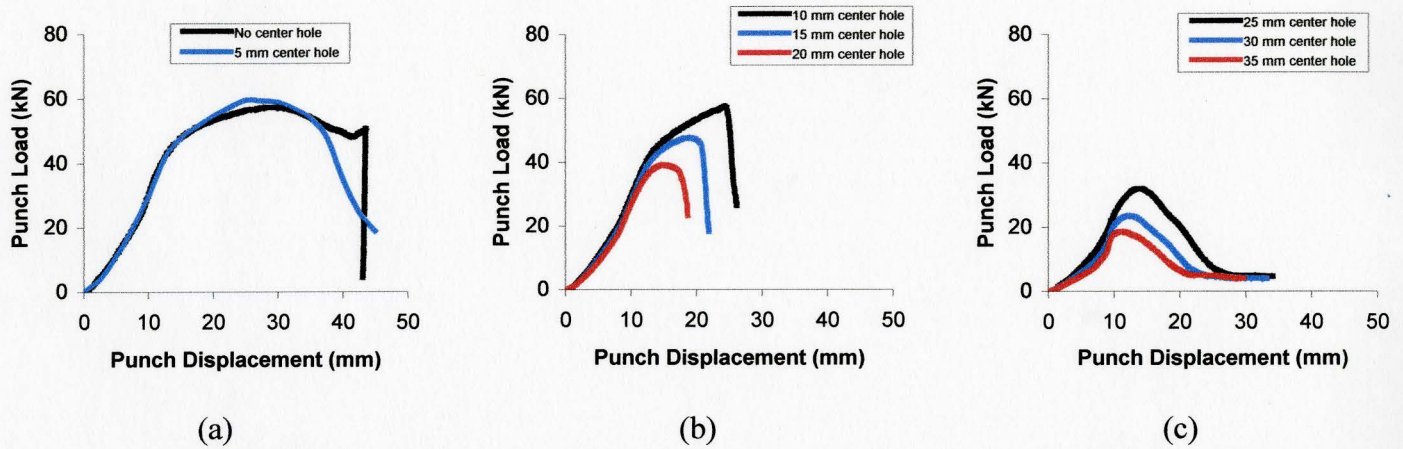


Figure 5.15 Comparison of punch loads from deep drawing process with blanks of various initial centre hole diameters in different cases: (a) full drawn cup, (b) cup cracking at centre hole and (c) punch through the centre hole

Argus system was also utilized to measure the strain distributions along the product profiles drawn from blanks with different initial centre hole diameters. Major, minor and Mises strains were again the three strain output parameters that were analyzed. Figure 5.16 shows the images of Mises strains obtained by Argus system for three different cases. Once again, a section along the product profile was defined to plot the thickness distribution.

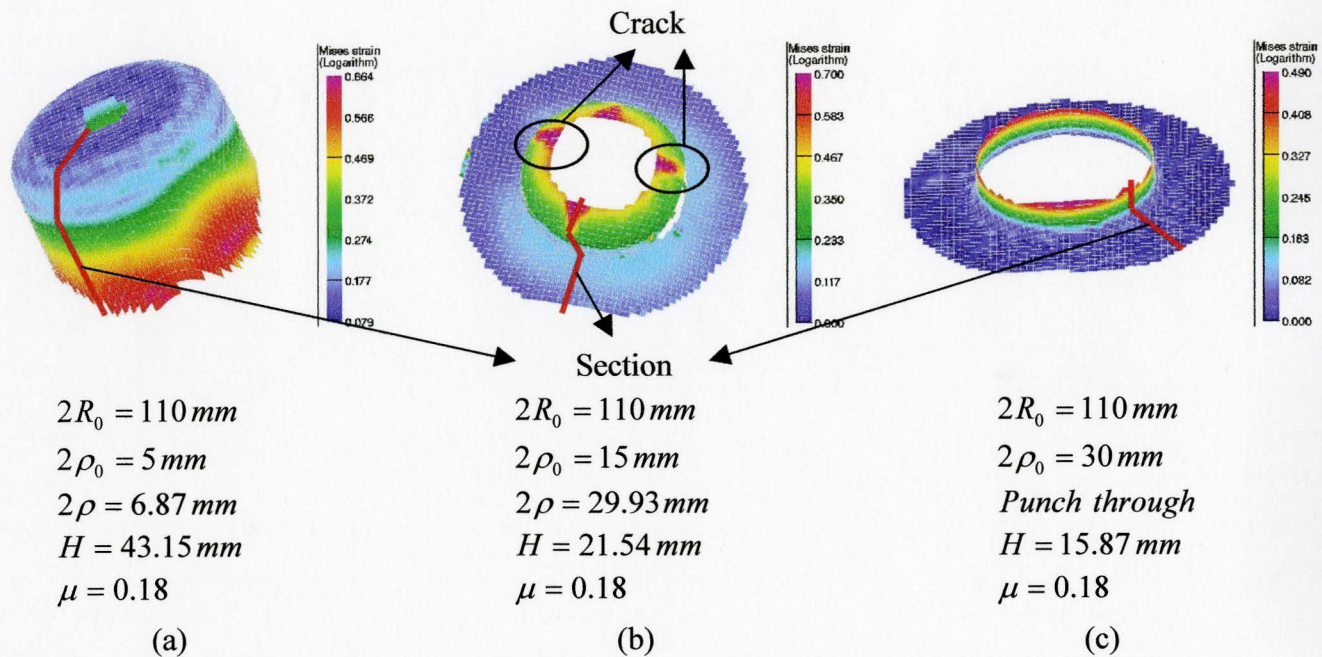


Figure 5.16 Mises strain output from Argus system for different cases: (a) full drawn cup, (b) cup cracking at centre hole and (c) punch through the centre hole

Using the same method as described in the previous section, the thickness along the cup was obtained from the information of major and minor strains as well as the constancy of volume (Equation 5.1 and 5.2). Figure 5.17(a) shows the thickness distribution of a fully drawn cup from a centre hole blank. In the figure, the thickness had a low value around the centre hole area, gradually increased and became constant for the rest of the cup bottom. A similar necking phenomenon occurred at the cup corner part and the thickness of the product increased progressively to the top of the cup wall. In Figure 5.17(b), because the centre hole cracked in the process, the thickness had a zero value at the centre hole edge. At cup wall area, the thickness increased towards the flange region and then stayed stationary. When the punch traveled through the centre hole, the thickness profile of the product was very similar to that of the centre hole

cracking case except that the thickness value was not zero at the edge of the centre hole edge, as shown in Figure 5.17(c).

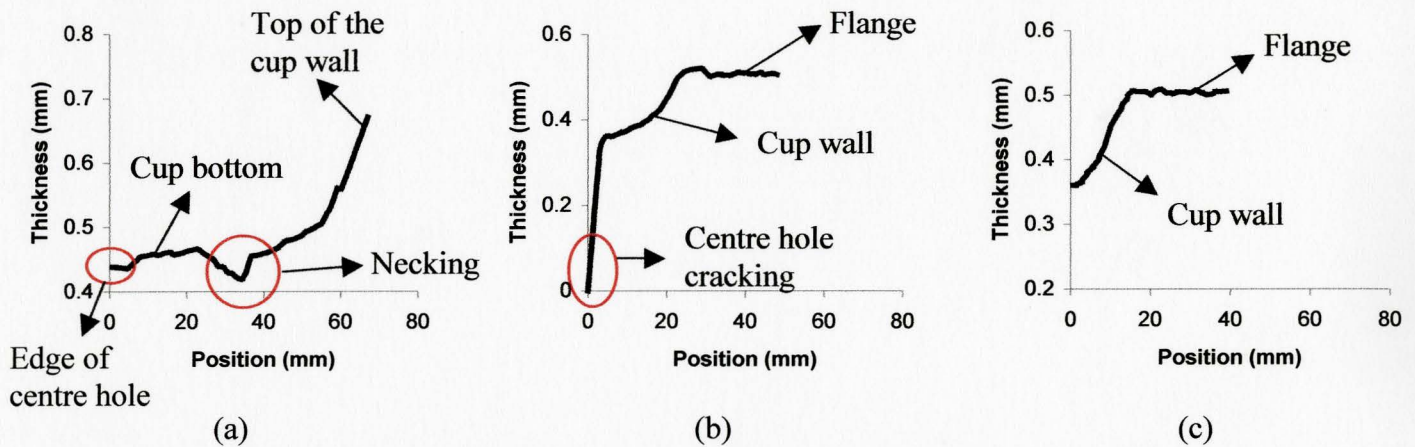


Figure 5.17 Thickness distribution of drawn cups from deep drawing with centre hole blanks process in different cases: (a) full drawn cup, (b) cup cracking at centre hole and (c) punch through the centre hole

5.3 FE Simulation Results and Validation

5.3.1 A comparison of FE simulation and experimental results

FE simulation results of deep drawing, redrawing and deep drawing with centre hole blank processes are presented in this sub-section. The results are then compared with those obtained experimentally. All the input data in the model, including the properties, tooling profiles and friction coefficients, were based on the real experimental test conditions. It is to be noted that friction coefficient values of 0.18 and 0.04 were used for dry condition and Teflon lubrication condition.

(1) Deep drawing and redrawing processes

Figure 5.18 shows an example of the deep drawn and redrawn cup geometry. All experiment and simulation test results of drawn cup height are given in the Appendix G.

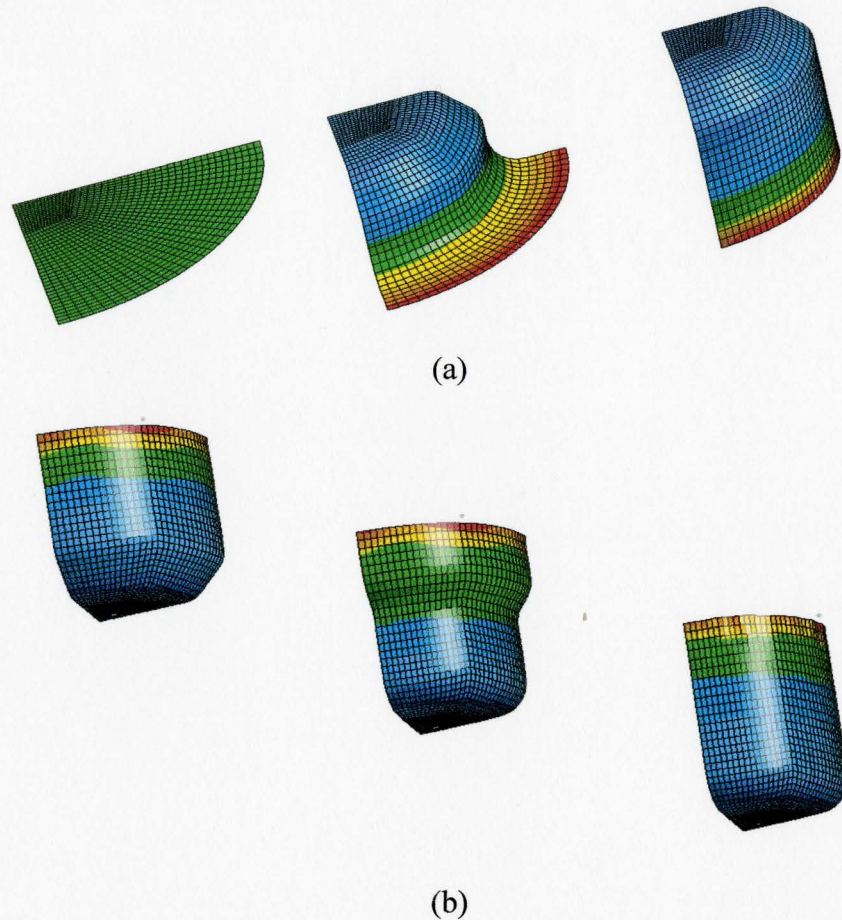


Figure 5.18 FE simulation cup geometry of (a) deep drawing and (b) redrawing processes

A sample comparison of deep drawing and redrawing load plots between experiment and FE simulation are shown in Figure 5.19. From the graph, the punch load curves from simulation matches well with the experiments, except for the ironing part. This is because in order to simulate this contact situation, penalty factor has to be

adjusted. However, ironing is not the major research interest, so it is not included in the finite element model to save on the processing time. Furthermore, for clamping force, the experimental curve is not as smooth as the simulation one, because many uncertainties occur during the experimental process, such as unknown unsymmetrical loading, machine and load cell noise etc. On the other hand, in simulation calculation, the process is very stable and consistently leads to a smoother curve. However, the curve trend is very similar to the experimental data and the magnitudes of the both curves are in the same range. All different test cases as presented in Appendix G indicate that simulation work reasonably matches the experimental data.

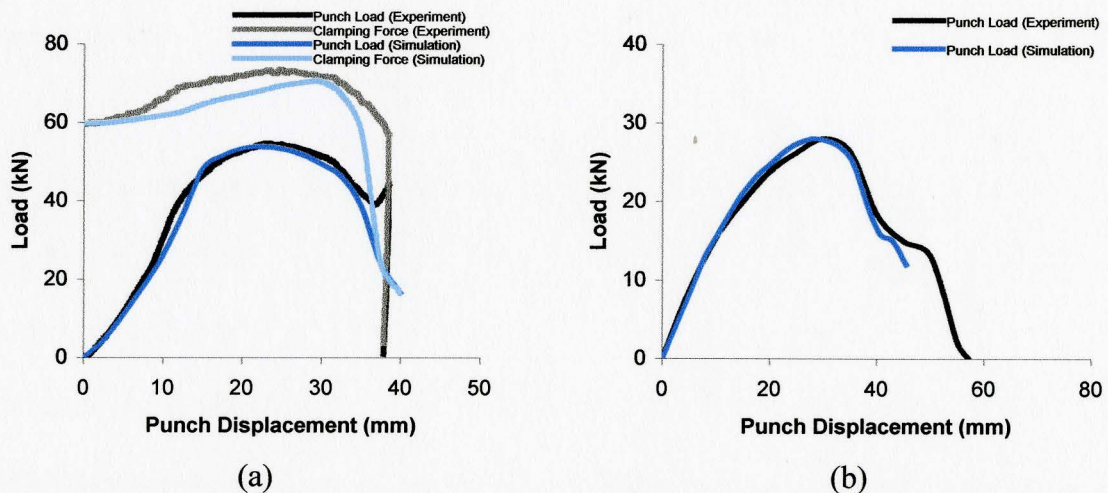


Figure 5.19 Sample of load curve comparison between experimental and simulation work: (a) deep drawing and (b) redrawing stages

Figure 5.20 shows a comparison of thickness distribution curve between experiment and simulation work for deep drawing and redrawing processes. Similar comparisons for

the different drawing conditions are shown in Appendix G. Once again, the simulation curves agree well with the experimental ones with some acceptable error.

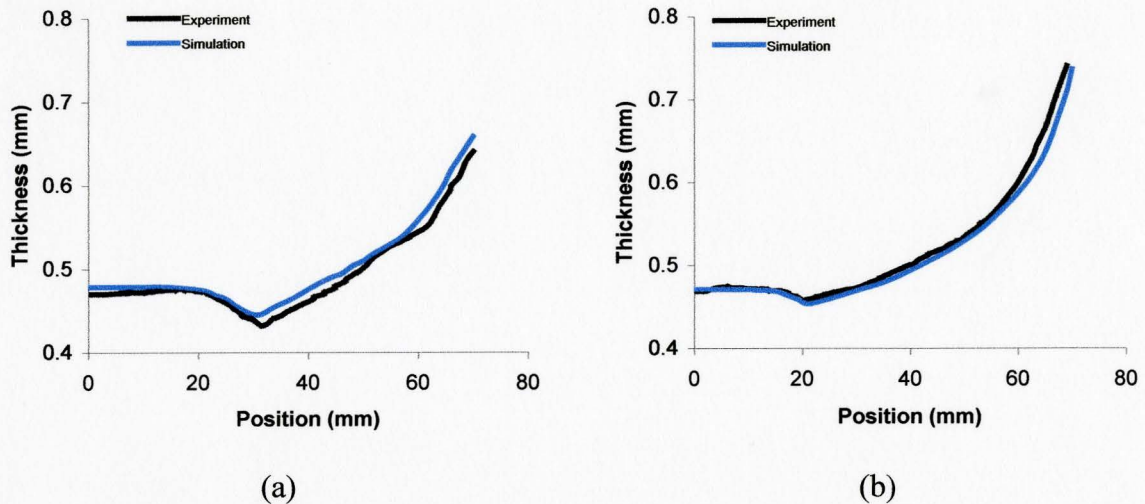


Figure 5.20 Sample of thickness distribution comparison between experimental and simulation work: (a) deep drawing and (b) redrawing stages

(2) Deep drawing process with centre hole blank

Figure 5.21 shows an example of deep drawn cup geometry from centre hole blank. All the comparisons between experiment and simulation test results in terms of drawn cup height, centre hole diameter and remaining flange size are given in the Appendix G. Furthermore, a comparison of the final cup profiles between experimental and FE simulation work in the three different cases, as mentioned above, is shown in Figure 5.22.

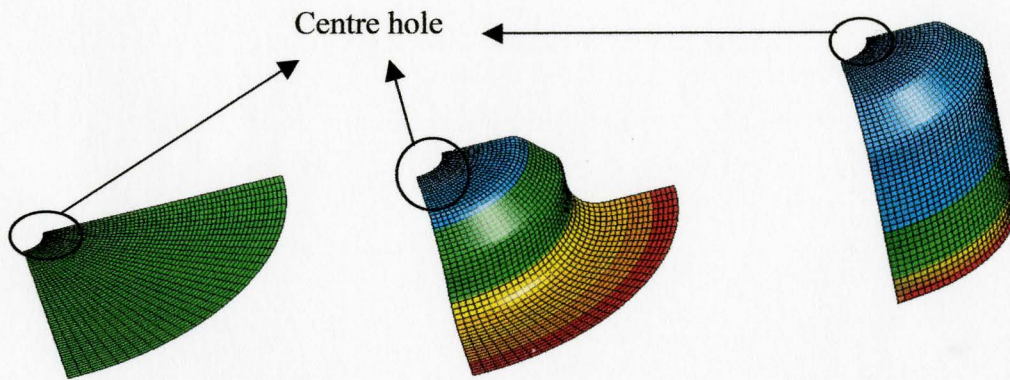


Figure 5.21 FE simulation cup geometry of deep drawing with centre hole blank process

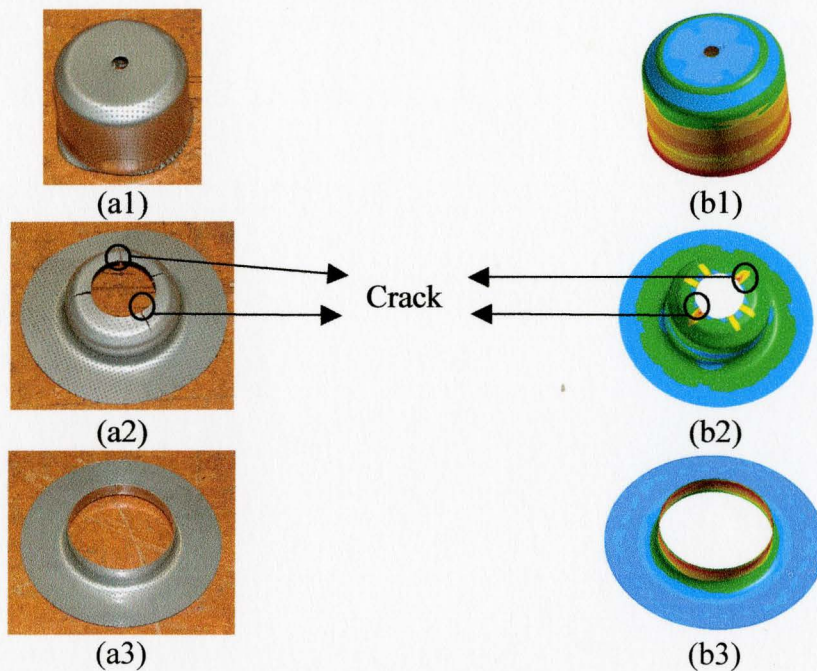


Figure 5.22 A comparison of final cup profile in the case of (a1, b1) successful deep drawing process, (a2, b2) cup cracking at centre hole edge and (a3, b3) punch going through the centre hole between experiment and FE simulation

Comparison between experimental and simulation work in terms of punch and clamping forces versus punch displacements and thickness distributions along the product profiles are given in Figure 5.23, 5.24 and AG.4. From the figures, the simulation curves matched well with those of experimental work.

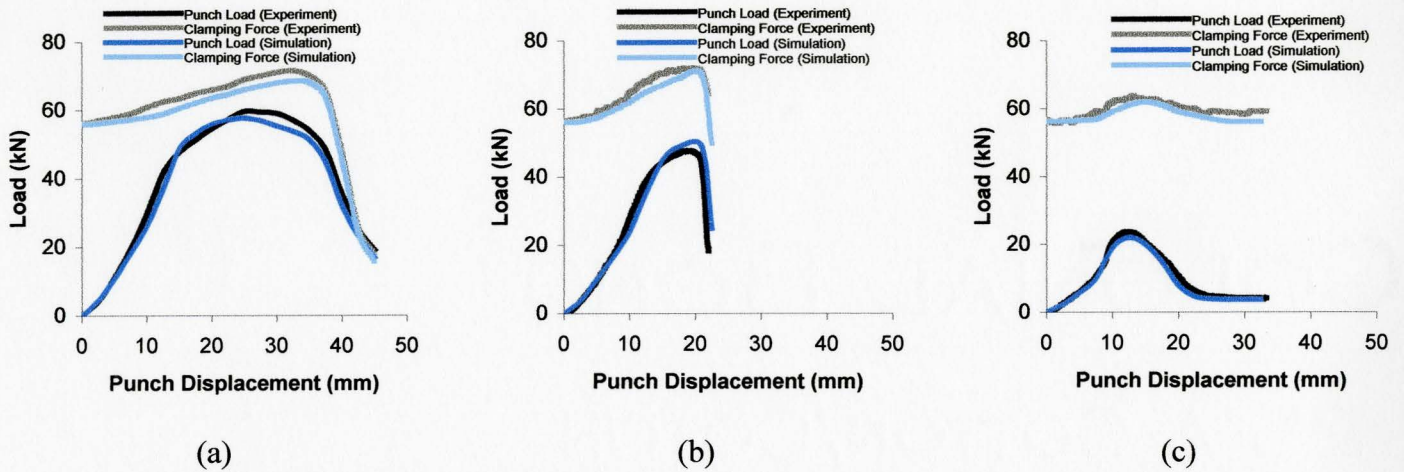


Figure 5.23 A comparison between experimental and simulation work of punch load and clamping force versus punch displacements plots from deep drawing with centre hole blanks in different cases: (a) full drawn cup (b) cup cracking at centre hole and (c) punch through the centre hole

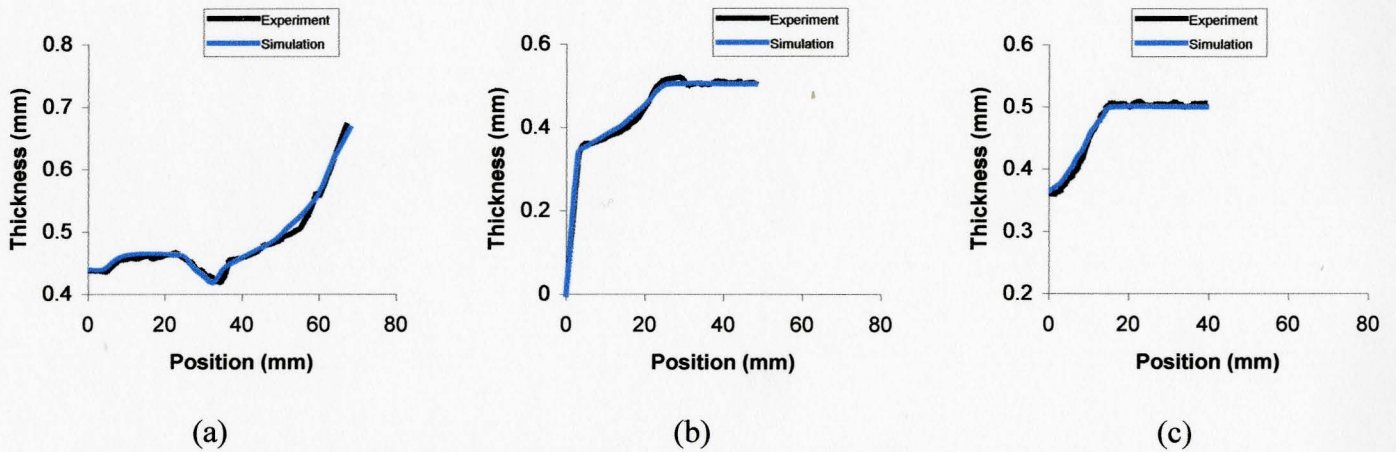


Figure 5.24 A comparison between experimental and simulation work of thickness distributions along the cup profiles from deep drawing with centre hole blanks in different cases: (a) full drawn cup (b) cup cracking at centre hole and (c) punch through the centre hole

5.3.2 Process signatures and strain paths in deep drawing versus the forming limit diagram

The FE simulation can provide a deeper understanding of the material flow behavior than what is obtainable from experiments. The strain data calculated by FE software can be plotted as minor strain versus major strain curve to achieve so called process signatures at different heights of deep drawing and redrawing. The strain paths of some critical regions, such as the element on the edge of the hole and the outmost flange area for a centre hole blank, can be analyzed and plotted along with the forming limit diagram (FLD) to further understand material flow and strain development. The plot of forming limit curve (FLC) for stainless steel 304 is based on the experimental data from Andersson et al. [49]

(1) Process signatures of deep drawing and redrawing processes

After each simulation run, a strip of elements on the blanks, as shown in Figure 5.25, was traced so the major and minor strains of these elements were exported to develop the process signature curves in FLD.

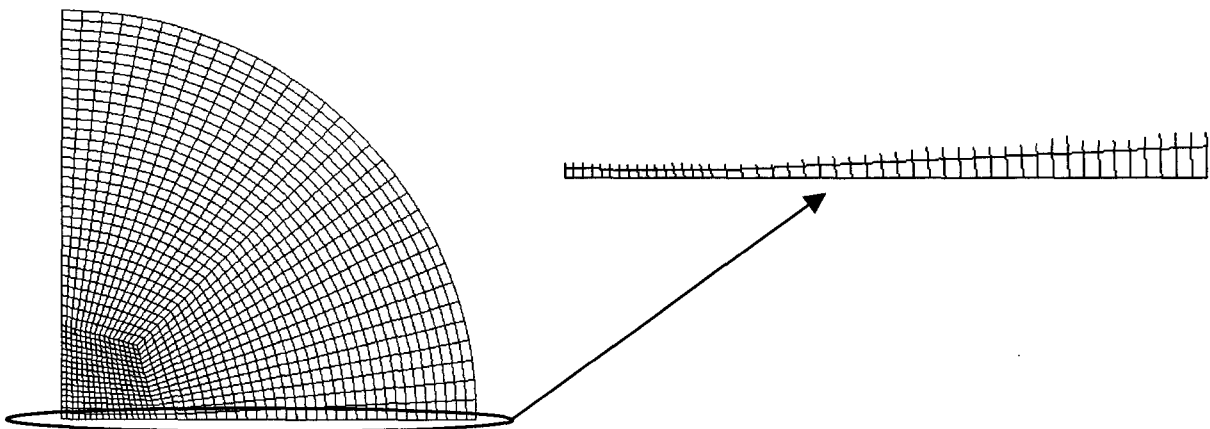


Figure 5.25 A strip of elements on the blank

Figure 5.26(a, b) show the major and minor strains plot curves in FLD strain space at different cup heights for deep drawing and redrawing. As expected, for both processes, the curves approached progressively towards the left side of FLC with an increase in cup heights. It is because with the increasing of the cup height, the maximum drawing force was reached. From Figure 5.26(c, d), the final state of the process signature curves from a larger drawing ratio operation approached close to the FLC, because the limit drawability of the material was gradually reached.

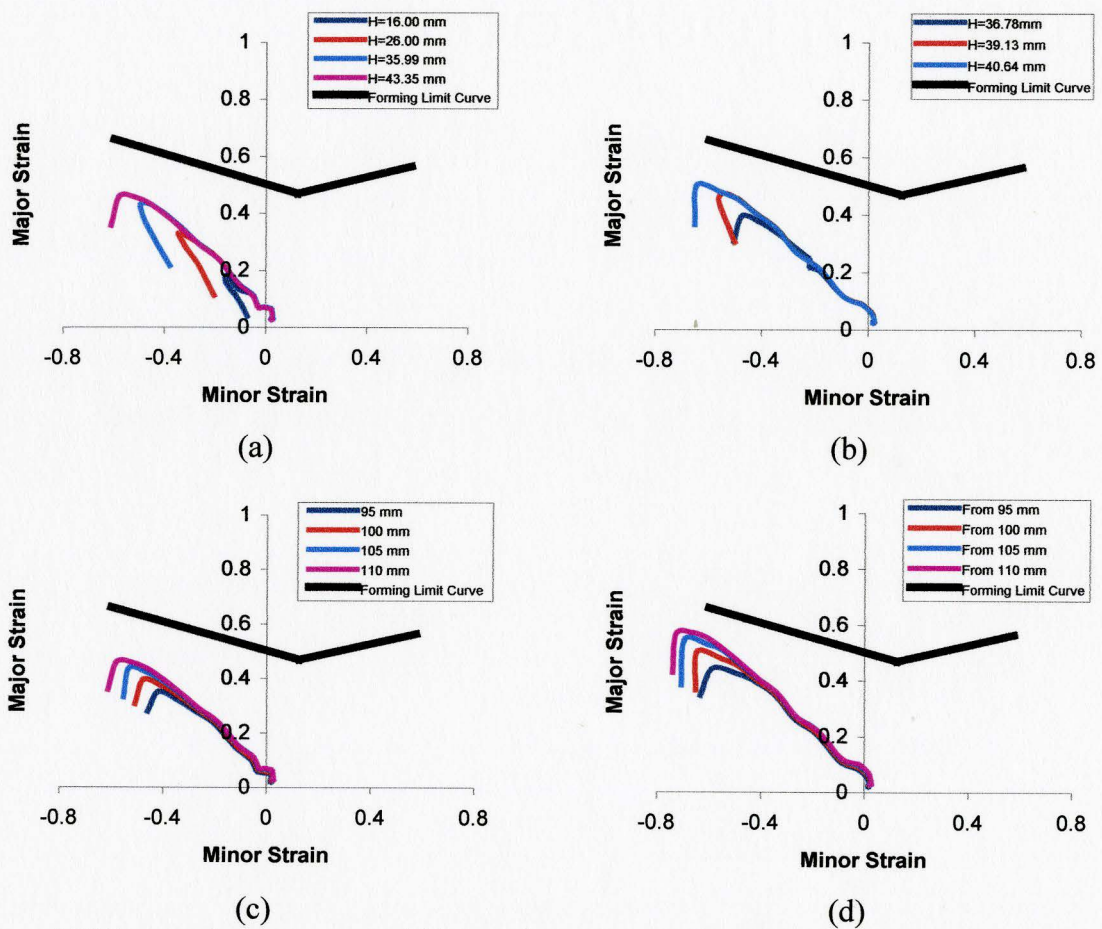


Figure 5.26 Process signature curves of (a) deep drawn cup and (b) redrawn cup at different heights, (c) deep drawn cups from different initial blank diameters and (d) redrawn cups from different previous cup heights

Figure 5.27 shows a comparison of the final states between deep drawing and redrawing in the FLD. As expected, the process signature curves from redrawing are closer to the FLC than those from deep drawing. If a blank is drawn at exceeding LDR condition, the cup will crack in the middle of the process and its process signature curves are shown in Figure 5.28. From the graph, there is one point appearing above the FLD, which means the product fails at this point.

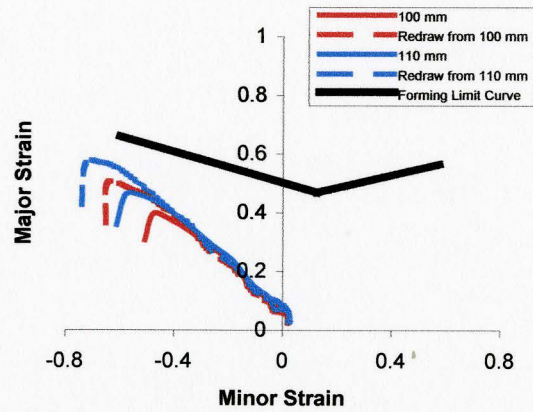


Figure 5.27 A comparison of process signature curves between deep drawing and redrawing in forming limit diagram

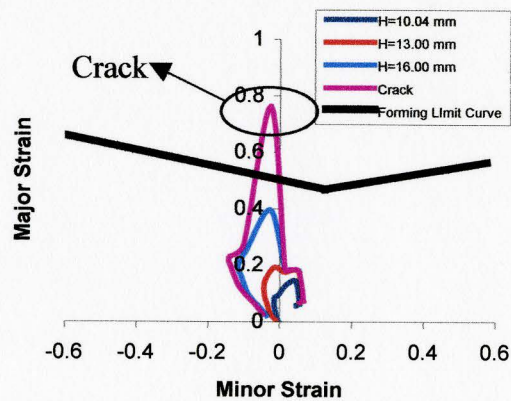


Figure 5.28 Process signature curve at crack condition

(2) Strain paths of deep drawing process with centre hole blank

In this process, an element on the centre hole edge and another one on the outmost edge of the blank were traced, as shown in Figure 5.29 (elements A and B). The major and minor strains of these two elements during the whole process were exported to plot the strain paths so that the material flow behaviors could be studied.

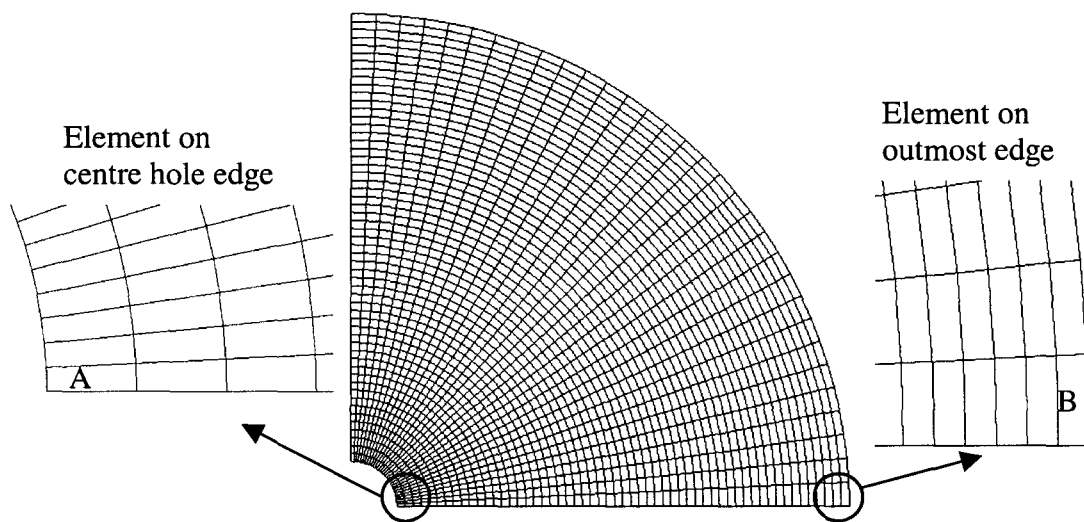


Figure 5.29 Elements traced on centre hole blank

Figure 5.30(a) shows the strain paths of Element A and B during the process when a full cup was drawn. Both paths started at the origin of the FLD and ended in the region below the FLC. Furthermore, the strain path of Element B approached to the FLC more than that of Element A. The information obtained was that the cup had a less chance to crack at the centre hole edge than those of other failure modes, such as cracking at the corner of the cup. If the cup cracked at the centre hole edge, the strain path of Element A traveled above the FLC, which means the forming limit was exceeded, as shown in

Figure 5.30(b). In addition, the small increment of the strain path for Element B showed that the flange of the cup was only drawn into die cavity by a small amount. In Figure 5.30(c), the strain path of Element B stayed stationary at the origin and it means that the material did not flow into the die cavity. On the other hand, the strain path of Element A gradually approached to the FLC until the punch traveled through the centre hole, because the size of the centre hole was expanded to the value of the punch diameter. Therefore, from the strain paths in these figures, one can provide a better understanding of the material flow behavior during the process in these three different cases.

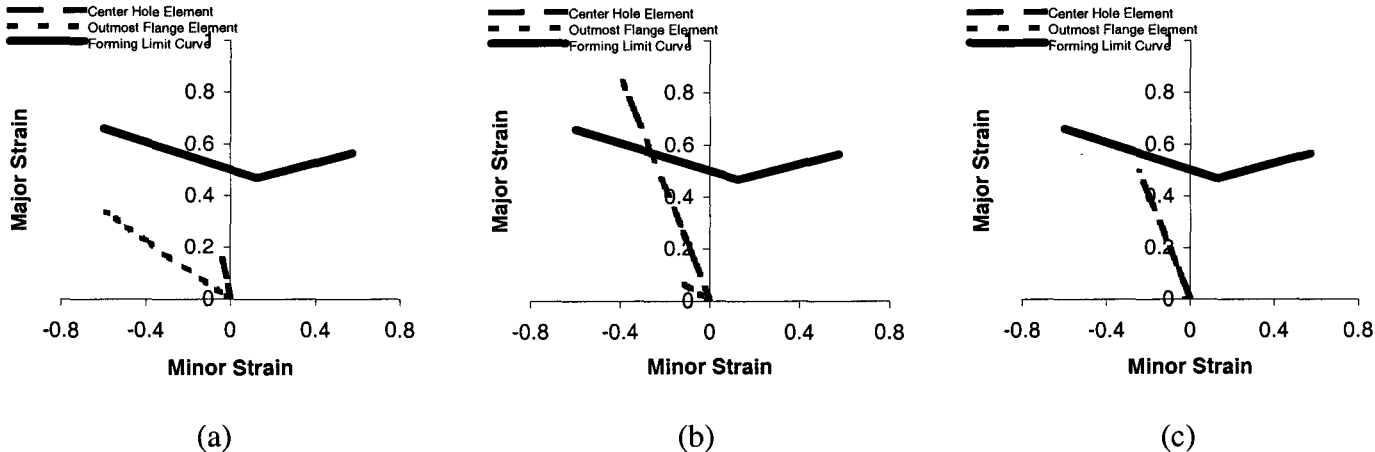


Figure 5.30 Strain paths of centre hole and outmost edges elements during deep drawing with centre hole blanks process in different cases: (a) full drawn cup (b) cup cracking at centre hole and (c) punch through the centre hole

5.3.3 Influence of tooling geometry on drawability of sheet material

As discussed in Chapter 2, an important advantage of FE simulation is to develop further analysis in deep drawing and redrawing processes under various tooling geometry conditions, which is not obtainable by experimental work. In this sub-section, the

influences of punch profile radius and die corner radius on drawability of sheet material in cup drawing process are investigated in terms of punch load during the operation and thickness distribution along the cup profile.

(1) Punch profile radius

Three punches with various profile radii of 6.35 mm, 9.525 mm and 12.7 mm for deep drawing and 3.175 mm, 6.35 mm and 12.7 mm for redrawing, were modeled to operate the processes. From Figure 5.31(a, b), the maximum punch force value altered slightly with an adjustment in the punch profile radius. In addition, as shown in Figure 5.31(c, d), the thickness distribution of different cases was very similar to each other for both drawing processes. Therefore, a conclusion is that punch profile radius does not affect the drawability of sheet material in deep drawing and redrawing processes drastically. This result actually agrees well with what existing in the literature [31].

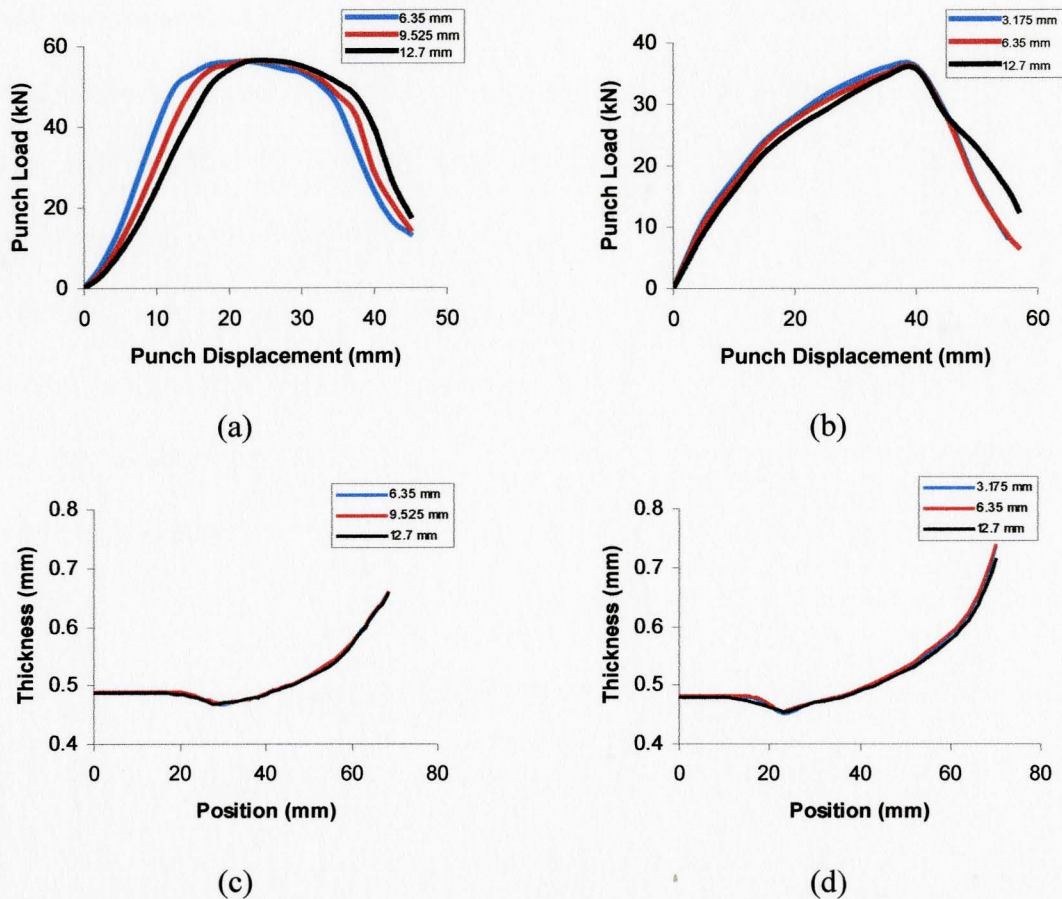


Figure 5.31 Effect of punch profile radius on (a) punch load for deep drawing, (b) punch load for redrawing, (c) thickness distribution for deep drawing and (d) thickness distribution for redrawing

(2) Die corner radius

The model was also developed using dies with different corner radii, which were 3.175 mm, 6.35 mm and 9.525 mm for deep drawing and 3.175 mm, 6.35 mm and 12.7 mm for redrawing. From the punch load versus punch displacement curves in Figure 5.32(a, b), the critical punch load value decreased with an increase in die corner radius for both drawing processes. Furthermore, as shown in Figure 5.32(c), the lowest thickness value in the cup profile, which is at the cup corner region, was proportional to the die corner radius. This means that the cup is not easy to crack if a die with large

corner radius is applied in the deep drawing process. For redrawing in Figure 5.32(d), the highest thickness value of the cup decreased with an increasing in die corner radius. It is also a positive effect because the most possible failure mode for redrawing is wall wrinkling instead of cracking and a lower thickness value at the top wall region indicates that the cup does not intend to wrinkle. From all of the above information, one can conclude that an increase in the die corner radius value has a positive influence on drawability of sheet material for both deep drawing and redrawing processes. This result also is in a good agreement with the information existing in the previous work [18].

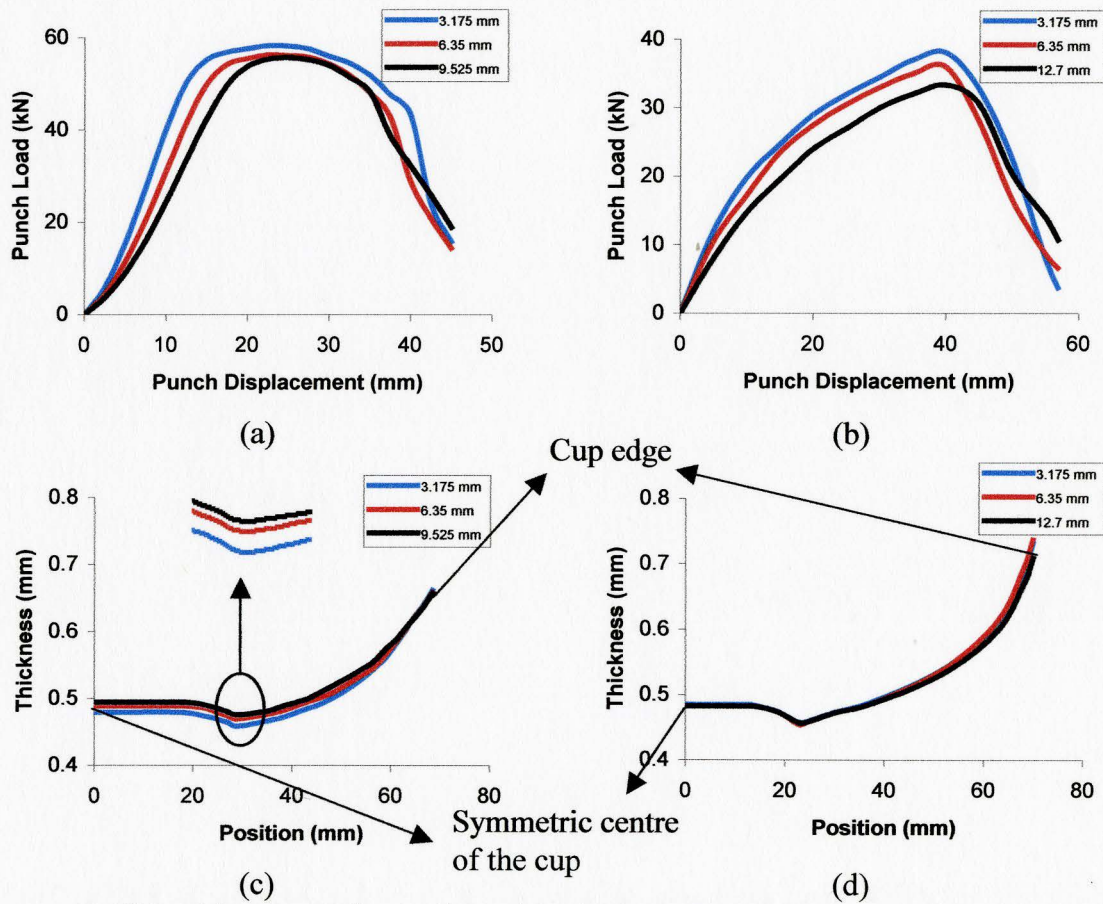


Figure 5.32 Effect of die corner radius on (a) punch load for deep drawing, (b) punch load for redrawing, (c) thickness distribution for deep drawing and (d) thickness distribution for redrawing

5.3.4 Determination of LDR from FE simulations

(1) Deep drawing and redrawing processes

A calculation flow chart for the prediction of LDR is given in Appendix H. On exceeding LDR condition, the model failed, cracking at the corner part of the cup for deep drawing or wall wrinkling for redrawing, as shown in Figure 5.33. It is to be noted that in redrawing process, every single adjustment of initial blank diameter and the second punch diameter had a value of 5 mm instead of 1 mm in the deep drawing stage, as shown in Appendix AH.2. This was because too much simulation work would be required if an adjustment of only 1 mm in diameter for every simulation was made. Apparently, this issue resulted in a larger error magnitude than that of deep drawing process.

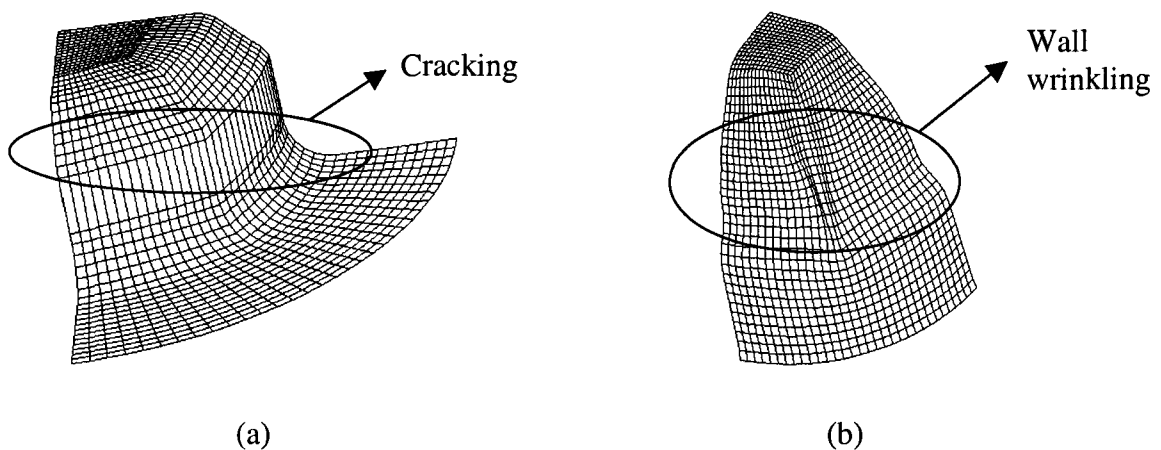


Figure 5.33 Failure mode: (a) cracking for deep drawing and (b) wall wrinkling for redrawing processes

Appendix I lists all the simulation results to determine the limiting drawing ratio for both deep drawing and redrawing processes and these values were shown in Table 5.7.

Table 5.7 FE simulation results of LDR for deep drawing and redrawing processes at experimental conditions

	Dry Friction ($\mu = 0.18$)	Teflon Condition ($\mu = 0.04$)
LDR of deep drawing process	2.116	2.434
LDR with one redrawing process	3.000	3.600

(2) Deep drawing process with centre hole blank

The simulation work to determine the LDR for this process followed the same calculation flow chart as the one for deep drawing (Figure AH.1). When the drawing ratio exceeds the critical value, the part fails in two different modes: cracking at the corner of the cup or cracking at the centre hole edge, as shown in Figure 5.34.

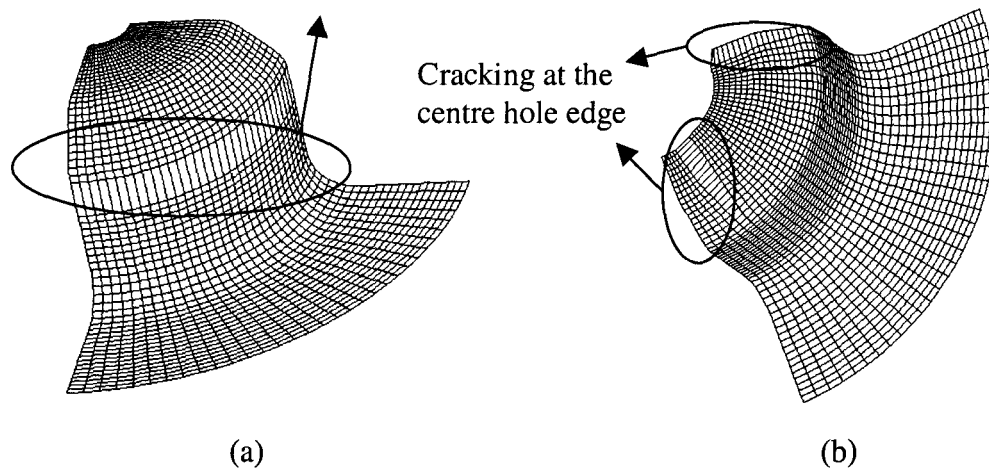


Figure 5.34 Failure modes for deep drawing with centre hole blank: (a) cracking at the corner of the cup and (b) cracking at the centre hole edge

Four sets of blanks with different initial centre hole diameters, 5 mm, 6 mm, 7 mm and 8 mm, were investigated in the simulation work under dry friction condition. The

simulation procedures to determine the limiting drawing ratio for all the sets of blanks are given in Appendix I. The resulting LDR values are listed in Table 5.8.

Table 5.8 FE simulation results of LDR for deep drawing with centre hole blank process at dry friction condition

Initial centre hole diameter (mm)	5	6	7	8
LDR of the process	2.116	2.116	2.116	2.046

From Appendix I and Table 5.8, on exceeding LDR condition, the cup drawn from the blank with 5 mm, 6 mm and 7 mm initial centre hole diameter cracked at the corner region (Figure 5.34(a)) and the LDR values are the same as that of the deep drawing from a blank without a centre hole. For the 8 mm initial centre hole diameter blank, the cup cracked at the centre hole edge (Figure 5.34(b)) when the critical drawing ratio was reached and the LDR value is smaller than those of the processes from other blanks.

Another series of simulation work was developed to determine the critical flanging ratio $k_p = \frac{r_1}{\rho_0}$ of three different cases, as mentioned in the previous section. In this set of simulation, the punch radius r_1 was constant with a magnitude of 56.7 mm and the blank diameter was kept as 110 mm. Figure AH.3 shows the logical flow chart of this simulation process and the all the results are given in Appendix I. From Table AI.9, the critical flanging ratio for different cases are shown below:

$$\begin{aligned}
6.300 \leq k_p < \infty & \quad \text{Full drawn cup} \\
2.363 \leq k_p < 6.300 & \quad \text{Cracking at centre hole} \\
0 \leq k_p < 2.363 & \quad \text{Punch through}
\end{aligned}
\tag{5.8}$$

5.4 Theoretical Results and Validation

5.4.1 Mathematical model validation

In order to apply the theory derived in Chapter 3 to the experimental test cases, the first and most important issue is to test the accuracy of the theoretical results. The validation program consisted of two steps:

- (1) Calculation of theoretical limiting drawing ratio for deep drawing and redrawing

The theoretical LDR values for both deep drawing and redrawing operations was calculated by substituting the experimental parameters, such as material properties (Table 4.1), tooling geometry (Table 4.2 and 4.3) and friction coefficients into the mathematical expressions presented in Chapter 3 and Appendix F (Equation (3.9) and (AF.8)). By using Microsoft Excel spread sheet, the results shown in Table 5.9 were obtained.

Table 5.9 Theoretical LDR for deep drawing and redrawing processes for identical experimental conditions
(Refer Table 4.1 for all the material properties and Table 4.2 and 4.3 for the tooling geometry)

	Dry Friction ($\mu = 0.18$)	Teflon Condition ($\mu = 0.04$)
LDR of deep drawing process	2.017	2.332
LDR with one redrawing process	2.738	3.296

(2) Validation of the theoretical values by simulation

Since the validation of finite element model has already been discussed, the next step was to determine how close were these theoretical results to those from FE simulation. By the comparing the magnitudes in Table 5.9 to those in Table 5.7, error percentage values between theoretical model and FE simulation for both deep drawing and redrawing were calculated and listed in Table 5.10.

Table 5.10 Error percentages of LDR values between theoretical model and FE simulation

	Error (%)	
	Dry Friction ($\mu = 0.18$)	Teflon Condition ($\mu = 0.04$)
Deep drawing process	4.68	4.19
Redrawing process	8.73	8.44

Considering too many approximations in the theoretical model, this error range is reasonable and acceptable.

5.4.2 Influence of material and tool geometric parameters on drawability using the theoretical model

Since the mathematical model has already been validated by comparing with the FE simulation results, the model was utilized to analyze the effect of various parameters in the drawing and redrawing operations. In the equations presented earlier (Chapter 3), there are five major parameters, which affect the final results of LDR, and they are material strain-hardening factor n , material normal anisotropy value \bar{R} , material yield

stress σ_y , die corner radius r_d & r_{d1} and friction coefficient in the flange area μ . It is to be noted that in the study of each parameter, the relationship between the certain parameter and LDR value were plotted at two different conditions: dry friction ($\mu = 0.18$) and Teflon condition ($\mu = 0.04$). The purpose is to prove the consistency of the results. In addition, for the effect of friction coefficient, two different die corner radii of 6.35 mm and 10 mm cases were investigated with the same objective.

(1) Material strain hardening exponent n

A relationship between material strain hardening exponent n and the LDR is shown in Figure 5.35. The LDRs of both drawing operations decrease when the strain-hardening factor with small magnitude increases until some critical point and they increase again afterwards with increasing of this strain hardening exponent. Since the normal stress on the die is proportional to the strain hardening exponent, an increase in strain hardening exponent results in an increase in the friction force at flange area. This explains why the LDR decreases initially with an increase in strain hardening exponent. However, the material has a larger ultimate tensile stress with a larger strain hardening exponent and it is the reason why LDR is proportional to strain hardening exponent afterwards. This result is consistent with Hosford and Caddell's work [50].

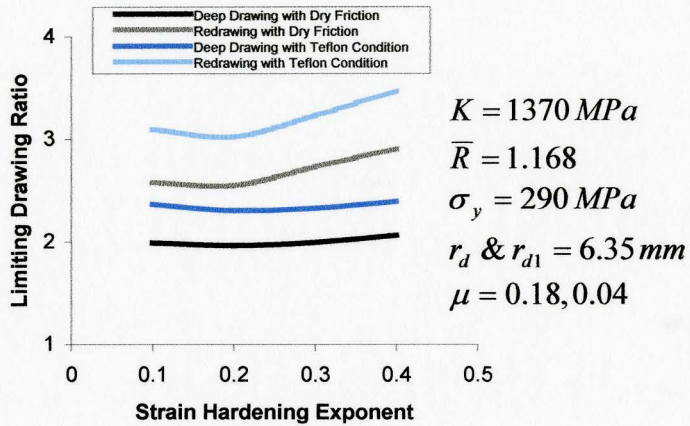


Figure 5.35 Effect of strain hardening factor on LDR

(2) Material normal anisotropy \bar{R}

Figure 5.36 shows that the LDRs of both deep drawing and redrawing operations are proportional to material normal anisotropy value \bar{R} . The meaning of \bar{R} can be understood as resistance to thinning of the material during the forming process. This explains why a material with a larger normal anisotropy value has a better drawability.

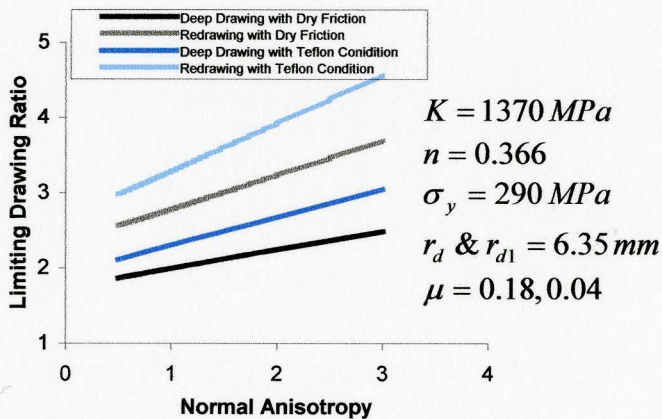


Figure 5.36 Effect of material normal anisotropy on LDR

(3) Material yield stress σ_y

Figure 5.37 shows that the LDRs of both drawing operations decrease linearly with an increasing in yield stress σ_y , because it requires larger drawing force to deform the blank plastically if the material has a larger yield stress value and larger drawing force will lead to an easier failure in the processes. The reason why the Teflon curves have a small decreasing slope than those of dry friction is because with less friction in the flange area, less drawing load is needed to form the cup so that material yield stress has a reduced effect.

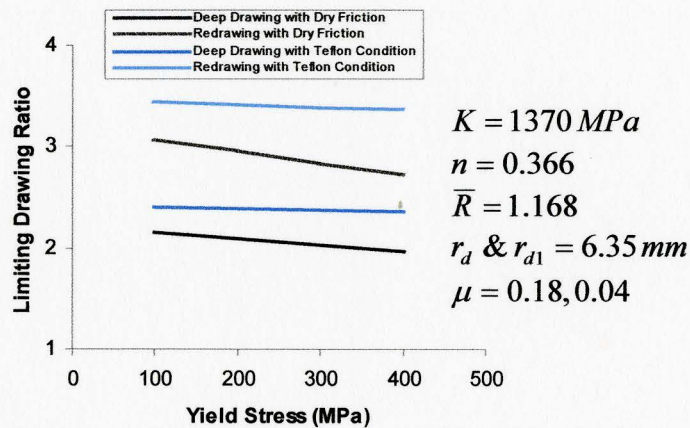


Figure 5.37 Effect of material yield stress on LDR

(4) Die corner radius r_d & r_{d1}

As shown in Figure 5.38, the LDR is proportional to die corner radius, because the material is easier to flow into the die with a larger arc radius. It is to be noted that for redrawing process in the figure, the data was plotted in the situation of assuming two dies involved in the processes having the same die corner radius. The reason why the curves

of the operation with one redrawing stage have a larger slope is because this parameter affects LDR in both the first and second draw, i.e. double effect.

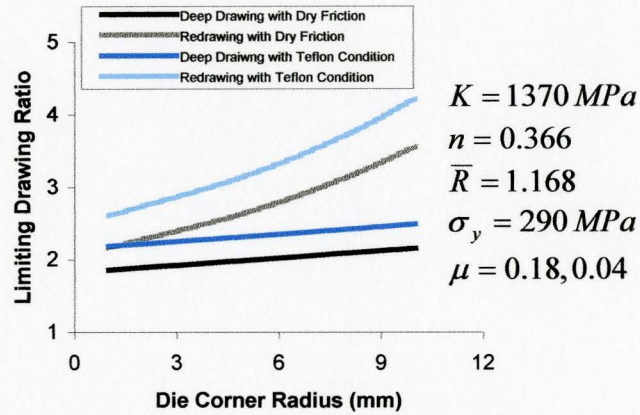


Figure 5.38 Effect of die corner radius on LDR

However, if the deep drawing and redrawing processes involves two dies with different die corner radii, additional calculation has to be made to obtain the response of this factor in terms of LDR, as shown in Table 5.11.

Table 5.11 LDRs of the process with one redrawing stage using dies with different radii

r_d (mm) \ r_{d1} (mm)	3	6	10
3	2.399	2.770	3.464
6	2.433	2.812	3.523
10	2.466	2.854	3.556

(5) Friction Coefficient μ

Figure 5.39 expresses a relationship between the LDR and friction coefficient μ in the flange area involved in the operations. It is obvious that the limiting drawing values decrease with increasing friction coefficient in the flange area. This is because larger friction means greater resisting force in the process so that the cup is easier to crack. The reason why LDR value decreases more rapidly for redrawing compared to deep drawing is exactly the same as in the case of die corner radius, i.e. double effect.

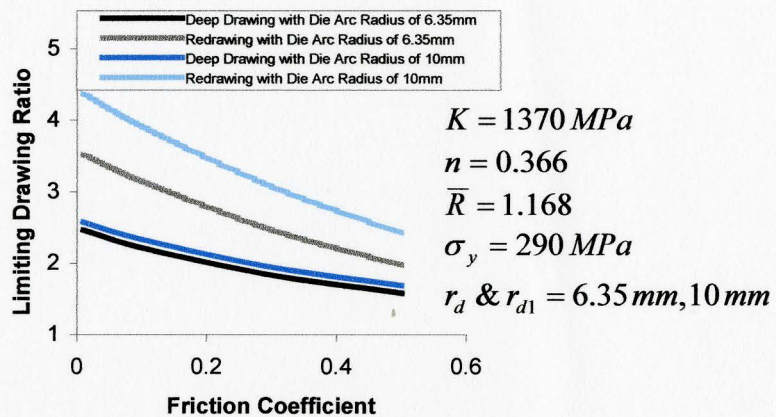


Figure 5.39 Effect of friction coefficient on LDR

It is to be noted that the parameter of punch profile radius was not included in the mathematical expression derived in Chapter 3, so the effect of this factor on LDR was not studied and plotted. However, it would not affect the final result drastically, because this parameter only has minor effect on LDR, as discussed in previous section. Table 5.12 summarizes the trends in LDR with respect to the parameters listed above.

Table 5.12 Effect of each parameter on limiting drawing ratio in drawing operations

Parameter situation	LDR of drawing operations
Material strain hardening factor n increasing	Decreasing and then increasing
Material normal anisotropy \bar{R} increasing	Increasing
Material yield stress σ_y increasing	Decreasing
Punch profile radius r_p	Minor effect
Die corner radius r_d & r_{d1} increasing	Increasing
Friction coefficient μ increasing	Decreasing

Chapter 6 Conclusions and Future Work

6.1 Conclusions

The present study has led to the following conclusions:

- (1) A new analytical model for redrawing process based on the extension of an existing mathematical model for deep drawing operation has been developed. The model has been validated by experimental and FE simulation work and the results are within reasonable error range. The new model provides a good interpretation and prediction of the role of material and tooling design parameter in drawing and redrawing. Furthermore, the effects of several parameters, such as n , \bar{R} , r_d and μ on LDR have been studied theoretically. The trends in LDR with respect to these parameters have been summarized in detail. The results are in good agreement with those existing in the literature.
- (2) A new finite element model for deep drawing has been developed, which accounts for the clamping force due to the inadequate stiffness of the operating machine. For

redrawing, the model takes stress and strain input from the deep drawing stage. The simulation results are in good agreement with the experimental work.

- (3) Argus optical strain measurement system has been utilized to obtain full-field strain measurement from the entire drawn and redrawn cup profiles for the first time to provide a rigorous validation of FE and analytical models.
- (4) Deep drawing with centre hole blank process has been studied experimentally and numerically in detail. The FE simulation model of the process has been compared to the experimental work in terms of punch load and clamping force versus punch displacements and thickness distributions along the product profiles and the results are in good agreement. In addition, the LDR values from blanks with different initial centre hole diameters have been determined by FE simulation work.
- (5) FE simulation has provided process signatures and strain paths during deep drawing and redrawing. These process signatures in conjunction with FLC provide useful insight into the material flow behaviors in deep drawing, redrawing and deep drawing with centre hole blank processes.

6.2 Future Work

6.2.1 Deep drawing process

Research on deep drawing process has been well developed in the previous work. In addition, this thesis work has improved FE simulation analysis in terms of clamping force due to inadequate machine stiffness. However, there is still some future work based on this process to improve the theoretical analysis, such as LDR prediction. For example, the effects of punch profile radius and punch-die clearance on LDR have not been included in the theoretical model due to the complexity of solving the mathematical expression. Theoretical-FE simulation combined method can be proposed to solve this problem, because FE model has been validated by experimental work with good agreements. Some correlation coefficients determined by FE analysis can be related to the mathematical formula to improve the accuracy of LDR prediction.

6.2.2 Redrawing process

The same improvement as deep drawing process can also be made on redrawing process. Furthermore, theoretical LDR prediction can be extended to multi-stage redrawing using the same method proposed in this thesis work, since only one redrawing stage has been involved in this research. Once again, the accuracy of LDR prediction can be improved by theoretical-FE simulation combined method.

6.2.3 Deep drawing process with centre hole blank

As mentioned in Chapter 5, this particular deep drawing process has not been investigated in detail. This thesis work has proposed a brief research method to develop further analysis on the process. Depending on the requirement of product profile, either a full drawn cup (Figure 6.1) or an “L” shape ring (Figure 6.2), the critical flanging ratios for these two cases need to be determined. Further studies on product profiles in terms of the amount of the centre hole expansion in the first case and the cup wall height in the second case are necessary. In addition, a mathematical model can also be proposed to predict the critical flanging ratios for these two cases and the results can be validated by experimental and FE simulation work.

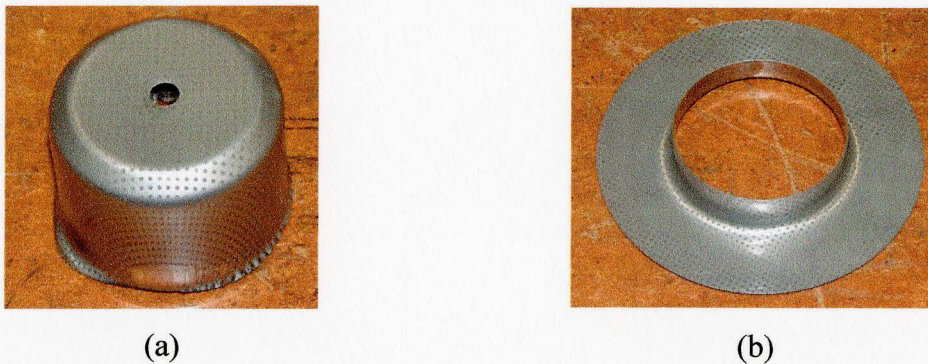


Figure 6.1 Two different product profiles from deep drawing with centre hole blanks: (a) full drawn cup and (b) “L” shape ring

References

- [1] Leu D.W., The limiting drawing ratio for plastic instability of the cup-drawing process, *Journal of Material Processing Technology*, V86, p168-176, 1999.
- [2] Swift H.W., An experimental investigation of deep drawing and redrawing cylindrical cups, *Process Int. Mech. Eng.* UK, p437-447, 1952.
- [3] Takeuchi K.; Kanamori H.; Ichikawa Y., On the scale effect in the cylindrical cup drawing of sheet aluminum on the limiting drawing ratio, *Japan Inst Light Metals-J*, V19, p550-8, 1969.
- [4] Woodthorpe J.; Pearce R., Effect of R and n upon the forming limit diagrams of sheet steel, *Sheet Metal Industry*, V46, p1061-7, 1969.
- [5] Chakrabarty J; Mellor P.B., New approach for predicting the limiting drawing ratio, *Met Ital*, V62, p791-9, 1970.
- [6] Kaftanoglu B, Method for estimating the limiting drawing ratio in deep-drawing, *International Journal of Production Research*, V12, p89-98, 1974.
- [7] Bayoumi M.R., Friction and bending effects on the limiting drawing ratios of anisotropic workhardening sheet metals, ASME Prod Eng Div Publ PED, p229-239, 1993.
- [8] Schedin E., Ph.D Thesis, Royal Institute of Technology, Stockholm, Sweden, 1991.
- [9] Hill R., The mathematical Theory of Plasticity, Clarendon Press, Oxford, UK, 1950.
- [10] Wan, M, Forming limit of conical parts in pressing, Ph.D. Dissertation, Harbin Institute of Technology, Harbin, 1995 (in Chinese).
- [11] Wan M.; Yang Y.Y.; Li S.B., Determination of fracture criteria during the deep drawing of conical cups, *Journal of Materials Processing Technology*, V114, p109-113, 2001.
- [12] Wan M.; Yang Y.Y.; Li S.B., Determination of the limiting drawing coefficient in the deep drawing of conical cups, *Journal of Materials Processing Technology*, V114, p114-117, 2001.

- [13] Whiteley R.L., The importance of directionality in drawing quality sheet steel, *Trans. ASM*, V52, p154, 1960.
- [14] Kawai N.; Hayashi N.; Matsui S., Assessment of deep-drawability of mild steel in consideration of r-value change during processing, *Journal of Engineering for Industry*, V110, p376-383, 1988.
- [15] Saran M.J.; Schedin E.; Samuelsson A.; Melander A.; Gustafsson C., Numerical and experimental investigations of deep drawing of metal sheets, *Journal of Engineering for Industry*, V112, p272-277, 1990.
- [16] Huang Y.M.; Chen J.W., Influence of the tool clearance in the cylindrical cup-drawing process, *Journal of Materials Processing Technology*, V57, p4-13, 1996.
- [17] Huang Y.M.; Chen J.W., Influence of lubricant on formability of cylindrical cup-drawing process, *Journal of Materials Processing Technology*, V63, p77-82, 1997.
- [18] Huang Y.M.; Chen J.W., Influence of the die arc on formability in the cylindrical cup-drawing process, *Journal of Materials Processing Technology*, V55, p350-369, 1995.
- [19] Moshksar M.M.; Zamanian A., Optimization of the tool geometry in the deep drawing of aluminum, *Journal of Materials Processing Technology*, V72, p363-370, 1997.
- [20] Zaky A.M.; Nassr A.B.; El-Sebaie M.G., Optimum blank shape of cylindrical cups in deep drawing of anisotropic sheet metals, *Journal of Materials Processing Technology*, V76, p203-211, 1998.
- [21] Jain M.; Allin J.; Bull M.J., Deep drawing characteristics of automotive aluminum alloys, *Materials Science and Engineering A*, V256, p69-82, 1998.
- [22] Kishor N.; Ravi Kumar D., Optimization of initial blank shape to minimize earing in deep drawing using finite element method, *Journal of Materials Processing Technology*, V130-131, p20-30, 2002.
- [23] Natarajan S.; Venkataswamy S.; Bagavathiperumal P., A note on deep drawing process: numerical simulation and experimental validation, *Journal of Materials Processing Technology*, V127, p64-67, 2002.
- [24] Colgan M; Monaghan J, Deep drawing process: analysis and experiment, *Journal of Material Processing Technology*, V132, p35-41, 2003.

- [25] Courant R (1888-1972), Ph.D. Georg-August-Universität Göttingen, 1910.
- [26] Gotoh M.; Ishise F., Finite element analysis of rigid-plastic deformation of the flange in a deep-drawing process based on a fourth-degree yield function, *International Journal of Mechanical Sciences*, V20, p423-435, 1978.
- [27] Onate E.; Zienkiewicz O.C., Viscous shell formulation for the analysis of thin sheet metal forming, *International Journal of Mechanical Sciences*, V25, p305-355, 1983.
- [28] Keck P.; Wilhelm M.; Lange K., Application of the finite element method to the simulation of the sheet forming process, comparison of calculations and experiments, *International Journal for Numerical Methods in Engineering*, V30, p1415-1430, 1990.
- [29] Wang C.T.; Wagonei R.H., Plane strain deep drawing: finite element modeling and measurements, *Autobody Stamping Technology Progress*, p133-142, 1991.
- [30] Sukhomlinov L.G.; Engelsberg V.K.; Davydov V.N., Finite element membrane model for the analysis of axisymmetric sheet metal forming processes, *International Journal of Mechanical Sciences*, V34, p179-193, 1992.
- [31] Harpell E.T.; Worswick M.J.; Finn M.; Jain M.; Martin P., Numerical prediction of the limiting draw ratio for aluminum alloy sheet, *Journal of materials processing technology*, V100, p131-141, 2000.
- [32] Menezes L.F.; Teodosiu C., Three-dimensional numerical simulation of the deep-drawing process using solid finite elements, *Journal of Materials Processing Technology*, V97, p100-106, 2000.
- [33] Kim J.B.; Yoon J.W.; Yang D.Y.; Barlat F., Investigation into wrinkling behavior in the elliptical cup deep drawing process by finite element analysis using bifurcation theory, *Journal of Materials Processing Technology*, V111, p170-174, 2001.
- [34] Liu Y.Q.; Wang J.C.; Hu P., Finite element analysis of the flange earrings of strong anisotropic sheet metals in deep-drawing processes, *Acta Mechanica Sinica/Lixue Xuebao*, V18, p82-91, 2002.
- [35] Erman Tekkaya A., State-of-the-art of simulation of sheet metal forming, *Journal of Materials Processing Technology*, V103, p14-22, 2000.

- [36] Duchene L; Habraken, A.M., Analysis of the sensitivity of FEM prediction to numerical parameters in deep drawing simulations, *European Journal of Mechanics A/Solids*, V24, p614-629, 2005.
- [37] MacPhee J., An engineering analysis of the redrawing process, *Sheet Metal Industry*, p427-440, 1976.
- [38] Iseki H.; Murota T.; Katoh K., On the determination of the redrawing ratio in the redrawing cylindrical shells with numerical simulation, *Nippon Kikai Gakkai Ronbunshu C Hen*, V52, p2257-2264, 1986.
- [39] Iseki H.; Murota T.; Katoh K., On the determination of the redrawing ratio in the redrawing cylindrical shells with a numerical simulation (2nd report, on the determination of the redrawing ratio by the reduction of the maximum deep drawing force), *Nippon Kikai Gakkai Ronbunshu C Hen*, V54, p2249-2256, 1988.
- [40] Iseki H.; Murota T.; Katoh K., On the determination of the redrawing ratio in the redrawing cylindrical shells with a numerical simulation (3rd report, on the determination of the redrawing ratio by the reduction of the maximum deep drawing energy), *Nippon Kikai Gakkai Ronbunshu C Hen*, V54, p3106-3114, 1988.
- [41] Iseki H.; Sowerby R., On the determination of the redrawing ratio in the redrawing cylindrical shells with a numerical simulation (on the determination of the redrawing ratio by the minimax optimization of compromise programming), *JSME International Journal*, V33, p202-208, 1990.
- [42] Parsa H.M.; Yamaguchi K.; Takakura N., Redrawing analysis of aluminum-stainless-steel laminated sheet using FEM simulations and experiments, *International Journal of Mechanical Sciences*, V43, p2331-2347, 2001.
- [43] Sonis P.; Venkata Reddy N.; Lai G.K., On Multistage deep drawing of axisymmetric components, *Journal of Manufacturing and Engineering*, V125, p352-362, 2003.
- [44] Marinkovic V., Analysis of hole-flanging process in stainless steel sheet, *Journal of Technology of Plasticity*, V26, p57-66, 2001.
- [45] Averkiev A.J.; Belov E.A. I dr.: Kovka I stampovka – Tom 4, Listovaja stampovka (Red. A.D.Matvejev). “Masinostroenie”, Moskva, 1987 (in Russian).

- [46] Ghosh, A.; Mallik, A.K., 1985, *Manufacturing Science*, Affiliated East-West Press Publishers Ltd., India.
- [47] Trilion Optical Test Systems, 2001 GOM mbH, Braunschweig, Germany.
- [48] Maker B.N.; Zhu X.H., Input parameter for metal forming simulation using LS-DYNA, Livermore Software Technology Corporation, 2000.
- [49] Andersson R.; Magnusson C.; Schedin E., Using stainless steel for energy absorbing components in automobiles
- [50] Hosford, W.F.; Caddell, R.M., 1983, *Metal Forming – Mechanics and Metallurgy*, Prentice Hall.

Appendices

Appendix A: Detailed Derivation of Daw-Kwei Leu's Work [1]

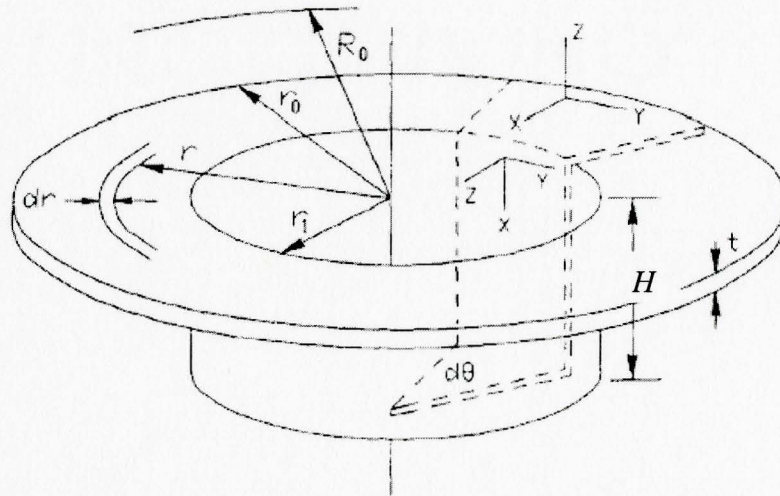


Figure AA.1 Schematic representation of a drawn cup showing the coordinate system and the dimensional notation [1]

Figure AA.1 shows the deep drawing operation under consideration that a circular sheet blank of original radius R_0 and thickness t_0 to be drawn by the flat-bottomed punch through a die opening of radius r_1 with a constant clearance blank holder.

In this model, Holloman's power law gives:

$$\bar{\sigma} = K\bar{\epsilon}^n \quad (\text{AA.1})$$

As discussed in Chapter 2, the normal anisotropy was evaluated as:

$$\bar{R} = \frac{R_{0^\circ} + 2R_{45^\circ} + R_{90^\circ}}{4} \quad (\text{AA.2})$$

Hill's quadratic anisotropic criterion and corresponding flow rule were utilized to describe the incremental theory of anisotropic plasticity as shown below:

$$\bar{\sigma} = \sqrt{\frac{1}{1+\bar{R}}} \left[(\sigma_\theta - \sigma_z)^2 + (\sigma_r - \sigma_z)^2 + \bar{R}(\sigma_r - \sigma_\theta)^2 \right]^{1/2} \quad (\text{AA.3})$$

$$d\bar{\varepsilon} = \frac{\sqrt{1+\bar{R}}}{1+2\bar{R}} \left[(d\varepsilon_\theta - \bar{R}d\varepsilon_z)^2 + (d\varepsilon_r - \bar{R}d\varepsilon_z)^2 + \bar{R}(d\varepsilon_r - d\varepsilon_\theta)^2 \right]^{1/2} \quad (\text{AA.4})$$

$$\begin{aligned} \frac{d\varepsilon_r}{\bar{R}(\sigma_r - \sigma_\theta) + (\sigma_r - \sigma_z)} &= \frac{d\varepsilon_\theta}{\bar{R}(\sigma_\theta - \sigma_r) + (\sigma_\theta - \sigma_z)} \\ &= \frac{d\varepsilon_z}{(\sigma_z - \sigma_\theta) + (\sigma_z - \sigma_r)} = \frac{d\bar{\varepsilon}}{(1+\bar{R})\bar{\sigma}} \end{aligned} \quad (\text{AA.5})$$

(1) Cup Wall Region

Critical drawing force at a certain stage:

$$P_c = 2\pi r_1 t \sigma_r \quad (\text{AA.6})$$

where $\varepsilon_z = \ln\left(\frac{t}{t_0}\right) \Rightarrow t = t_0 e^{\varepsilon_z}$

In this region:

$$\begin{aligned} d\varepsilon_\theta &= 0 \\ \Rightarrow d\varepsilon_r &= -d\varepsilon_z \\ d\varepsilon_r + d\varepsilon_\theta + d\varepsilon_z &= 0 \end{aligned} \quad (\text{AA.7})$$

Substitute Equation (AA.7) into Equation (AA.4):

$$\begin{aligned} \bar{\varepsilon} &= \frac{\sqrt{1+\bar{R}}}{1+2\bar{R}} \left[\bar{R}^2 \varepsilon_z^2 + (1+\bar{R})\varepsilon_z^2 + \bar{R}\varepsilon_z^2 \right]^{1/2} \\ &= \frac{\sqrt{1+\bar{R}}}{1+2\bar{R}} (2\bar{R}^2 + 3\bar{R} + 1)^{1/2} (-\varepsilon_z) \\ &= -\frac{1+\bar{R}}{\sqrt{1+2\bar{R}}} \varepsilon_z \end{aligned}$$

$$\Rightarrow \varepsilon_z = -\frac{\sqrt{1+2\bar{R}}}{1+\bar{R}} \bar{\varepsilon} \quad (\text{AA.8})$$

Substitute Equation (AA.8) into Equation (AA.5):

$$\begin{aligned} \frac{\varepsilon_z}{-(\sigma_\theta + \sigma_r)} &= \frac{\bar{\varepsilon}}{(1+\bar{R})\bar{\sigma}} \\ \Rightarrow \frac{\frac{\sqrt{1+2\bar{R}}}{1+\bar{R}} \bar{\varepsilon}}{\sigma_\theta + \sigma_r} &= \frac{\bar{\varepsilon}}{(1+\bar{R})\bar{\sigma}} \\ \Rightarrow \sigma_\theta &= \sqrt{1+2\bar{R}}\bar{\sigma} - \sigma_r \end{aligned} \quad (\text{AA.9})$$

Substitute Equation (AA.9) into Equation (AA.3):

$$\begin{aligned} \bar{\sigma} &= \sqrt{\frac{1}{1+\bar{R}} \left[\left(\sqrt{1+2\bar{R}}\bar{\sigma} - \sigma_r \right)^2 + \sigma_r^2 + \bar{R} \left(2\sigma_r - \sqrt{1+2\bar{R}}\bar{\sigma} \right)^2 \right]^{1/2}} \\ \Rightarrow \sigma_r^2 - \sqrt{1+\bar{R}}\bar{\sigma}\sigma_r + \frac{\bar{R}(1+\bar{R})}{1+2\bar{R}}\bar{\sigma}^2 &= 0 \\ \Rightarrow \sigma_r &= \frac{1+\bar{R}}{\sqrt{1+2\bar{R}}}\bar{\sigma} \\ \Rightarrow \sigma_r &= \frac{1+\bar{R}}{\sqrt{1+2\bar{R}}}\bar{\varepsilon}^n \end{aligned} \quad (\text{AA.10})$$

Critical drawing force at limiting drawing condition can be achieved by maximizing the punch load at the beginning of the punch nose radius in the cup wall. The critical effective strain can be evaluated as:

$$\bar{\varepsilon} = \frac{1+\bar{R}}{\sqrt{1+2\bar{R}}} n \quad (\text{AA.11})$$

Substitute Equation (AA.10) and (AA.11) into Equation (AA.6):

$$P_c = 2\pi r_1 t_0 \left(\frac{1 + \bar{R}}{\sqrt{1 + 2\bar{R}}} \right) (n^n e^{-n} K) \quad (\text{AA.12})$$

(2) Die Arc Region

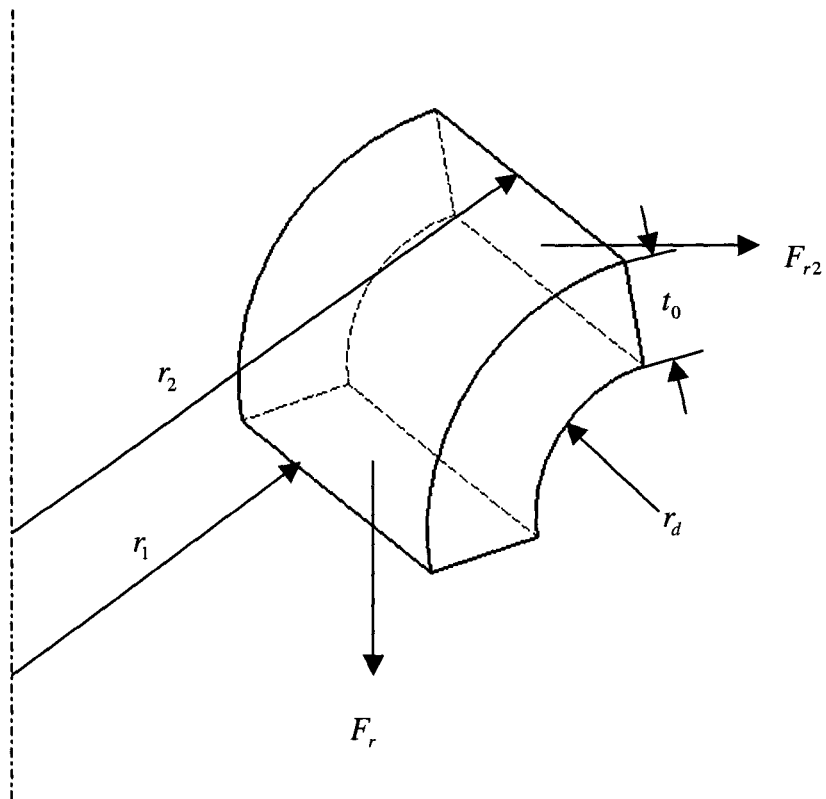


Figure AA.2 Free body diagram of die arc region

From the free body diagram in die arc region, as shown in Figure AA.2, the critical drawing stress at the top part of cup wall area σ_{r2} can be obtained by the equation below,

based on the force equilibrium and the increase in rope tension around a capstan with friction between radii r_1 and $r_2 = r_1 + r_d$ [46]:

$$\frac{F_r}{F_{r_2}} = e^{\frac{\mu\pi}{2}} \Rightarrow F_{r_2} = F_r e^{-\frac{\mu\pi}{2}}$$

$$\Rightarrow \sigma_{r_2} = \frac{P_{r_2}}{2\pi r_2 t_0} = \frac{P_c}{2\pi r_2 t_0} e^{-\frac{\mu\pi}{2}} \quad (\text{AA.13})$$

Substitute Equation (AA.12) into Equation (AA.13):

$$\sigma_{r_2} = \left(\frac{1 + \bar{R}}{\sqrt{1 + 2\bar{R}}} \right)^{1+n} (n^n e^{-n} K) e^{-\frac{\mu\pi}{2}} \left(\frac{r_1}{r_2} \right) \quad (\text{AA.14})$$

(3) Flange Region

Radial equilibrium of the element in this region gives:

$$\frac{d\sigma_r}{dr} + \frac{\sigma_r - \sigma_\theta}{r} + \frac{2\mu Q}{t_0} = 0 \quad (\text{AA.15})$$

Q in the equation above represents the clamping force in the operation and neglecting the effect of this parameter, the equation becomes:

$$\frac{d\sigma_r}{dr} = -\frac{\sigma_r - \sigma_\theta}{r} \quad (\text{AA.16})$$

In this region:

$$d\varepsilon_z = 0$$

$$d\varepsilon_r + d\varepsilon_\theta + d\varepsilon_z = 0 \quad \Rightarrow d\varepsilon_r = -d\varepsilon_\theta \quad (\text{AA.17})$$

Substitute Equation (AA.17) into Equation (AA.4):

$$\begin{aligned}
\bar{\varepsilon} &= \frac{\sqrt{1+\bar{R}}}{1+2\bar{R}} \left(\varepsilon_\theta^2 + \varepsilon_\theta^2 + 4\bar{R}\varepsilon_\theta^2 \right)^{1/2} \\
&= \frac{\sqrt{1+\bar{R}}}{1+2\bar{R}} (4\bar{R}+2)^{1/2} \varepsilon_\theta \\
&= \sqrt{\frac{2(1+\bar{R})}{1+2\bar{R}}} \varepsilon_\theta \\
&\Rightarrow \varepsilon_\theta = \sqrt{\frac{1+2\bar{R}}{2(1+\bar{R})}} \bar{\varepsilon}
\end{aligned} \tag{AA.18}$$

Substitute Equation (AA.18) into Equation (AA.5):

$$\begin{aligned}
\frac{\varepsilon_\theta}{\bar{R}(\sigma_\theta - \sigma_r) + \sigma_\theta} &= \frac{\bar{\varepsilon}}{(1+\bar{R})\bar{\sigma}} \\
\Rightarrow \frac{-\sqrt{\frac{1+2\bar{R}}{2(1+\bar{R})}} \bar{\varepsilon}}{(1+\bar{R})\sigma_\theta - \bar{R}\sigma_r} &= \frac{\bar{\varepsilon}}{(1+\bar{R})\bar{\sigma}} \\
\Rightarrow \sigma_\theta &= -\sqrt{\frac{1+2\bar{R}}{2(1+\bar{R})}} \bar{\sigma} + \frac{\bar{R}}{1+\bar{R}} \sigma_r
\end{aligned} \tag{AA.19}$$

Substitute Equation (AA.19) into Equation (AA.3):

$$\begin{aligned}
\bar{\sigma} &= \sqrt{\frac{1}{1+\bar{R}}} \left[\left(-\sqrt{\frac{1+2\bar{R}}{2(1+\bar{R})}} \bar{\sigma} + \frac{\bar{R}}{1+\bar{R}} \sigma_r \right)^2 + \sigma_r^2 \right]^{1/2} \\
&\quad + \bar{R} \left(\sqrt{\frac{1+2\bar{R}}{2(1+\bar{R})}} \bar{\sigma} + \frac{1}{1+\bar{R}} \sigma_r \right)^2 \\
\Rightarrow \frac{1+2\bar{R}}{1+\bar{R}} \sigma_r^2 - \frac{1}{2} \bar{\sigma}^2 &= 0
\end{aligned}$$

$$\Rightarrow \sigma_r = \sqrt{\frac{1+\bar{R}}{2(1+2\bar{R})}} \bar{\sigma}$$

$$\Rightarrow \sigma_r - \sigma_\theta = \sqrt{\frac{2(1+\bar{R})}{1+2\bar{R}}} \bar{\sigma} \quad (\text{AA.20})$$

In flange region:

$$\varepsilon_\theta = \ln\left(\frac{R}{r}\right) \quad (\text{AA.21})$$

Substitute Equation (AA.21) into Equation (AA.18):

$$\bar{\varepsilon} = \sqrt{\frac{2(1+\bar{R})}{1+2\bar{R}}} \ln\left(\frac{R}{r}\right)$$

$$\Rightarrow \bar{\sigma} = K \left[\sqrt{\frac{2(1+\bar{R})}{1+2\bar{R}}} \ln\left(\frac{R}{r}\right) \right]^n \quad (\text{AA.22})$$

Substitute Equation (AA.22) into Equation (AA.20)

$$\sigma_r - \sigma_\theta = K \left[\sqrt{\frac{2(1+\bar{R})}{1+2\bar{R}}} \right]^{n+1} \left[\ln\left(\frac{R}{r}\right) \right]^n \quad (\text{AA.23})$$

Substitute Equation (AA.23) into Equation (AA.16):

$$\int_{\sigma_{r1}}^{\sigma_{r2}} d\sigma_r = -K \left[\sqrt{\frac{2(1+\bar{R})}{1+2\bar{R}}} \right]^{n+1} \int_0^2 \left[\ln\left(\frac{R}{r}\right) \right]^n \frac{dr}{r}$$

$$\Rightarrow \sigma_{r2} = \sigma_{r0} + K \left[\sqrt{\frac{2(1+\bar{R})}{1+2\bar{R}}} \right]^{n+1} \int_2^0 \left[\ln\left(\frac{R}{r}\right) \right]^n \frac{dr}{r} \quad (\text{AA.24})$$

where σ_{r0} is the radial friction stress at position r_0 . This value is approximated as

$$2\mu(1.1\sigma_y) \frac{R_0}{r_0}.$$

(4) Solving Limiting Drawing Ratio

The limiting drawing ratio can be determined by solving the integral in Equation (AA.24)

and the value of σ_{r_2} obtained in Equation (AA.14) and

$\sigma_{r_0} = 2\mu(1.1\sigma_y)\frac{R_0}{r_0}$. The detailed solving procedures of the integral were shown below:

$$\begin{aligned} \frac{R}{r} \leq 3 &\Rightarrow \ln\left(\frac{R}{r}\right) \leq 2 \\ \Rightarrow \int_2^6 \left[\ln\left(\frac{R}{r}\right) \right]^n \frac{dr}{r} &= \int_2^6 \left\{ 1 + \left[\ln\left(\frac{R}{r}\right) - 1 \right] \right\}^n \frac{dr}{r} \\ &\approx \int_2^6 \left\{ 1 + n \left[\ln\left(\frac{R}{r}\right) - 1 \right] \right\} \frac{dr}{r} \\ &= \int_2^6 \ln\left(\frac{R}{r}\right) \frac{dr}{r} + (1-n) \ln\left(\frac{r_0}{r_2}\right) \end{aligned} \quad (\text{AA.25})$$

The integral term in Equation (AA.25) can be approximated as:

$$\begin{aligned} \int_2^6 \ln\left(\frac{R}{r}\right) \frac{dr}{r} &\approx \int_2^6 2 \left(\frac{\frac{R}{r} - 1}{\frac{R}{r} + 1} \right) \frac{dr}{r} \\ &= 2 \int_2^6 \left(1 - \frac{2r}{R+r} \right) \frac{dr}{r} \\ &= 2 \ln\left(\frac{r_0}{r_2}\right) - 4 \int_2^6 \frac{1}{R+r} dr \end{aligned} \quad (\text{AA.26})$$

According to the volume constancy of plastic deformation in the flange region:

$$R_0^2 - r_0^2 = R^2 - r^2 = R_2^2 - r_2^2 = C^2 = \text{Constant} \quad (\text{AA.27})$$

Equation (AA.26) can be written as:

$$\begin{aligned}
\int_2^0 \ln\left(\frac{R}{r}\right) \frac{dr}{r} &= 2 \ln\left(\frac{r_0}{r_2}\right) - \frac{4}{C^2} \int_2^0 (R-r) dr \\
&= 2 \ln\left(\frac{r_0}{r_2}\right) - \frac{4}{C^2} \left(\int_2^0 \sqrt{C^2 + r^2} dr - \frac{r_0^2 - r_2^2}{2} \right) \\
&= 2 \left[\ln\left(\frac{r_0}{r_2}\right) - \frac{1}{C^2} \left(R_0 r_0 - R_2^2 r_2^2 + C^2 \ln \frac{R_0 + r_0}{R_2 + r_2} - r_0^2 + r_2^2 \right) \right] \tag{AA.28}
\end{aligned}$$

Substitute Equation (AA.28) into Equation (AA.25):

$$\int_2^0 \left[\ln\left(\frac{R}{r}\right) \right]^n \frac{dr}{r} = (1+n) \ln \frac{r_0}{r_2} - 2n \left(\ln \frac{R_0 + r_0}{R_2 + r_2} + \frac{r_0}{R_0 + r_0} - \frac{r_2}{R_2 + r_2} \right) \tag{AA.29}$$

Substitute Equation (AA.14) and (AA.29) into Equation (AA.24):

$$\begin{aligned}
f(LDR_0) &= -C_1 \frac{r_1}{r_2} + C_3 \frac{LDR_0 r_1}{\sqrt{(LDR_0)^2 - R_2^2 + r_2^2}} \\
&+ C_2 (1+n) \ln \left(\sqrt{\frac{LDR_0^2 r_1^2}{r_2^2} - \frac{R_2^2}{r_2^2} + 1} \right) \\
&- 2nC_2 \ln \left(\frac{LDR_0 r_1}{r_2} + \sqrt{\frac{LDR_0^2 r_1^2}{r_2^2} - \frac{R_2^2}{r_2^2} + 1} \right) \tag{AA.30} \\
&- 2nC_2 \frac{1}{\frac{LDR_0 r_1}{\sqrt{LDR_0^2 r_1^2 - R_2^2 + r_2^2}} + 1} + 2nC_2 \left(\ln \left(\frac{R_2}{r_2} + 1 \right) + \frac{1}{\frac{R_2}{r_2} + 1} \right) = 0
\end{aligned}$$

where:

$$C_1 = \left(\frac{1 + \bar{R}}{\sqrt{1 + 2\bar{R}}} \right)^{1+n} (n^n e^{-n} K) e^{-\frac{\mu\pi}{2}}$$

$$C_2 = K \left(\sqrt{\frac{2(1 + \bar{R})}{2\bar{R} + 1}} \right)^{1+n}$$

$$C_3 = 2\mu(1.1\sigma_y)$$

Due to constancy of volume, the term $\frac{R_2}{r_2}$ can be evaluated:

$$\begin{aligned} \pi(R_2^2 - R_1^2)t_0 &= 2\pi \left(r_2 - \frac{2r_d}{\pi} \right) \frac{\pi r_d t_0}{2} \\ \Rightarrow \frac{R_2}{r_2} &= \sqrt{\pi \left(\frac{r_d}{r_2} - \frac{2r_d^2}{\pi r_2^2} \right) + \left(\frac{r_1}{r_2} \right)^2 \left(\frac{R_1}{r_1} \right)^2} \end{aligned} \quad (\text{AA.31})$$

Because the effective strain in the flange never exceeds the critical strain in the cup wall area, the term $\frac{R_1}{r_1}$ can be approximated as:

$$\begin{aligned} \bar{\epsilon} &= \sqrt{\frac{2(1 + \bar{R})}{1 + 2\bar{R}}} \ln \left(\frac{R_1}{r_1} \right) = \frac{1 + \bar{R}}{\sqrt{1 + 2\bar{R}}} n \\ \Rightarrow \frac{R_1}{r_1} &= e^{\sqrt{\frac{1 + \bar{R}}{2}} n} \end{aligned} \quad (\text{AA.32})$$

It is to be noticed that r_2 appeared in Equation (AA.30) instead of R_0 , which means that the theoretical maximum blank diameter can be determined by this equation based on the punch diameter. However, if R_0 is utilized in the equation, one would find the

critical designed punch diameter, because $LDR = \frac{R_0}{r_1}$ and $r_1 = r_2 - r_d$. By using some

iteration method, such as Newton-Raphson method, Equation (AA.30) can be solved.

Appendix B: Detailed Derivation of Wang's Conical Cup Model [10-12]

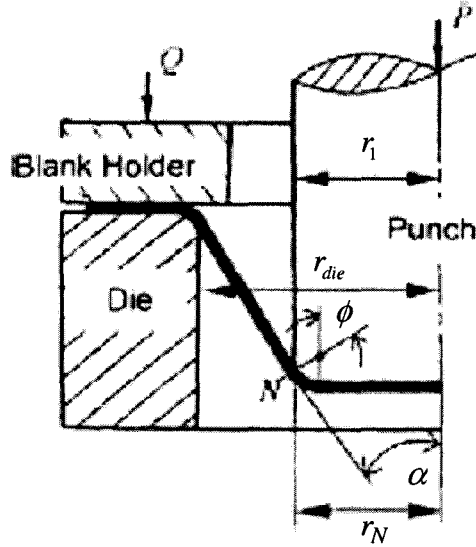


Figure AB.1 Illustration of a conical cup drawing [12]

Figure AB.1 shows a cross section illustration of a conical cup drawing process with a punch radius of r_1 and die radius of r_{die} . Holloman's strain-hardening expression, Equation (2.2) and Hill's anisotropic yield criterion, Equation (2.4-2.6) are also utilized in this model. After the arrangement, some expressions are obtained:

$$\sigma_{\theta} - \sigma_t = \bar{R}(\sigma_r - \sigma_{\theta}) \quad (\text{AB.1})$$

$$\sigma_r - \sigma_t = (1 + \bar{R})(\sigma_r - \sigma_{\theta}) \quad (\text{AB.2})$$

$$\bar{\sigma} = \sqrt{1 + 2\bar{R}}(1 - \beta)\sigma_r \quad (\text{AB.3})$$

where the stress ratio $\beta = \frac{\sigma_{\theta}}{\sigma_r}$.

The strain increment is:

$$d\bar{\epsilon} = \frac{1 + \bar{R}}{\sqrt{1 + 2\bar{R}}} d\epsilon_r \quad (\text{AB.4})$$

In order to describe accurately the stress state on the critical section, the influence of the thickness stress σ_z on the acting surface of a blank with a punch profile is considered, as shown in Figure AB.2.

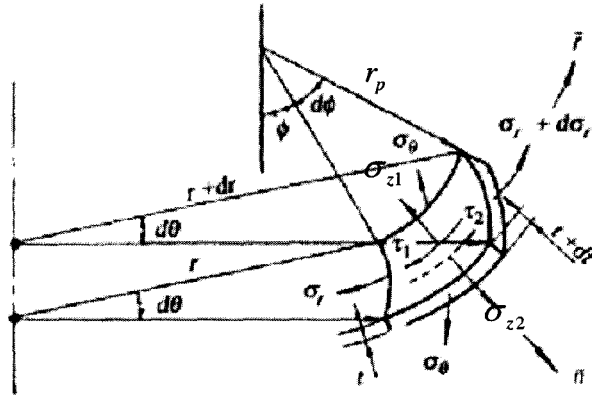


Figure AB.2 Stress state on the critical section [11]

By simplifying the normal equilibrium equation, the following equation is obtained:

$$\frac{\sigma_{z2} - \sigma_{z1}}{t} = \frac{\sigma_{\theta} \sin \phi}{r} + \frac{\sigma_r}{r_p'} \quad (\text{AB.5})$$

and r_N in Figure AB.1 can be written as:

$$r_N = r_1 - r_p + r_p' \sin \phi = r_1 - r_p + \left(r_p + \frac{1}{2} t \right) \cos \alpha \quad (\text{AB.6})$$

where: $r_{p'} = r_p + \frac{1}{2}t$

With $\sigma_{z2} = 0$ and $\sigma_{z1} = \sigma_z$, Equation (AB.3) can be re-written as:

$$\sigma_z = -\frac{t}{r_N r_{p'}} (\sigma_\theta r_{p'} \cos \alpha + \sigma_r r_N) \quad (\text{AB.7})$$

Substitute Equation (AB.7) into Equation (AB.1):

$$\left(1 + \bar{R} + \frac{t}{r_N} \cos \alpha\right) \sigma_\theta = \left(\bar{R} - \frac{t}{r_{p'}}\right) \sigma_r \quad (\text{AB.8})$$

Based on Equation (AB.8), the stress ratio β can be expressed as:

$$\beta = \frac{\sigma_\theta}{\sigma_r} = \frac{\bar{R} - \frac{t}{r_{p'}}}{1 + \bar{R} + \frac{t \cos \alpha}{r_N}} \quad (\text{AB.9})$$

Substituting Equation (AB.9) into Equation (AB.3), the radial stress is evaluated as:

$$\sigma_r = \frac{1 + \bar{R} + \frac{t \cos \alpha}{r_N}}{\sqrt{1 + \bar{R}} \left(1 + \frac{t \cos \alpha}{r_N} + \frac{t}{r_{p'}}\right)} \bar{\sigma} \quad (\text{AB.10})$$

Using the same approach as Leu's work, the critical effective strain in the process can be obtained as:

$$\bar{\varepsilon} = \frac{1 + \bar{R}}{\sqrt{1 + 2\bar{R}}} n \quad (\text{AB.11})$$

And the thickness at certain stage can be expressed as:

$$t = t_0 e^{-n} \quad (\text{AB.12})$$

By substituting Equation (AB.11, AB.12) and using Holloman's expression, the critical stress σ^* can be derived as:

$$\sigma_c = \frac{1 + \bar{R}}{\sqrt{1 + 2\bar{R}}} \frac{1 + \bar{R} + \frac{t_0 e^{-n} \cos \alpha}{r_N}}{(1 + \bar{R}) \left(1 + \frac{t_0 e^{-n} \cos \alpha}{r_N} + \frac{t_0 e^{-n}}{r_p'} \right)} K \left(\frac{1 + \bar{R}}{\sqrt{1 + 2\bar{R}}} \right)^n n^n \quad (\text{AB.13})$$

When necking occurs in uniaxial tensile test, the power law can be written as:

$$\sigma_j = K \varepsilon_j^n \text{ and } \sigma_j = \frac{d\sigma_j}{d\varepsilon_j} \quad (\text{AB.14})$$

With necking strain $\varepsilon_j = n$, the necking stress is determined as:

Substitute Equation (AB.15) into Holloman's expression:

$$K = \frac{\sigma_j}{\varepsilon_j^n} = \sigma_{UTS} \left(\frac{e}{n} \right)^n \quad (\text{AB.16})$$

Finally, with the substitution of Equation (AB.16) into Equation (AB.13), the critical stress can be determined as:

$$\sigma_c = C \left(\frac{1 + \bar{R}}{\sqrt{1 + 2\bar{R}}} \right)^{1+n} e^n \sigma_{UTS} \quad (\text{AB.17})$$

where:

$$C = \frac{1}{1 + \bar{R}} \frac{1 + \bar{R} + \frac{t_0 e^{-n} \cos \alpha}{r_1 - r_p + \left(r_p + \frac{1}{2} t_0 e^{-n}\right) \cos \alpha}}{1 + \frac{t_0 e^{-n} \cos \alpha}{r_1 - r_p + \left(r_p + \frac{1}{2} t_0 e^{-n}\right) \cos \alpha + \frac{t_0 e^{-n}}{r_p + \frac{1}{2} t_0 e^{-n}}}}$$

From Figure AB.2, the critical load P^* in the deep drawing process can be determined as:

$$P_c = 2\pi \left[r_1 - r_p + \left(r_p + \frac{1}{2} t_0 e^{-n} \cos \alpha \right) \right] t_0 e^{-n} \sigma_c \cos \alpha \quad (\text{AB.18})$$

A mathematical representation of the limiting drawing ratio, $LDR = \frac{R_0}{r_{die}}$ was obtained, as shown below, where σ_{rN} is the radial stress at Point N in Figure AB.1. In addition, they found that when $\frac{r_0}{R_0} \approx 0.9$, σ_{rN} reaches a maximum value in the whole

process and it can be written as:

$$\sigma_{rN \max} = \frac{r_{die}}{r_1} \left[\left(\frac{\mu Q}{2.83 R_0 t} + 1.1 \bar{\sigma} \ln(0.9 LDR) \right) e^{\mu \phi} + \frac{t \sigma_{UTS}}{2(r_{die} + 0.5t)} \right] \quad (\text{AB.19})$$

where the effective stress $\bar{\sigma}$ can be expressed by:

$$\bar{\sigma} = \sigma_{UTS} \left(\frac{e}{n} \right)^n \left[\frac{1}{2} \ln \frac{0.9}{LDR} \sqrt{0.19 + \frac{1}{LDR^2}} \right]^n$$

By equating Equation (AB.17) and Equation (AB.19), it is possible to solve the limiting drawing ratio numerically using iteration method.

Appendix C: Effect of Numerical Parameters on FE results

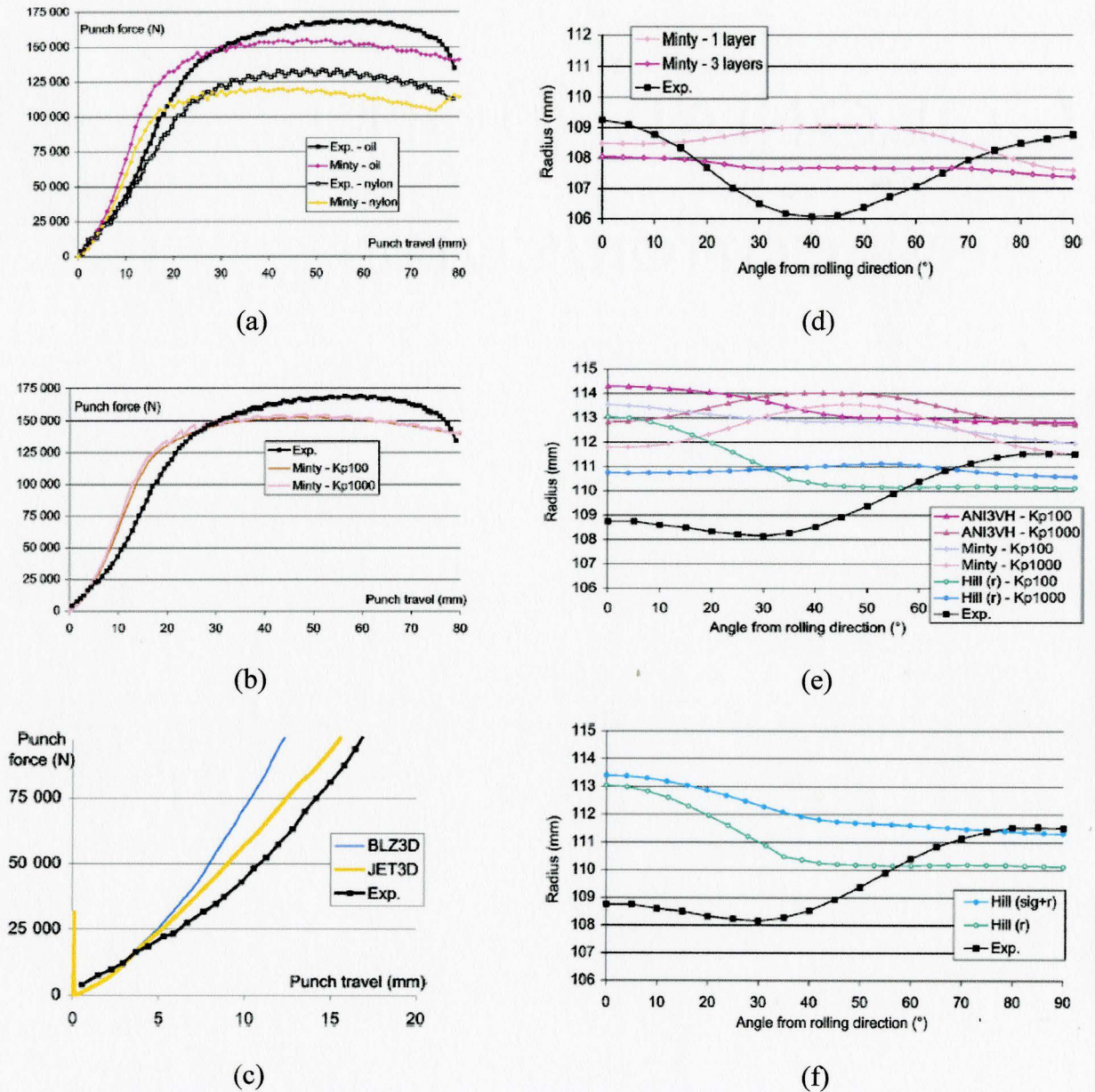


Figure AD.1 Punch forces as a function of punch displacement showing the effect of (a) lubricant, (b) penalty factor and (c) element type, and earing radius as a function of angle from rolling direction with effect of (d) element layer, (e) penalty factor and (f) element type [36]

Appendix D: Detailed Derivation of Iseki's Work [38-41]

Notation:

- R_0, R_n : Radius of initial blank and mean radius of a cup wall at the n th redrawing process
- t : Thickness of initial blank
- β_n, β_{nm} : Redrawing ratio ($= R_{n-1} / R_n$) and the limiting redrawing ratio at the n th redrawing process
- β_{nt} : Total drawing ratio ($= R_0 / R_n$) up to n th redraw
- β_{na} : Redrawing ratio calculated by maximization of the minimum safety factor
- β_{np} : Redrawing ratio calculated by minimization of the maximum drawing force
- β_{ne} : Redrawing ratio calculated by minimization of the maximum drawing energy
- β_{ni} : Redrawing ratio calculated by the minimax optimization of compromise programming
- φ_n, φ_L : Contact angles of the initial and last stages at the bell surface of the die profile
- η_n : Ratio of the die radius ρ_n of the bell of die to the cup wall radius R_n
- μ_n : Coulomb's coefficient of friction at the n th redraw
- P_n, S_n, W_n : Drawing force, punch stroke and redrawing energy at the n th redraw
- P_{nk}, S_{nk}, W_{nk} : Drawing force, punch stroke and redrawing energy at step k of the n th redraw
- H_n, p_n : Blank holder load and mean pressure of blank holder
- σ_{φ_n} : Stress in the meridian direction at the die radius
- σ_{en} : Yield stress at n th redraw
- σ_p : Plane strain tensile strength
- α_n : Safety factor ($\sigma_p / \sigma_{\varphi_n}$)

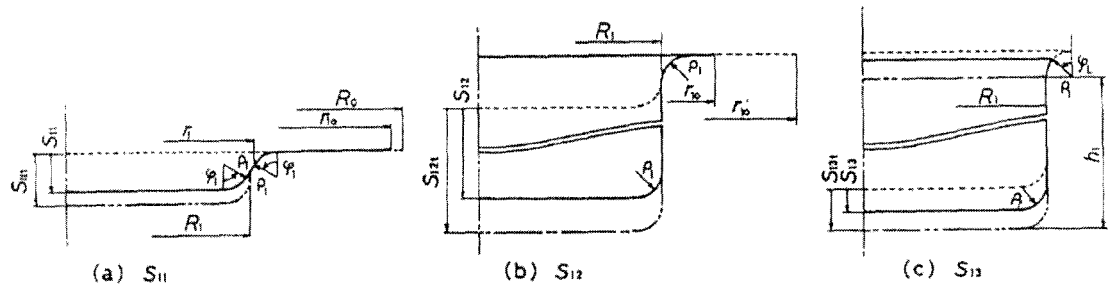


Figure AD.1 k step stroke S_{1k} during the first draw [41]

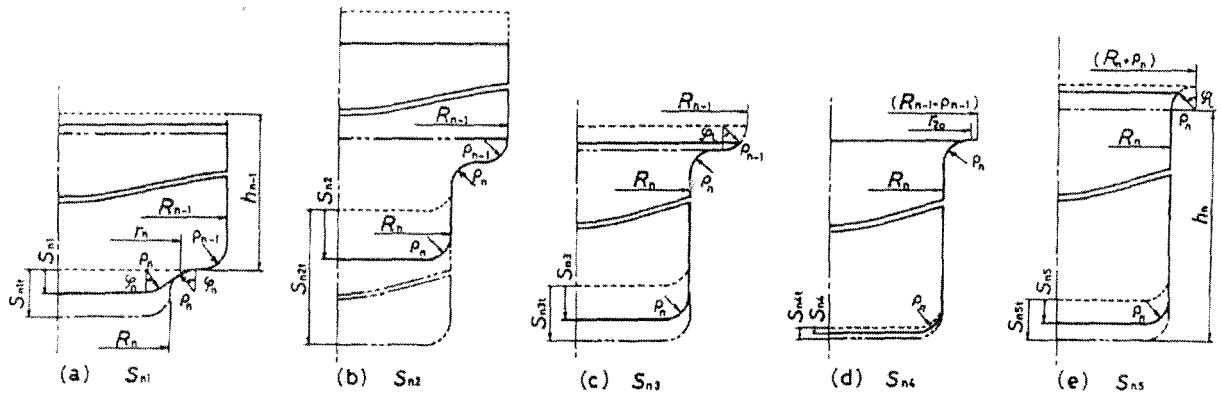


Figure AD.2 k step stroke S_{nk} at the n th draw [41]

Figure AD.1 shows specific stages, designated S_{1k} during the initial draw and Figure AD.2 shows the stroke S_{nk} at some intermediate stage k during n th redraw. Expressions for the meridian stress σ_{φ_n} at die radius, the drawing force P_{nk} , and the redrawing energy W_{nk} were given below:

(1) The first draw

$$\sigma_{\phi 1} = e^{\frac{\pi\mu_1}{2}} \left(\sigma_{e1} \ln \frac{r_{10}}{R_1} + \frac{\mu_1 H_1}{\pi r_{10} t} \right) + \left(1 + e^{\frac{\pi\mu_1}{2}} \right) \frac{t}{4\rho_1} \sigma_{e1} \quad (\text{AD.1})$$

$$P_{12} = 2\pi R_1 t \sigma_{\phi 1} \quad (\text{AD.2})$$

$$W_{12} = \int_0^{\phi_{12}} P_{12} dS_{12} \quad (\text{AD.3})$$

(2) The n th redraw

$$\sigma_{\phi n} = \sigma_{en} \left\{ e^{\frac{\pi\mu_n}{2}} \left[\ln \beta_n + \left(1 + e^{\frac{\pi\mu_n}{2}} \right) \frac{1}{4\rho_{n-1}} \right] + \left(1 + e^{\frac{\pi\mu_n}{2}} \right) \frac{1}{4\rho_n} \right\} + e^{\frac{\pi\mu_n}{2}} \frac{\mu_n H_n}{\pi(R_{n-1} - \rho_{n-1})t} \quad (\text{AD.4})$$

$$P_{12} = 2\pi R_n t \sigma_{\phi n} \quad (\text{AD.5})$$

$$W_{12} = \int_0^{\phi_{n2}} P_{n2} dS_{n2} \quad (\text{AD.6})$$

The total drawing ratio β_{nt} was determined from:

$$\beta_{nt} = \frac{R_0}{R_n} = \sqrt{1 + 2\frac{h}{R} - (4 - \pi)\frac{\rho}{R} - (\pi - 3)\frac{\rho^2}{R^2}} \quad (\text{AD.7})$$

where:

R = Drawn cup radius

h = Drawn depth

ρ = Punch nose radius

R_0 = Initial blank radius

In order to select the best solution of the multi-objective optimization problem, which consists of several objective functions ψ_i , a compromise solution was proposed. The ideal point is an optimum solution ψ_{iu} of each simple-objective function ψ_i . Defining $\beta = (\beta_1, \beta_2, \dots, \beta_n)$, the ideal solution ψ_{iu} was expressed as follows:

- (1) Maximization of the minimum safety factor $\alpha_{n\min}$ (max $\alpha_{n\min}$ method) [38]

$$\psi_1(\beta) = \alpha_{n\min}(\beta) \quad (\text{AD.8})$$

$$\psi_{1u} = \max \psi_1(\beta) \quad (\text{AD.9})$$

- (2) Minimization of the maximum drawing force $P_{n\max}$ (min $P_{n\max}$ method) [39]

$$\psi_2(\beta) = P_{n\max}(\beta) \quad (\text{AD.10})$$

$$\psi_{2u} = \min \psi_2(\beta) \quad (\text{AD.11})$$

- (3) Minimization of maximum drawing energy $W_{n\max}$ (min $W_{n\max}$ method) [40]

$$\psi_3(\beta) = W_{n\max}(\beta) \quad (\text{AD.12})$$

$$\psi_{3u} = \min \psi_3(\beta) \quad (\text{AD.13})$$

As there is not a characteristic of commensuration in the simple-objective function ψ_i , the non-attainment value of Ψ_i was defined by the standardization of the distance between an ideal solution ψ_{iu} and a simple-objective function ψ_i .

$$\Psi_1(\beta) = (\psi_{1u} - \psi_1(\beta)) / \psi_{1u} \quad (\text{AD.14})$$

$$\Psi_2(\beta) = (\psi_2(\beta) - \psi_{2u}) / \psi_{2u} \quad (\text{AD.15})$$

$$\Psi_3(\beta) = (\psi_3(\beta) - \psi_{3u}) / \psi_{3u} \quad (\text{AD.16})$$

Finally, the optimization problem was solved using a direct-search method based on the iterative test of trial solutions that satisfy the above equations.

Appendix E: Detailed Calculation to Solve Equation (3.8, 3.9)

The term $\left[\ln\left(\frac{R_0}{r_1}\right) + \sqrt{\frac{2(1+\bar{R})}{1+2\bar{R}}} \ln\left(\frac{R}{r}\right) \right]^n$ in the integral in Equation (3.8) can be

rearranged as:

$$\begin{aligned} & \left[\ln\left(\frac{R_0}{r_1}\right) + \sqrt{\frac{2(1+\bar{R})}{1+2\bar{R}}} \ln\left(\frac{R}{r}\right) \right]^n \\ &= \left(\sqrt{\frac{2(1+\bar{R})}{1+2\bar{R}}} \right)^n \left\{ \ln \left[\left(\frac{R}{r}\right) \left(\frac{R_0}{r_1}\right)^{\sqrt{\frac{1+2\bar{R}}{2(1+\bar{R})}}} \right] \right\}^n \end{aligned} \quad (\text{AE.1})$$

Usually, with the following relationships:

$$\begin{aligned} \frac{R}{r} &\leq 3 \\ \frac{R_0}{r_1} &< 6 \\ \sqrt{\frac{1+2\bar{R}}{2(1+\bar{R})}} &< 1 \end{aligned} \quad \Rightarrow \ln \left[\left(\frac{R}{r}\right) \left(\frac{R_0}{r_1}\right)^{\sqrt{\frac{1+2\bar{R}}{2(1+\bar{R})}}} \right] < 3$$

The equation can be rewritten as:

$$\begin{aligned} & \left(\sqrt{\frac{2(1+\bar{R})}{1+2\bar{R}}} \right)^n \left\{ 2 + \ln \left[\left(\frac{R}{r}\right) \left(\frac{R_0}{r_1}\right)^{\sqrt{\frac{1+2\bar{R}}{2(1+\bar{R})}}} \right] - 2 \right\}^n \\ &= 2^n \left(\sqrt{\frac{2(1+\bar{R})}{1+2\bar{R}}} \right)^n \left\{ 1 + \left(\frac{1}{2} \ln \left[\left(\frac{R}{r}\right) \left(\frac{R_0}{r_1}\right)^{\sqrt{\frac{1+2\bar{R}}{2(1+\bar{R})}}} \right] - 1 \right) \right\}^n \\ &\approx 2^n \left(\sqrt{\frac{2(1+\bar{R})}{1+2\bar{R}}} \right)^n \left\{ 1 + \frac{n}{2} \ln \left[\left(\frac{R}{r}\right) \left(\frac{R_0}{r_1}\right)^{\sqrt{\frac{1+2\bar{R}}{2(1+\bar{R})}}} \right] - n \right\} \end{aligned} \quad (\text{AE.2})$$

Substituting Equation (AB.2) into Equation (3.8), the integral in Equation (3.8) becomes:

$$\begin{aligned}
& \left[1 - n + \frac{n}{2} \sqrt{\frac{1+2\bar{R}}{2(1+\bar{R})}} \ln\left(\frac{R_0}{r_1}\right) \right] \int_{r_{21}}^{r_{01}} \frac{dr}{r} + \frac{n}{2} \int_{r_{21}}^{r_{01}} \ln\left(\frac{R}{r}\right) \frac{dr}{r} \\
&= \left[1 - n + \frac{n}{2} \sqrt{\frac{1+2\bar{R}}{2(1+\bar{R})}} \ln\left(\frac{R_0}{r_1}\right) \right] \ln\left(\frac{r_{01}}{r_{21}}\right) - n \left(\ln \frac{r_1 + r_{01}}{R_{21} + r_{21}} + \frac{r_{01}}{r_1 + r_{01}} - \frac{r_{21}}{R_{21} + r_{21}} \right) \\
& \left[1 - n + \frac{n}{2} \sqrt{\frac{1+2\bar{R}}{2(1+\bar{R})}} \ln\left(\frac{R_0}{r_1}\right) \right] \ln\left(\frac{r_{01}}{r_{21}}\right) \\
&= \left[\begin{aligned} & -n \ln\left(\frac{r_1 + r_{01}}{r_{21} + r_{21}}\right) - \ln\left(\frac{R_{21}}{r_{21}} + 1\right) + \frac{1}{\frac{r_1}{r_{01}} + 1} - \frac{1}{\frac{R_{21}}{r_{21}} + 1} \end{aligned} \right] \tag{AE.3}
\end{aligned}$$

Finally, Equation (3.9) can be obtained by multiplying Equation (AB.3) by a the factor of

$$K \sqrt{\frac{2(1+\bar{R})}{1+2\bar{R}}} \text{ and using the relationship of } r_1 = LDR_1 r_{11}.$$

Appendix F: Detailed Derivation of LDR_0 with Critical Effective Strain

$$\text{Value of } \bar{\varepsilon} = \frac{1 + \bar{R}}{\sqrt{1 + 2\bar{R}}} n - \ln\left(\frac{r_1}{r_{11}}\right)$$

(1) Cup Wall Region

As discussed in Chapter 3, the critical effective strain can only reach a value of

$$\bar{\varepsilon} = \frac{1 + \bar{R}}{\sqrt{1 + 2\bar{R}}} n - \ln\left(\frac{r_1}{r_{11}}\right) = \frac{1 + \bar{R}}{\sqrt{1 + 2\bar{R}}} n - \ln(LDR_1), \text{ so the critical drawing load } P_c \text{ in cup}$$

wall area is defined as:

$$P_c = 2\pi r_1 t_0 e^{\left[\frac{\sqrt{1+2\bar{R}}}{1+\bar{R}} \ln(LDR_1) - n\right]} K \frac{1 + \bar{R}}{\sqrt{1 + 2\bar{R}}} \left[\frac{1 + \bar{R}}{\sqrt{1 + 2\bar{R}}} n - \ln(LDR_1) \right]^n \quad (\text{AF.1})$$

(2) Die Corner Region

The maximum radial stress σ_{r2} can be expressed as:

$$\sigma_{r2} = \frac{1 + \bar{R}}{\sqrt{1 + 2\bar{R}}} \left[\frac{1 + \bar{R}}{\sqrt{1 + 2\bar{R}}} n - \ln(LDR_1) \right]^n e^{\left[\frac{\sqrt{1+2\bar{R}}}{1+\bar{R}} \ln(LDR_1) - n\right]} K \left(\frac{r_1}{r_2}\right) e^{\frac{\mu\pi}{2}} \quad (\text{AF.2})$$

(3) Flange Region

During the deep drawing process, the effective strain in the flange region can be written as:

$$\bar{\varepsilon} = \sqrt{\frac{2(1 + \bar{R})}{1 + 2\bar{R}}} \ln\left(\frac{R}{r}\right) \quad (\text{AF.3})$$

Hollomon's power law then gives:

$$\bar{\sigma} = K \left[\sqrt{\frac{2(1 + \bar{R})}{1 + 2\bar{R}}} \ln\left(\frac{R}{r}\right) \right]^n \quad (\text{AF.4})$$

From Hill's anisotropic theory, one obtains:

$$\sigma_r - \sigma_\theta = K \left(\sqrt{\frac{2(1+\bar{R})}{1+2\bar{R}}} \right)^{n+1} \left[\ln \left(\frac{R}{r} \right) \right]^n \quad (\text{AF.5})$$

Substitution of Equation (AC.5) into Equation (3.6) results in the integral below:

$$\int_{\sigma_0}^{\sigma_2} d\sigma_r = -K \left(\sqrt{\frac{2(1+\bar{R})}{1+2\bar{R}}} \right)^{n+1} \int_0^{\sigma_2} \left(\ln \frac{R}{r} \right)^n \frac{dr}{r} \quad (\text{AF.6})$$

The above equation can be written as:

$$\sigma_{r_2} = \sigma_{r_0} + K \left(\sqrt{\frac{2(1+\bar{R})}{1+2\bar{R}}} \right)^{n+1} \int_{\sigma_2}^0 \left(\ln \frac{R}{r} \right)^n \frac{dr}{r} \quad (\text{AF.7})$$

where $\sigma_{r_0} = 2\mu(1.1\sigma_y) \frac{R_0}{r_0}$.

Finally, by relating Equation (AC.2) to Equation (AC.7) and solving the integral, a function of limiting drawing ratio of deep drawing process $f(LDR_0)$ similar to Equation (2.10) can be achieved:

$$\begin{aligned}
f(LDR_0) &= -C_1' \frac{r_1}{r_2} + C_3 \frac{LDR_0 r_1}{\sqrt{LDR_0^2 r_1^2 - R_2^2 + r_2^2}} \\
&+ C_2 (1+n) \ln \left(\sqrt{\frac{LDR_0^2 r_1^2}{r_2^2} - \frac{R_2^2}{r_2^2} + 1} \right) \\
&- 2nC_2 \ln \left(\frac{LDR_0 r_1}{r_2} + \sqrt{\frac{LDR_0^2 r_1^2}{r_2^2} - \frac{R_2^2}{r_2^2} + 1} \right) - 2nC_2 \frac{1}{\frac{LDR_0 r_1}{\sqrt{LDR_0^2 r_1^2 - R_2^2 + r_2^2}} + 1} \quad (\text{AF.8}) \\
&+ 2nC_2 \left[\ln \left(\frac{R_2}{r_2} + 1 \right) + \frac{1}{\frac{R_2}{r_2} + 1} \right] = 0
\end{aligned}$$

where:

$$C_1' = \frac{1+\bar{R}}{\sqrt{1+2\bar{R}}} \left[\frac{1+\bar{R}}{\sqrt{1+2\bar{R}}} n - \ln(LDR_1) \right]^n e^{\left[\frac{\sqrt{1+2\bar{R}}}{1+\bar{R}} \ln(LDR_1) - n \right]} K e^{-\frac{\mu\pi}{2}}$$

$$C_2 = K \left(\sqrt{\frac{2(1+\bar{R})}{1+2\bar{R}}} \right)^{n+1}$$

$$C_3 = 2\mu(1.1\sigma_y)$$

Same as before, due to the constancy of volume, the term $\frac{R_2}{r_2}$ can be written as:

$$\begin{aligned}
\pi(R_2^2 - R_1^2) t_0 &= 2\pi \left(r_2 - \frac{2r_d}{\pi} \right) \frac{\pi r_d t_0}{2} \\
\Rightarrow \frac{R_2}{r_2} &= \sqrt{\pi \left(\frac{r_d}{r_2} - \frac{2r_d^2}{\pi r_2^2} \right) + \left(\frac{r_1}{r_2} \right)^2 \left(\frac{R_1}{r_1} \right)^2} \quad (\text{AF.9})
\end{aligned}$$

For the same reason of that the effective strain in the flange area never exceeds the

critical effective strain in the cup wall, term $\frac{R_1}{r_1}$ can be expressed as:

$$\bar{\epsilon} = \sqrt{\frac{2(1+\bar{R})}{1+2\bar{R}}} \ln\left(\frac{R_1}{r_1}\right) = \frac{1+\bar{R}}{\sqrt{1+2\bar{R}}} n - \ln(LDR_1)$$

$$\Rightarrow \frac{R_1}{r_1} = e^{\sqrt{\frac{1+\bar{R}}{2}} n - \sqrt{\frac{1+2\bar{R}}{2(1+\bar{R})}} \ln(LDR_1)} \quad (\text{AF.10})$$

R_1 and R_2 are the intermediate radii of annular rings at the blank, which draw into the die to radii r_1 and r_2 .

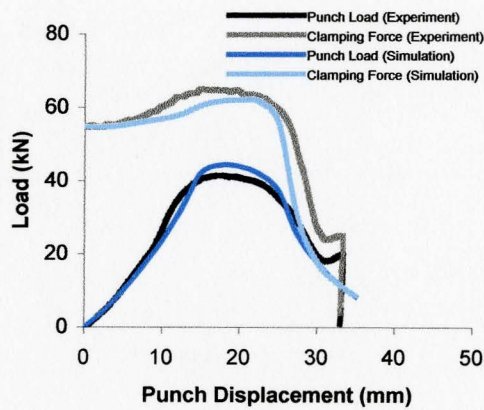
Appendix G: Comparison of Experimental and Simulation Results

1. Deep Drawing Process

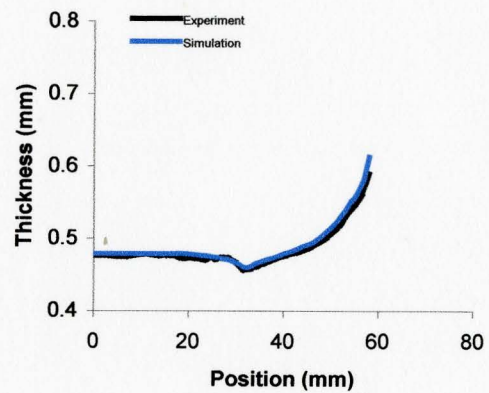
(1) Dry friction

Table AG.1 Experimental and simulation comparison of cup depth in deep drawing process with dry friction condition from different initial blank sheet sizes

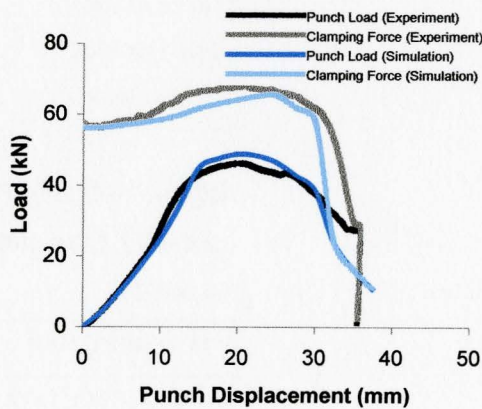
Initial blank size (mm)	95	100	105	110
Experiment cup height (mm)	29.59	33.84	38.43	43.13
Simulation cup height (mm)	30.27	34.49	39.08	43.35



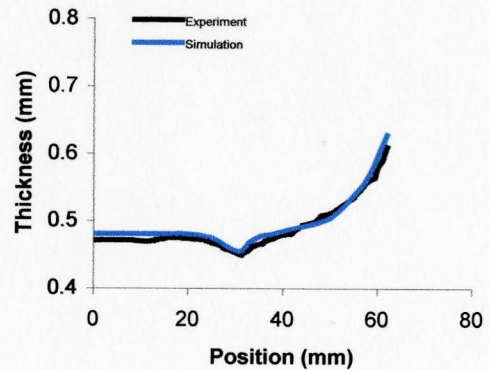
(a1)



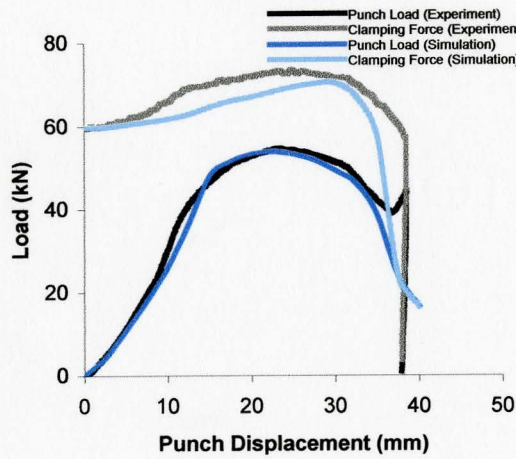
(a2)



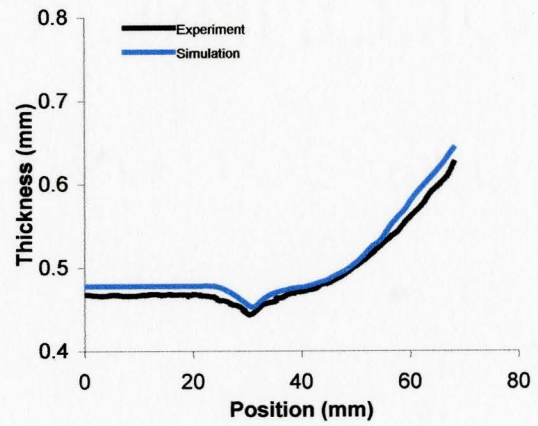
(b1)



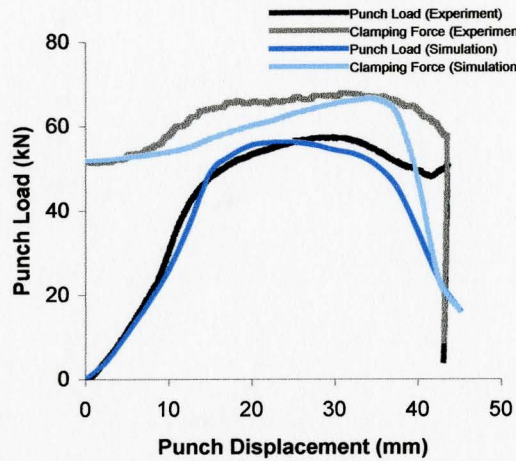
(b2)



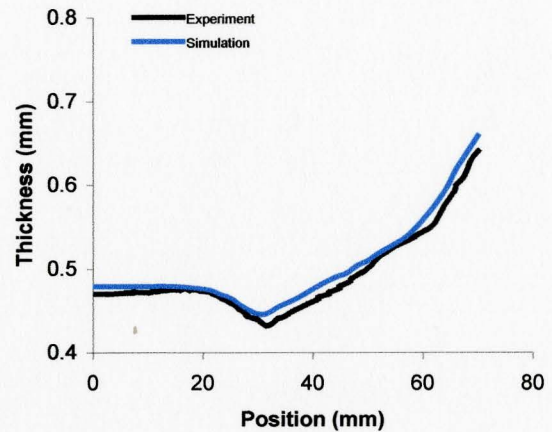
(c1)



(c2)



(d1)



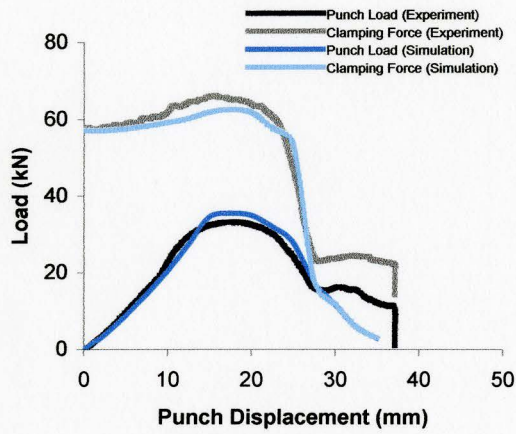
(d2)

Figure AG.1 Experimental and simulation results comparison of deep drawing process with dry friction condition: (a1)-(d1) punch load and clamping force versus punch displacements and (a2)-(d2) thickness distributions along the cup profiles from 95 mm – 110 mm initial blank diameters respectively

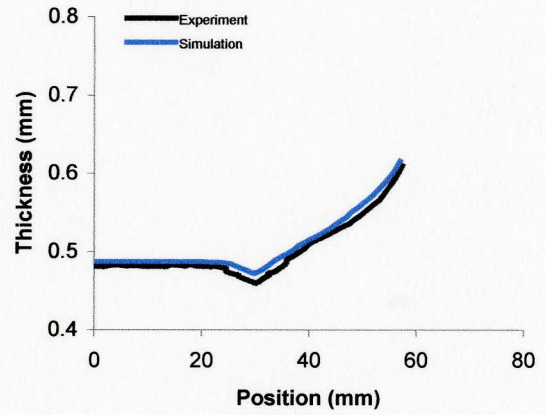
(2) Teflon condition

Table AG.2 Experimental and simulation comparison of cup depth in deep drawing process with Teflon friction condition from different initial blank sheet sizes

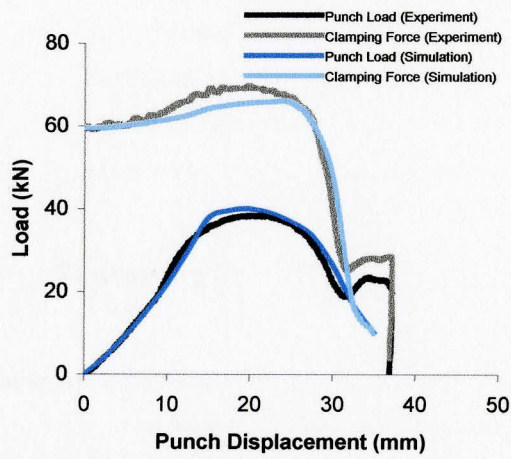
Initial blank size (mm)	95	100	105	110
Experiment cup height (mm)	28.92	33.96	38.03	42.66
Simulation cup height (mm)	29.58	34.33	38.44	42.87



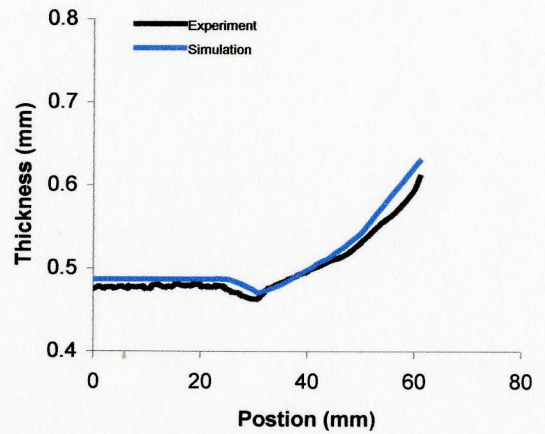
(a1)



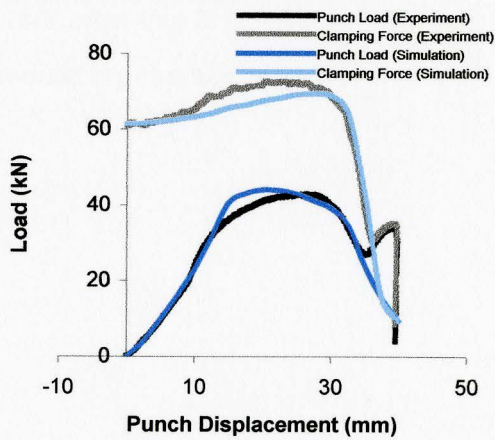
(a2)



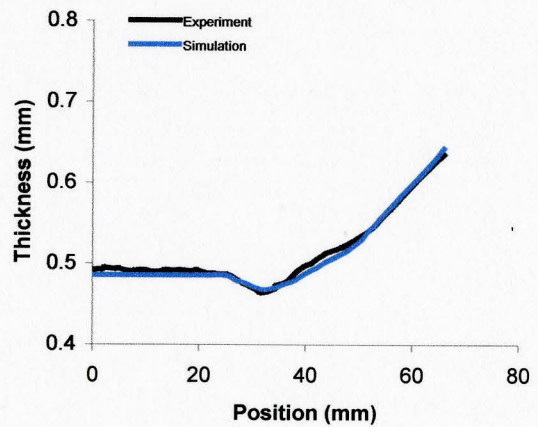
(b1)



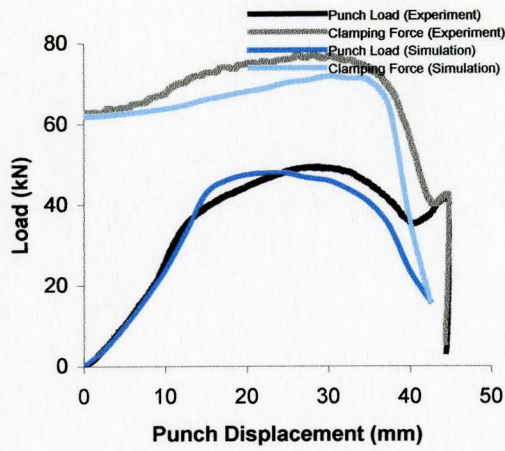
(b2)



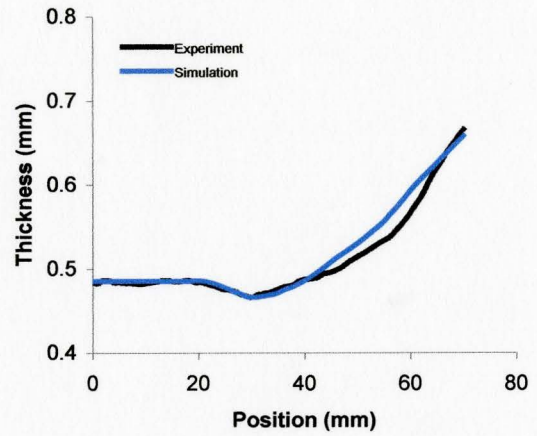
(c1)



(c2)



(d1)



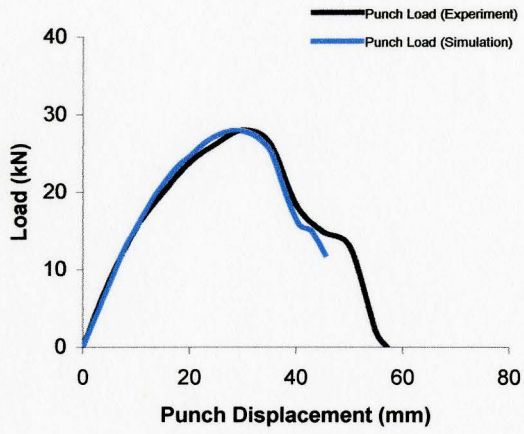
(d2)

Figure AG.2 Experimental and simulation results comparison of deep drawing process with Teflon friction condition: (a1)-(d1) punch load and clamping force versus punch displacements and (a2)-(d2) thickness distributions along the cup profiles from 95 mm – 110 mm initial blank diameters respectively

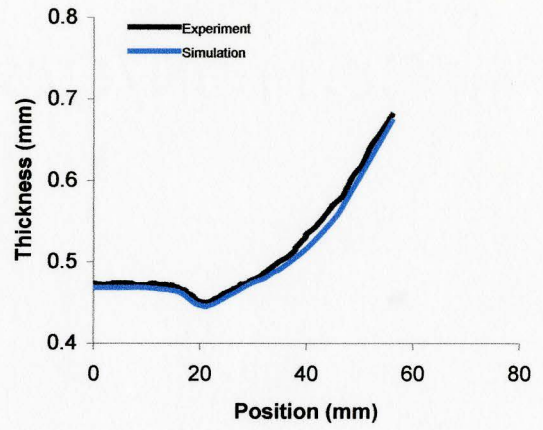
2. Redrawing Process

Table AG.3 Experimental and simulation comparison of cup depth in redrawing process with dry friction condition from different initial former drawn cup heights

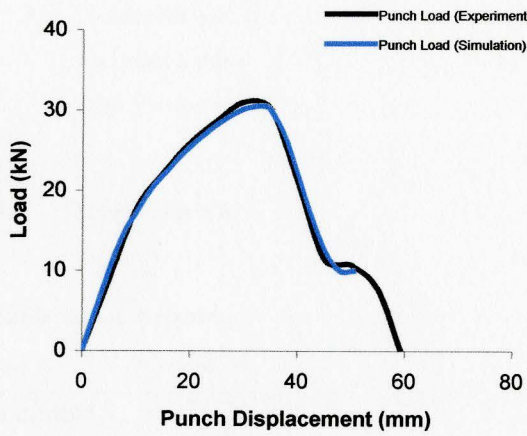
Initial blank size (mm)	95	100	105	110
Experiment cup height (mm)	35.13	40.11	45.42	51.46
Simulation cup height (mm)	35.57	40.68	45.65	51.41



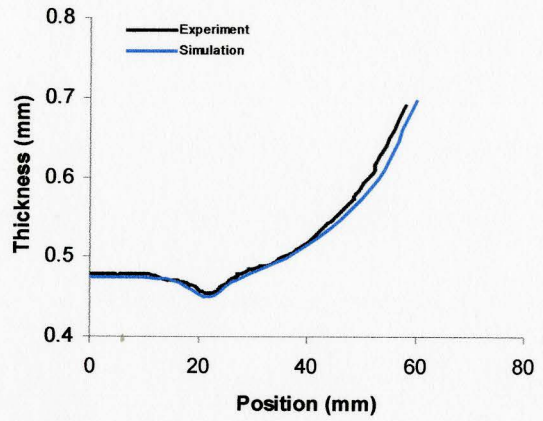
(a1)



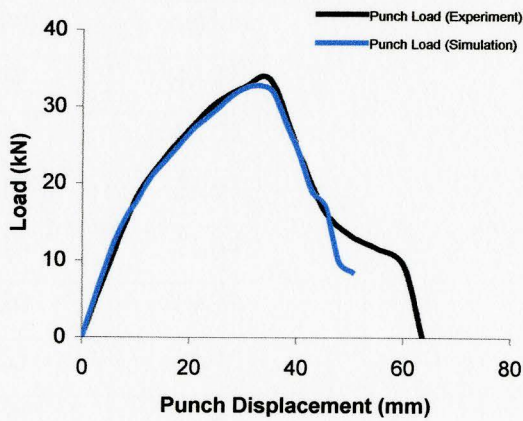
(a2)



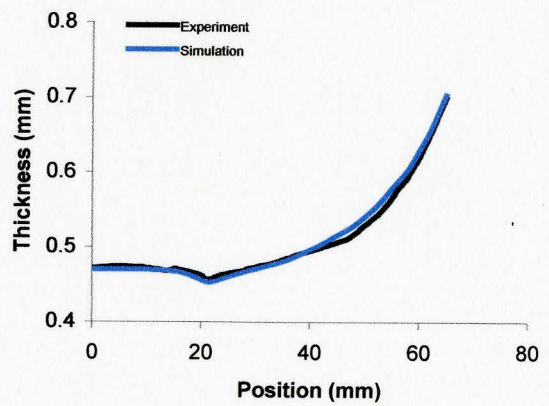
(b1)



(b2)



(c1)



(c2)

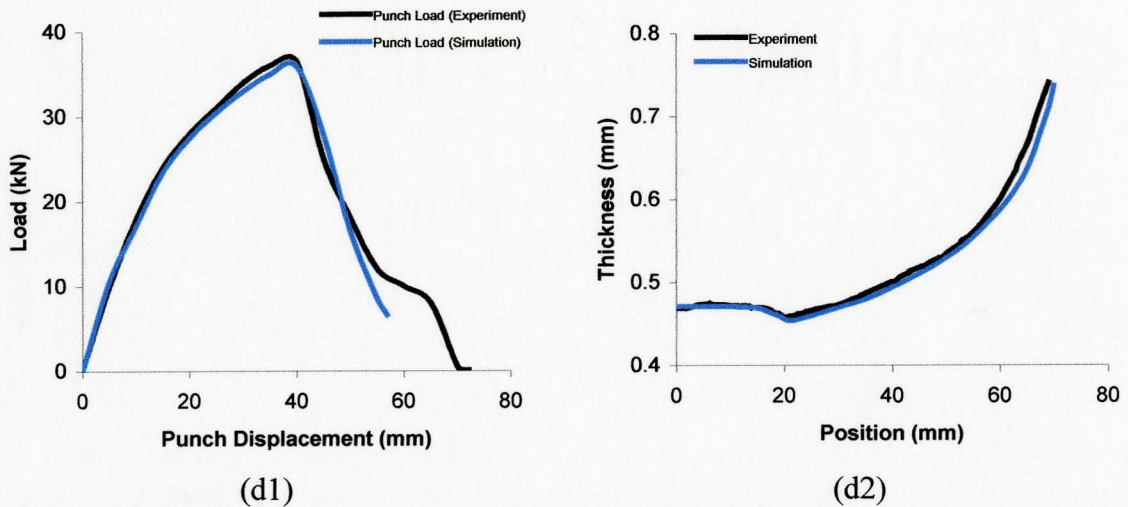
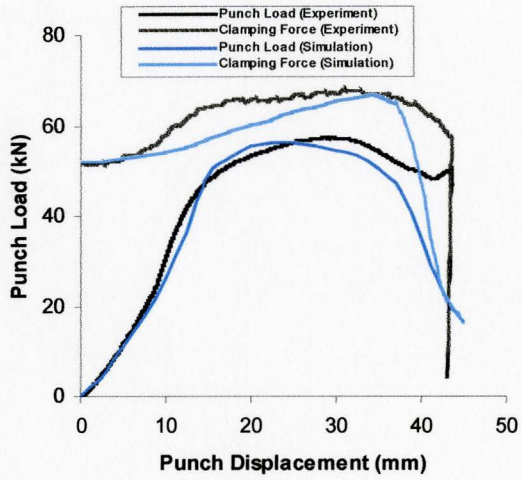


Figure AG.3 Experimental and simulation results comparison of redrawing process with dry friction condition: (a1)-(d1) punch load and clamping force versus punch displacements and (a2)-(d2) thickness distribution along the cup profiles from 95 mm – 110 mm initial blank diameter receptively

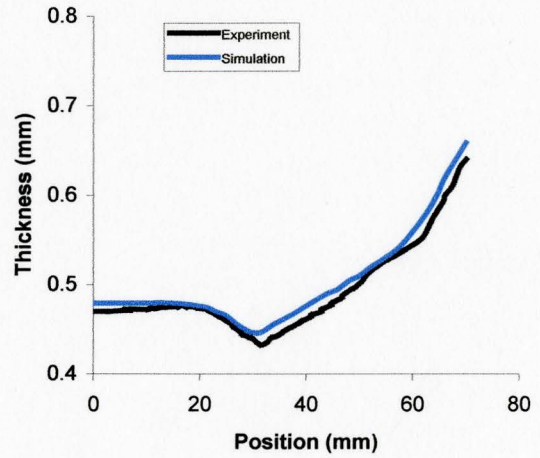
3. Deep Drawing With Centre Hole Blank Process

Table AG.4 Experimental and simulation comparison of cup profiles in deep drawing with centre hole blank process from different initial centre hole diameters

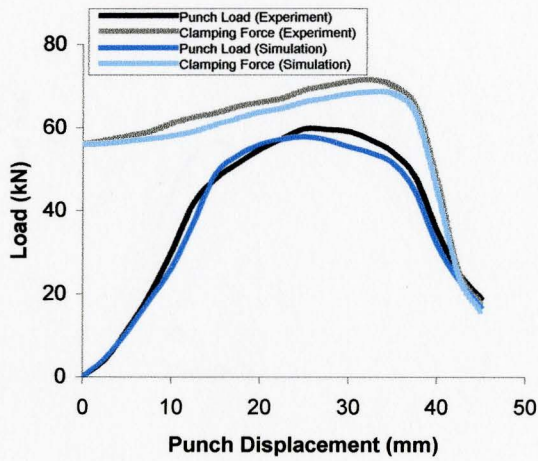
Initial centre hole size (mm)	Cup height (mm)		Flange diameter (mm)		Centre hole diameter (mm)	
	Experiment	Simulation	Experiment	Simulation	Experiment	Simulation
0	43.31	43.35	Full cup	Full cup	0	0
5	43.51	43.65	Full cup	Full cup	6.87	6.69
10	25.95	26.02	93.66	92.36	21.74 Crack	20.78 Crack
15	21.54	22.01	103.01	102.46	29.93 Crack	28.89 Crack
20	19.21	19.09	106.98	107.32	38.94 Crack	38.54 Crack
25	18.41	18.35	108.75	108.96	Punch thru	Punch thru
30	15.87	15.59	109.37	109.46	Punch thru	Punch thru
35	13.27	13.25	109.76	109.65	Punch thru	Punch thru



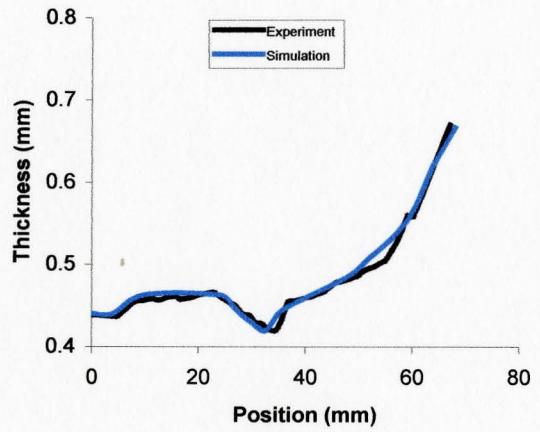
(a1)



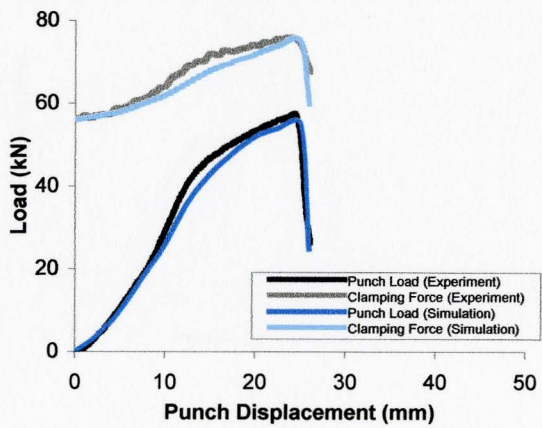
(a2)



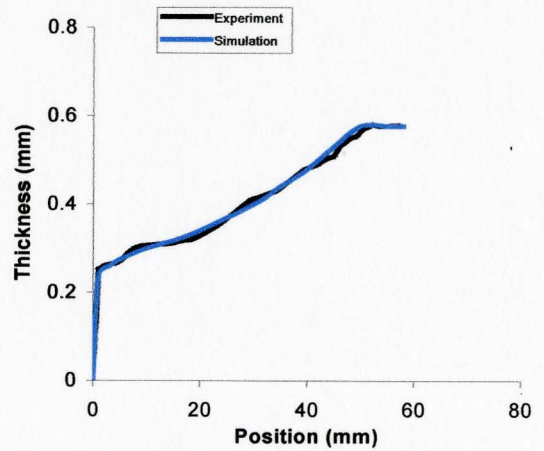
(b1)



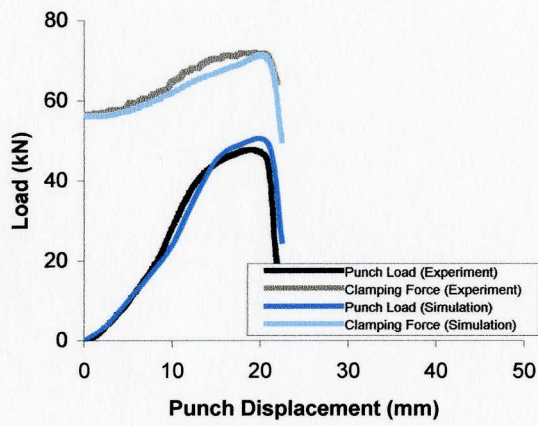
(b2)



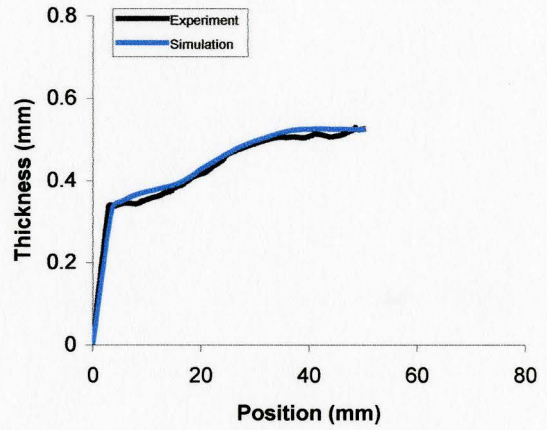
(c1)



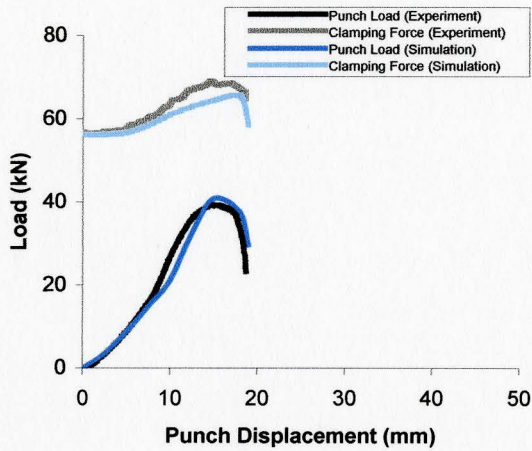
(c2)



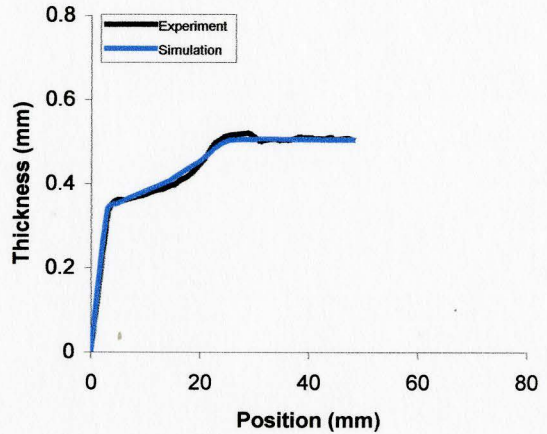
(d1)



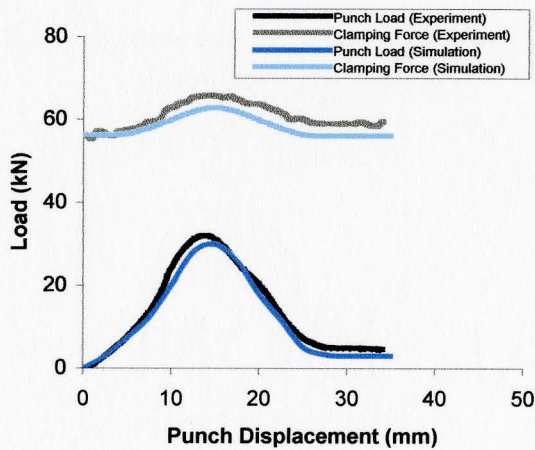
(d2)



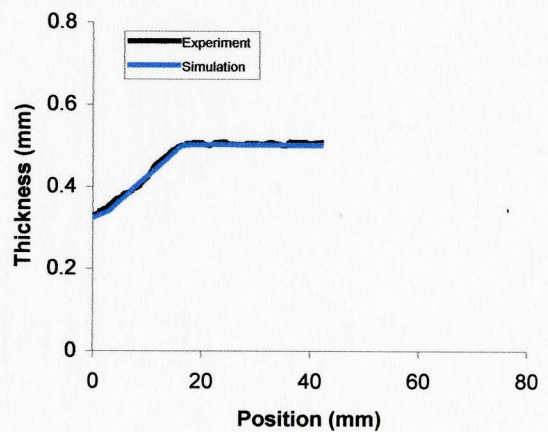
(e1)



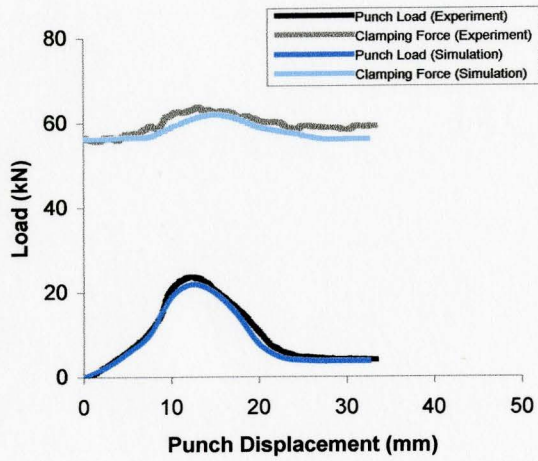
(e2)



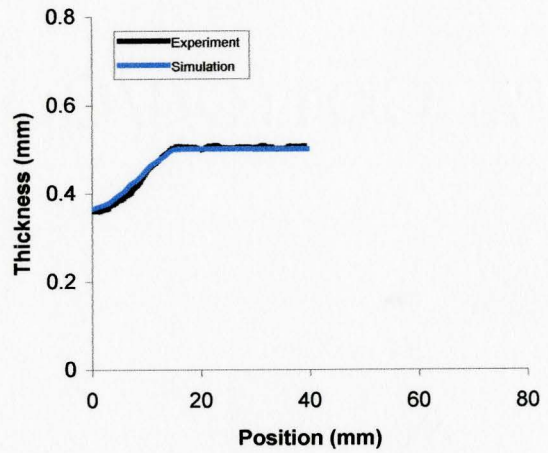
(f1)



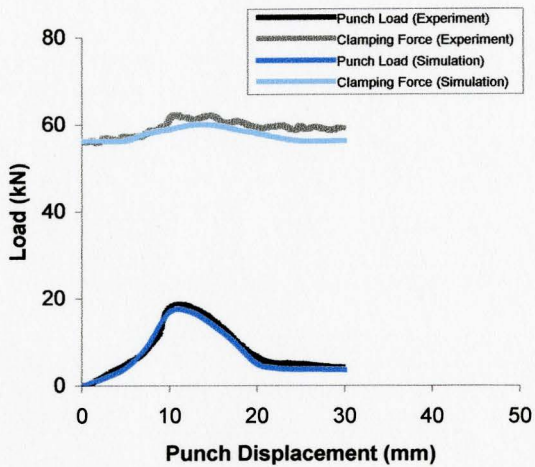
(f2)



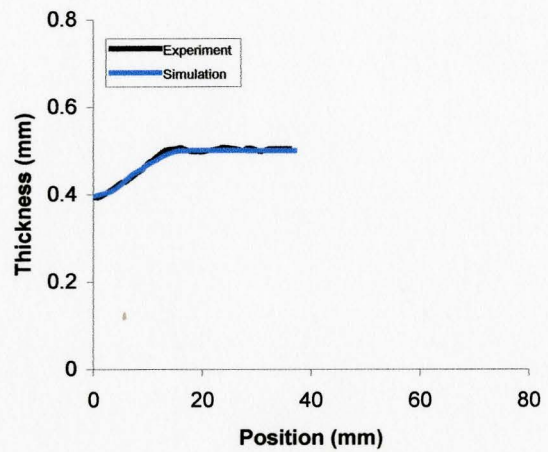
(g1)



(g2)



(h1)



(h2)

Figure AG.4 Experimental and simulation results comparison of deep drawing with centre hole blank process: (a1)-(h1) punch load and clamping force versus punch displacements and (a2)-(h2) thickness distributions along the cup profile from 0 mm – 35 mm initial centre hole diameter receptively

Appendix H: Logical Flow Chart of Simulation Set Up to Determine Limiting Drawing Ratio of Deep Drawing and Redrawing Operations and Critical Flanging Ratios for Deep Drawing with Centre Hole Blanks

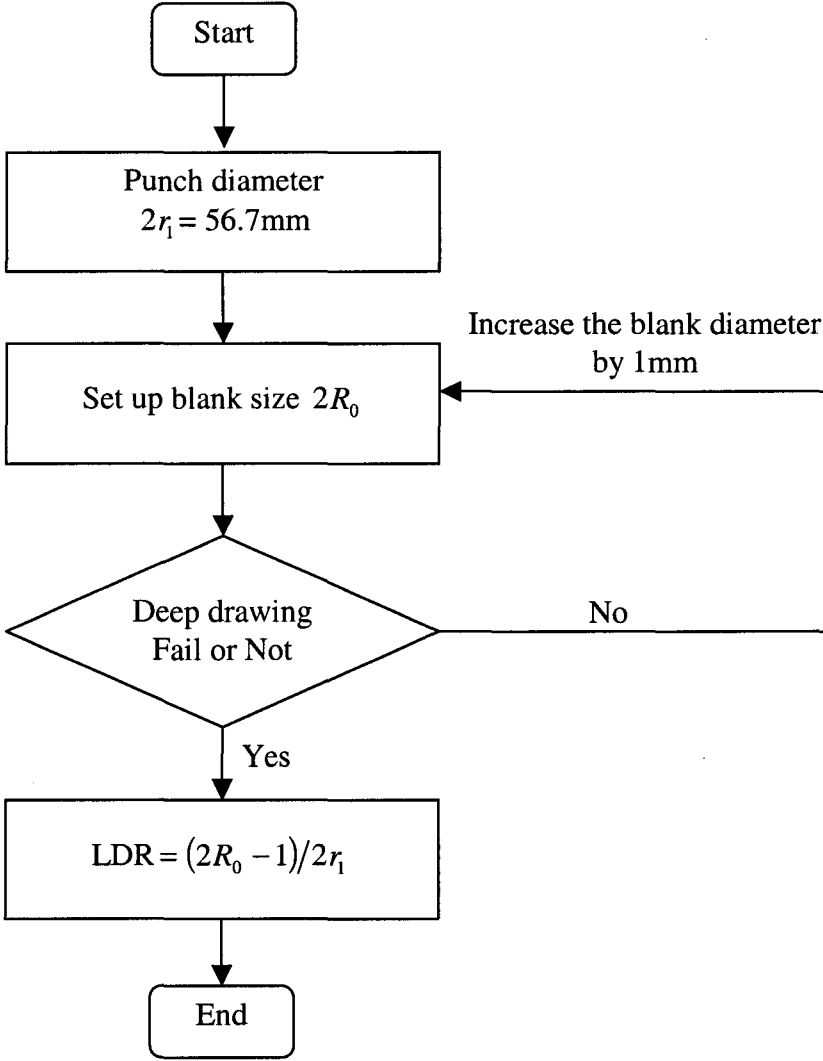


Figure AH.1 Logical flow chart of simulation work to determine limiting drawing ratio for deep drawing process

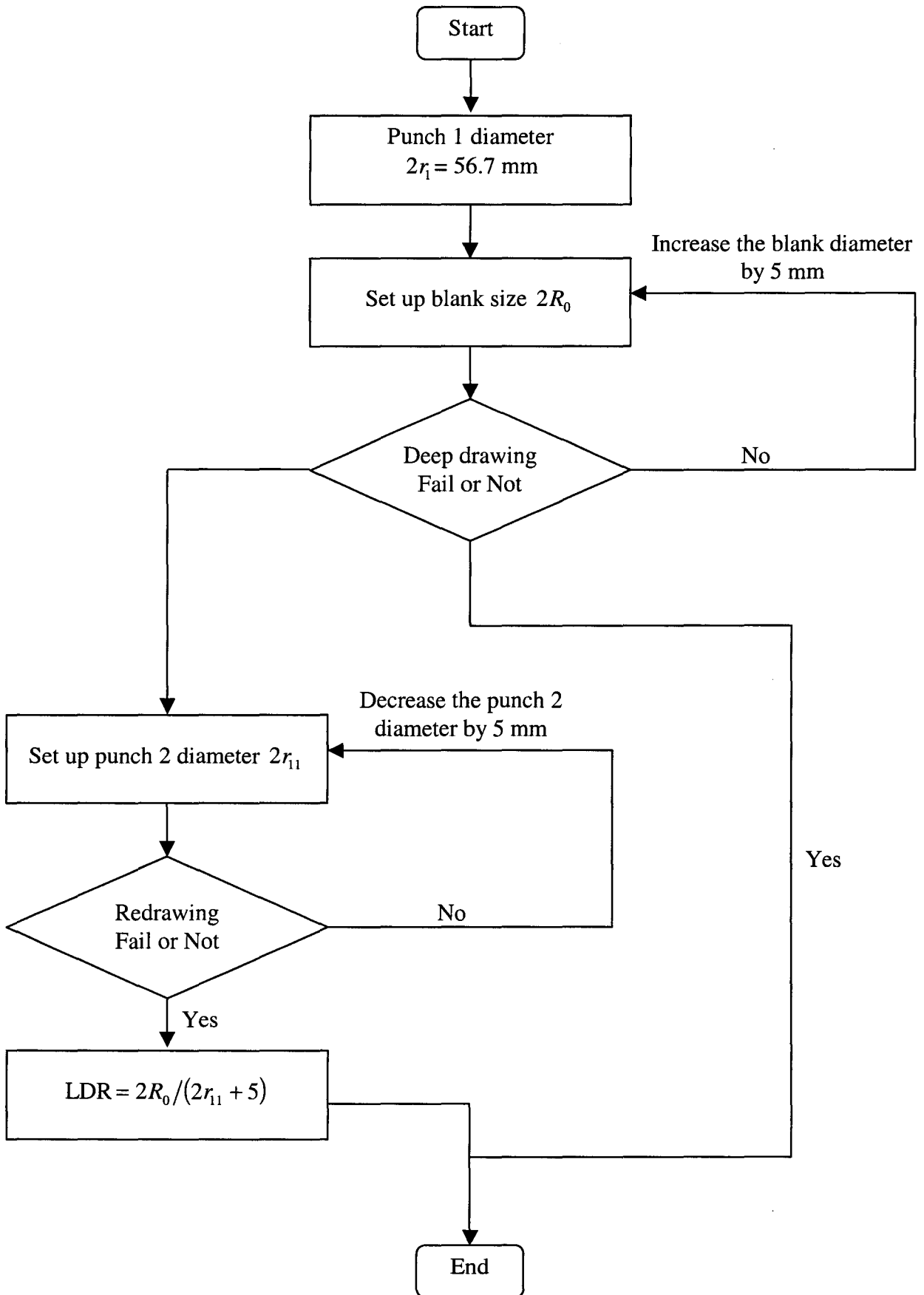


Figure AH.2 Logical flow chart of simulation work to determine limiting drawing ratio with one redrawing process

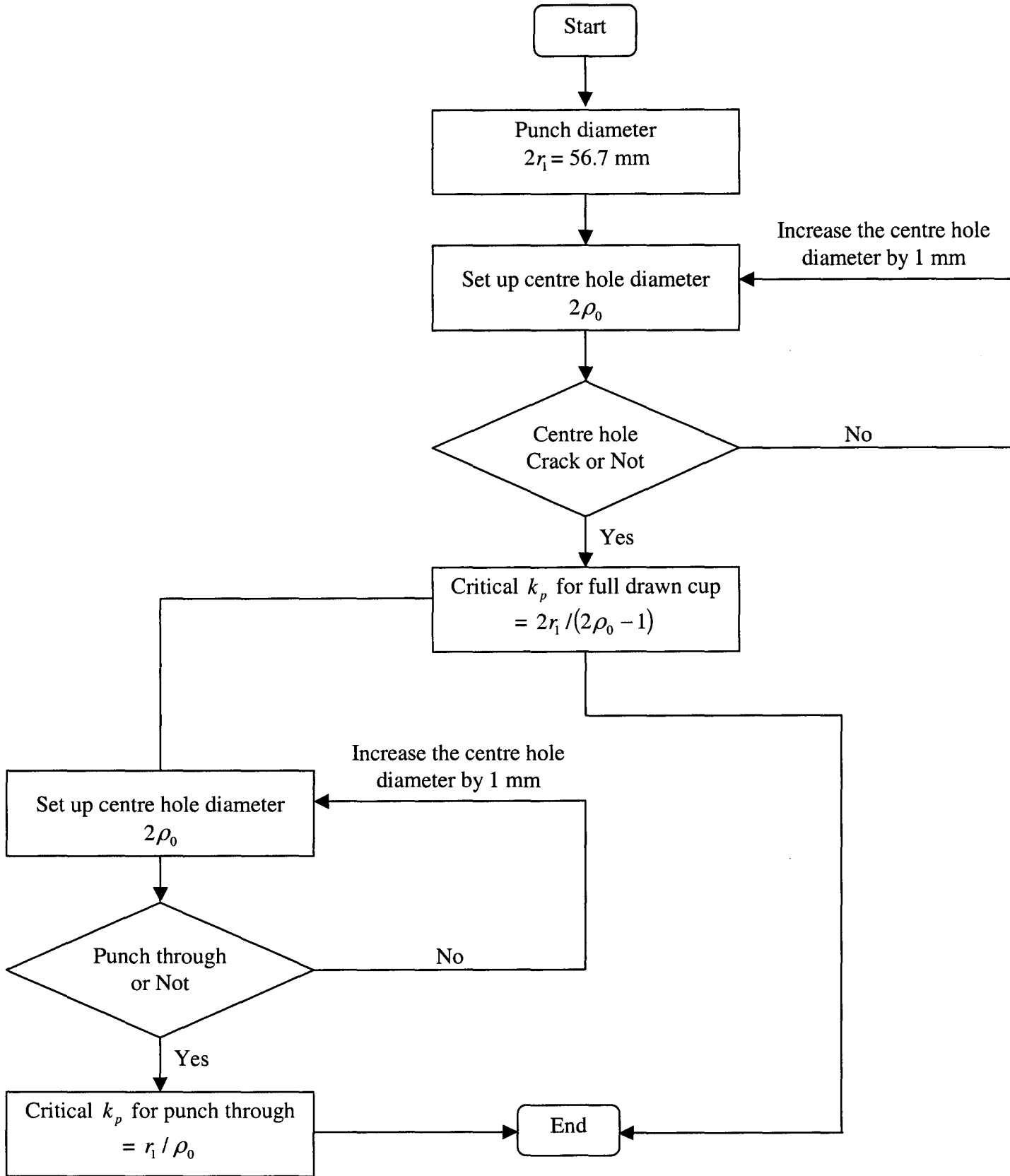


Figure AH.2 Logical flow chart of simulation work to determine critical flanging ratios of deep drawing with centre hole blanks

Appendix I: Simulation Results to Determine Limiting Drawing Ratio of Deep Drawing and Redrawing Processes

Table AI.1 Simulation progress to determine limiting drawing ratio of deep drawing at dry friction condition

Initial blank diameter (mm)	Fail or Not	Drawing ratio
100	No	1.764
105	No	1.852
110	No	1.940
112	No	1.975
114	No	2.011
116	No	2.049
117	No	2.063
118	No	2.081
119	No	2.099
120	No	2.116
121	Yes	/
Limiting drawing ratio		2.116

Table AI.2 Simulation progress to determine limiting drawing ratio of deep drawing at Teflon friction condition

Initial blank diameter (mm)	Fail or Not	Drawing ratio
120	No	2.116
125	No	2.205
130	No	2.293
135	No	2.381
136	No	2.399
137	No	2.416
138	No	2.434
139	Yes	/
Limiting drawing ratio		2.434

Table AI.3 Simulation progress to determine limiting drawing ratio with one redrawing at dry friction condition

Initial blank diameter (mm)	Deep drawing Fail or Not	Second punch diameter (mm)	Redrawing Fail or Not	Drawing ratio
85	No	35	No	2.429
		30	No	2.833
		25	Yes	/
90	No	35	No	2.571
		30	No	3.000
		25	Yes	/
95	No	40	No	2.375
		35	No	2.714
		30	Yes	/
100	No	40	No	2.500
		35	No	2.857
		30	Yes	/
105	No	45	No	2.333
		40	No	2.625
		35	Yes	/
110	No	45	No	2.444
		40	No	2.750
		35	Yes	/
115	No	50	No	2.300
		45	No	2.556
		40	Yes	/
120	No	50	No	2.400
		45	No	2.667
		40	Yes	/
125	Yes	/	/	/
Limiting drawing ratio				3.000

Table AI.4 Simulation progress to determine limiting drawing ratio with one redrawing at Teflon friction condition

Initial blank diameter (mm)	Deep drawing Fail or Not	Second punch diameter (mm)	Redrawing Fail or Not	Drawing ratio
85	No	30	No	2.833
		25	No	3.400
		20	Yes	/
90	No	30	No	3.000
		25	No	3.600
		20	Yes	/
95	No	35	No	2.714
		30	No	3.167
		25	Yes	/
100	No	35	No	2.857
		30	No	3.333
		25	Yes	/
105	No	40	No	2.625
		35	No	3.000
		30	Yes	/
115	No	40	No	2.875
		35	No	3.286
		30	Yes	/
125	No	50	No	2.500
		45	No	2.778
		40	Yes	/
135	No	50	No	2.700
		45	No	3.000
		40	Yes	/
140	Yes	/	/	/
Limiting drawing ratio				3.600

Table AI.5 Simulation progress to determine LDR from 5 mm initial center hole blank at dry friction condition

Initial blank diameter (mm)	Fail or Not	Drawing ratio
118	No	2.081
119	No	2.099
120	No	2.116
121	Yes (crack at the corner area)	/
Limiting drawing ratio		2.116

Table AI.6 Simulation progress to determine LDR from 6 mm initial center hole blank at dry friction condition

Initial blank diameter (mm)	Fail or Not	Drawing ratio
118	No	2.081
119	No	2.099
120	No	2.116
121	Yes (crack at the corner area)	/
Limiting drawing ratio		2.116

Table AI.7 Simulation progress to determine LDR from 7 mm initial center hole blank at dry friction condition

Initial blank diameter (mm)	Fail or Not	Drawing ratio
118	No	2.081
119	No	2.099
120	No	2.116
121	Yes (crack at the corner area)	/
Limiting drawing ratio		2.116

Table AI.8 Simulation progress to determine LDR from 8 mm initial center hole blank at dry friction condition

Initial blank diameter (mm)	Fail or Not	Drawing ratio
114	No	2.011
115	No	2.028
116	No	2.046
117	Yes (crack at center hole)	/
Limiting drawing ratio		2.046

Table A1.9 FE simulation results of deep drawing from blanks with different center hole diameters

Initial center hole diameter ρ_0 (mm)	Flanging ratio k_p	Results
5	11.340	Full drawn cup
6	9.450	Full drawn cup
7	8.100	Full drawn cup
8	7.088	Full drawn cup
9	6.300	Full drawn cup
10	5.670	Cracking at the center hole
15	3.780	Cracking at the center hole
20	2.840	Cracking at the center hole
21	2.700	Cracking at the center hole
22	2.577	Cracking at the center hole
23	2.465	Cracking at the center hole
24	2.363	Cracking at the center hole
25	2.268	Punch through
30	1.890	Punch through
35	1.620	Punch through